

2013-01-01

Comparative Characterization of Ni-Base Superalloys Fabricated by Laser and Electron Beam Melting Technologies

Krista Amato

University of Texas at El Paso, knamato@miners.utep.edu

Follow this and additional works at: https://digitalcommons.utep.edu/open_etd



Part of the [Materials Science and Engineering Commons](#), and the [Mechanics of Materials Commons](#)

Recommended Citation

Amato, Krista, "Comparative Characterization of Ni-Base Superalloys Fabricated by Laser and Electron Beam Melting Technologies" (2013). *Open Access Theses & Dissertations*. 1778.
https://digitalcommons.utep.edu/open_etd/1778

This is brought to you for free and open access by DigitalCommons@UTEP. It has been accepted for inclusion in Open Access Theses & Dissertations by an authorized administrator of DigitalCommons@UTEP. For more information, please contact lweber@utep.edu.

COMPARATIVE CHARACTERIZATION
OF NI-BASE SUPERALLOYS FABRICATED BY LASER AND ELECTRON
BEAM MELTING TECHNOLOGIES

KRISTA NAOMI AMATO

Materials Science and Engineering

APPROVED:

Lawrence E. Murr, Ph.D., Chair

Robert R. Chianelli, Ph.D.

Felicia S. Manciu, Ph.D.

Stephen W. Stafford, Ph.D.

Benjamin C. Flores, Ph.D.
Dean of the Graduate School

by
Krista Naomi Amato
2013

Dedication

Thank you to my parents for exposing me to engineering as a young girl and to them and my brothers for being supportive of all of my ambitions. Thank you, Jenny for being with me every step of the way for the last seven years. We did it! I am so grateful to my professors in the MME department for providing me the opportunity to excel in research and making my college experience so enjoyable. You have made such a huge impact in my life.

COMPARATIVE CHARACTERIZATION
OF NI-BASE SUPERALLOYS FABRICATED BY LASER AND ELECTRON BEAM
MELTING TECHNOLOGIES

by

KRISTA NAOMI AMATO, B.S.

DISSERTATION

Presented to the Faculty of the Graduate School of
The University of Texas at El Paso
in Partial Fulfillment
of the Requirements
for the Degree of

DOCTOR OF PHILOSOPHY

Materials Science and Engineering
THE UNIVERSITY OF TEXAS AT EL PASO
May 2013

Acknowledgements

I would like to thank Dr. Murr for convincing me to join the doctoral program instead of the master's program. I never saw myself going to that level until I spoke with him. Without my research group, my life would have been much more difficult, and I appreciate all your help, Jenny, Edwin, Frank and Patrick. I would also like to acknowledge Sara for all the advice for mentoring me through my graduate years. I can't forget David Brown because he is the reason the MME department runs so smoothly. Thank you.

Abstract

Nickel-base superalloys have been used in cast and wrought, and powder metallurgy forms for nearly four decades for industrial and automotive applications. One drawback of cast alloys is that upon solidification, there is minimal microstructural control. Another issue to be improved is to eliminate the limitations of shapes and forms of fabricated alloys.

Rapid prototyping is a new technology of additive manufacturing that shows to be promising for the freeform fabrication of novel superalloys, including nickel-base alloys. New rapid manufacturing technologies allow us to produce parts in any shape that can be designed by computer-aided design (CAD) software. Additionally, the microstructure can be controlled by adjusting build parameters during fabrication.

Components made from Inconel 718 pre-alloyed powder have been fabricated by selective laser melting in two different orientations. These components, built in the transverse and longitudinal directions, parallel and perpendicular to the build direction, respectively, have been compared. Inconel 625 and has been fabricated by electron beam and selective laser melting. The two processes have been compared to each other as well as to their respective cast and wrought alloys. Microstructural characterization has been conducted using optical metallography, X-ray diffraction, scanning electron microscopy, and transmission electron microscopy. Mechanical properties have been analyzed by Vickers microhardness, macrohardness, and tensile testing.

Table of Contents

Dedication.....	iii
Acknowledgements.....	v
Abstract.....	vi
Table of Contents.....	vii
List of Tables	ix
List of Figures.....	x
Chapter 1: Introduction.....	1
1.1 Properties and Applications of Inconel 718.....	1
1.2 Properties and Applications of Inconel 625.....	2
1.3 Background of Additive Manufacturing.....	3
Chapter 2: Research Objectives.....	5
Chapter 3: Build Direction and Environment Comparison of Inconel 718	6
3.1 Experimental Methods.....	7
3.2 Results and Discussion	10
3.3 Summary.....	34
Chapter 4: Inconel 625 Fabricated by Selective Laser and Electron Beam Melting.....	37
4.1 Fabrication Process Comparison: EBM vs. SLM.....	37
4.2 Experimental Methods.....	40
4.3 Results and Discussion	40
4.4 Summary.....	78
Chapter 5: Discussion	80
5.1 Fabrication parameters.....	80
5.2 X-Ray Diffraction	80
5.3 Scanning and Transmission Electron Microscopy	81
5.4 Mechanical Behavior	81

Chapter 6: Conclusion	83
References.....	84
Vita.....	85

List of Tables

Table 3.1 Mechanical properties for Inconel 718 cylindrical components fabricated by selective laser melting (SLM) in argon or nitrogen.	36
Table 4.1. Chemical Composition for Alloy 625 EBM and SLM Precursor Powders and Fabricated Components	39
Table 4.2. Mechanical Properties for EBM and SLM Processed Alloy 625	74
Table 4.3. Comparative Precipitation for EBM and SLM Processed Alloy 625	77

List of Figures

Figure 3.1. SEM views of the prealloyed (Inconel 718) precursor powder. (a) Lower magnification showing the range of powder sizes and spherical morphology. (b) OM image for powder particle etched cross-section showing interior microdendritic microstructure.	6
Figure 3.2. SLM system schematic: Electron gun (1), rotating mirror lens system (2), beam focus lens (3), powder roller (4), build platform (5), powder feed (6), powder recycle container (7).	7
Figure 3.3. SLM as-fabricated cylinders built in (a) z-axis and (b) x-y axis orientations.	8
Figure 3.4. (a) Melt pool overlap and layer development observed in the vertical reference plane (parallel to the build direction shown by the arrow) for an x-axis oriented, as-fabricated cylinder (in argon). (b) Magnified view showing columnar grain structure (G) and fine columnar special features (shown by arrow). B indicates the build direction.	11
Figure 3.5. 3D optical metallograph (OM image) composite showing the details of columnar grains and fine arrays relative to the build direction shown by arrow (top left) for an as-fabricated (x-axis) cylinder in argon gas.	12
Figure 3.6. XRD spectra for (a) precursor Inconel 718 powder, (b) EBM as-fabricated (z-axis) cylinder in argon for the horizontal reference plane, (c) vertical reference plane.	13
Figure 3.7. Schematic views illustrating the directional solidification-induced columnar grains and γ'' precipitate arrays as well as the melt-pool/layer structure development in SLM. The coincident plane variants for (100) [200] are shown at [002], [200] and [020].	14
Figure 3.8. OM 3D composite view for a cylindrical component (x-axis) fabricated in argon and HIPed in argon. Build direction is noted by the arrow (bottom right).	16
Figure 3.10. Vertical reference section (OM) views showing partial recrystallization for x-axis fabricated cylinder in nitrogen and HIPed in argon. Arrow in (a) shows the build direction. (b) shows a magnified view of (a).	18
Figure 3.11. OM 3D composite view for a cylindrical component (x-axis) fabricated in nitrogen and HIPed in argon. Build direction is noted by the arrow (bottom right).	19
Figure 3.12. TEM-3D image composite view for an as-fabricated (in argon) z-axis cylinder HIPed in argon. The SAED pattern insert corresponds to a γ [001] zone in the vertical reference plane as shown. The arrow to the right indicates the build direction.	21
Figure 3.13. XRD spectra representing as-fabricated and HIPed (in argon) z-axis oriented specimen. (a) Horizontal reference plane (normal to the build direction). (b) Vertical reference plane (parallel to the build direction).	22
Figure 3.14. Magnified TEM bright-field image for a vertical reference plane section corresponding to Fig. 3.12. Lenticular-like/oblate ellipsoidal γ'' precipitates are coherent with {100} planes in two	

prominent columns (c) which are parallel to the build direction noted by large arrow. Some precipitates are coincident with the $\{010\}$ variant shown. The SAED pattern insert shows a γ $[001]$ zone axis. γ''

$\langle \bar{1}00 \rangle$ and $\langle 1 \frac{1}{2} 0 \rangle$ reflections are noted by spots designated 1 and 2, respectively.....24

Figure 3.15. Horizontal reference plane (OM) view for recrystallized microstructures following as-fabricated (argon) and annealed treatment (argon) for an x-axis oriented cylinder.26

Figure 3.16. (a) Vertical reference plane (OM) view for recrystallized microstructures corresponding to Figure 3.15, showing melt pool interaction and layering in remnant columnar microstructure. Arrow denotes the build direction. (b) Horizontal plane reference (OM image) corresponding to (a) etched to reveal the recrystallized grain and annealing twin (γ) boundaries (arrow).....27

Figure 3.17. OM 3D composite view for the annealed (4h @1160°C) argon-fabricated, x-axis cylinder. The recrystallized regions are denoted R. Selective etching reveals homogeneous globular precipitates. C indicates the original (remnant) columnar microstructural architecture arrays. Arrow at upper left denotes the build direction.28

Figure 3.18. XRD spectra representing the as-fabricated and annealed (4h @1160°C) specimens corresponding to Fig. 3.17. (a) Horizontal reference plane. (b) Vertical reference plane.29

Figure 3.19. TEM observation of dense γ'' precipitation in recrystallized regions for annealed SLM-fabricated Inconel 718. The enlarged view shows oblate ellipsoidal γ'' precipitates coincident with (001)

(or (00 $\bar{1}$)) planes while the lower magnification dark-field image insert shows these precipitates imaged

with the $[00\bar{1}]$ (bct) reflection at small arrow in the SAED pattern insert. The surface orientation is noted as the $[210]$ fcc zone. A indicates a common reference for the enlarged view and the reduced magnification, dark-field image insert. Note the magnification bar in the dark-field insert is the same as shown in the bright-field image.31

Figure 3.20. δ precipitate at a grain boundary separating an unrecrystallized grain from a recrystallized grain. (a) shows recrystallized grain as (R). (b) magnified view of precipitate. (c) tilted view of (b).32

Figure 4.1 (a) EBM system schematic: Electron gun (1), Beam focus lens (2), Beam scan coils (3), Powder cassettes (4), Powder layer rake (5), Building component (6), build platform (7). (b), SLM powder microstructure and low magnification insert. (a) is adapted from Murr et al. (2012a)38

Figure 4.3. TEM vertical plane section view (parallel to the build direction (B) showing γ'' precipitate platelets coincident with the NiCr fcc matrix $\{111\}$ planes. The grain surface orientation is (110). The build direction marked B is coincident with the arrow in Fig. 4.2.42

Figure 4.4. XRD spectra corresponding to the horizontal and vertical reference planes in Figure 4.2 (EBM).43

Figure 4.5. 3D LOM composite section for an SLM (Z-axis) fabricated component. Note build direction represented by the arrow is parallel to the Z-axis orientation.45

Figure 4.6. XRD spectrum corresponding to the vertical and horizontal reference planes represented in Figure 4.5.....	46
Figure 4.7 3D LOM composite section for an SLM (X, Y-axis) fabricated component. Note build direction represented by the arrow at lower right which is perpendicular to the X, Y-axis, of the cylindrical component.	47
Figure 4.8. XRD spectrum corresponding to the vertical and horizontal reference planes represented in Figure 4.7.....	48
Figure 4.9. TEM bright-field images in the (a) horizontal (H) and (b) vertical (V) reference planes for Figure 4.7. P in (b) designates a precipitate (γ'') cluster. The build direction is denoted by white arrow (B) at right in (b) SAED pattern inserts show (112) orientation in the horizontal (H) plane (a), and (110) orientation in the vertical (V) plane (b). Note arrows in (a) show precipitate clusters within dislocation cell-like arrays.	50
Figure 4.10. TEM magnified view in Figure 4.9, P designates precipitate cluster in Figure 4.9. Column of precipitate clusters and dense dislocations is shown at right.	51
Figure 4.11. TEM image showing γ'' precipitation arrays. Reference section of array is enclosed in the dotted box. The SAED pattern insert shows the (110) grain surface orientation. The operating reflection for diffraction contrast is shown to be $g = [00\bar{2}]$	52
Figure 4.12. Magnified TEM image for Fig. 4.11 showing precipitate clusters within the dotted reference box. Arrows in (a) show precipitate clusters (aggregates) which exhibit Nb-rich features shown in the corresponding Nb-X-ray map in (b). (c) shows the TEM-EDS spectrum for (a).	53
Figure 4.13. SLM-laser melt-scan banding. (a) LOM image in vertical reference plane for X,Y-axis cylindrical component (b) SEM image showing γ'' precipitate/second-phase formation within the melt bands. (c) Magnified SEM image showing melt-band precipitates.....	55
Figure 4.14. EBM fabricated and HIP (Z-axis) component 3D LOM composition showing equiaxed, fcc (NiCr) grain structure and associated precipitation.	56
Figure 4.15. XRD spectra corresponding to the horizontal and vertical reference planes in Fig. 4.14. Prominent precipitation peaks are dark shaded.	57
Figure 4.16. TEM bright-field image showing typical intragranular precipitates (NbCr_2) corresponding to Fig. 4.15. Coherent annealing twin is shown in the image center (upper left to lower right).	58
Figure 4.17. Analytical sequence showing Cr precipitate in EBM fabricated and HIP component. (a) TEM image of precipitate at foil edge. (b) SAED pattern showing (110) orientation for supporting NiCr matrix. (c) EDS spectra for precipitate in (a). (d) Cr map using (c). (e) Ni map for (a). (f) EDS spectrum for NiCr matrix.....	59
Figure 4.18. SLM fabricated and HIP (Z-axis) component 3D LOM composition showing equiaxed, fcc (NiCr) grain structure and associated precipitation.	61

Figure 4.19. SLM fabricated and HIP (X, Y-axis) component 3D LOM composition showing equiaxed, fcc (NiCr) grain structure and associated precipitation.	62
Figure 4.20. XRD spectra corresponding to horizontal and vertical reference planes in Fig. 4.18. Precipitation peaks are dark shaded.....	63
Figure 4.21. XRD spectra corresponding to horizontal and vertical reference planes in Fig. 4.19. Precipitation peaks are dark shaded.....	64
Figure 4.22. SLM (Z-axis) fabricated and HIP component observed in vertical reference plane (Fig. 4.18). (a) SEM image of precipitates. (b) to (d) show corresponding EDS elemental X-ray maps. (c) Precipitate image.	65
Figure 4.23. SEM analysis sequence corresponding to Fig. 4.22(a). (a) Precipitates. (b) EDS spectra for (a). (c) to (f) show corresponding EDS elemental X-ray maps.	66
Figure 4.24. SEM analysis sequence corresponding to the vertical reference plane in Figure 4.19 (X, Y-axis) build. (a) Vertical surface view of precipitates. (b) Magnified view of precipitates. (c) to (e) show corresponding EDS elemental X-ray maps.....	68
Figure 4.25. EDS spectra corresponding to Fig. 4.24. (a) matrix. (b) Precipitate area as in Fig. 4.24(b).	69
Figure 4.26. TEM image in horizontal reference plane corresponding to Fig. 4.19 (X, Y-axis component). The grain surface orientation is (110) shown in SAED pattern insert. Operating reflection, $g = [\bar{1}11]$. Note diffraction spots normal to inclined twin plane in SAED pattern insert.	70
Figure 4.27. TEM image features for precipitates in a vertical reference plane corresponding to Fig. 4.19. The inserts (top right and bottom left) show magnified views for precipitates marked P_1 , P_2 , P_3 . Precipitates are single crystals dispersed noncoherently in the fcc NiCr matrix.....	71
Figure 4.28. TEM microanalysis sequence for precipitates in Fig. 4.27. (a) EDS analysis for precipitate P_1 . Insert shows Nb characteristic X-ray map. (b) EDS analysis for precipitate P_2 . (c) Ni and Nb characteristic X-ray maps for precipitate P_2 in Fig. 4.27.....	72
Figure 4.29. TEM microanalysis sequence for precipitate P_1 in Fig. 4.27. (a) Bright-field image. (b) SAED pattern for (a). (c) Dark-field image of (a) using $[2\bar{4}6]$ diffraction spot circled in (b). (d) Tilted bright-field image of (a).....	73
Figure 4.30. Failed tensile specimen for EBM fabricated and HIP component (a) and SEM image of corresponding fracture surface (b).	75
Figure 4.31. TEM image for failed tensile specimen in Fig. 4.30(a) in a section ~ 2 mm from the fracture surface, perpendicular to the tensile axis. The two views show sections in a (123) oriented matrix grain. $NbCr_2$ precipitates are observed.....	76

Chapter 1: Introduction

Nickel-base alloys are increasingly being used in many industries today. Nickel is highly soluble with elements in a wide solubility range including iron and chromium, which allows for solid solution strengthening, carbide precipitation, and precipitation hardening of nickel-base alloys. Its ability to alloy with most metals combined with advancements in powder metallurgy processing and new melting technologies gives numerous possibilities to develop parts for high-strength, high-temperature, and even cryogenic applications.

Cast and wrought alloys have limitations, which decrease or prevent microstructural control. Additive manufacturing provides a way to manipulate properties as well as shape so that the alloy may be used for any desired application. One advantage of the advanced technology of additive manufacturing is that it is controlled by computer software that allows the fabrication of any 3-D model that can be input into computer-aided design (CAD) software. It would be ideal to compare two methods of rapid manufacturing as well as the parameters involved in the fabrication process using Inconel 625 and Inconel 718 to study the microstructures and to compare the properties of alloys fabricated by layer manufacturing to cast and wrought alloys. To understand the change in properties, materials characterization must be performed. Furthermore, it would be pertinent to heat-treat these fabricated components and compare the properties of heat-treated specimens to the as-fabricated and cast alloy to understand how to improve the properties to their maximum potential.

1.1 Properties and Applications of Inconel 718

Unlike many alloys in its family, Inconel 718 is a precipitation-hardenable Ni-Cr alloy. Its composition (51Ni-22Fe-19Cr-5Nb-3Mo-1Co, with lesser additions of Ti (~1%) and Al (~0.5%)) allows Inconel 718 to have high corrosion resistance simultaneously with high strength and flexibility as well as being highly resistant to post-welding cracking. Inconel alloys also have good fatigue strength and

good cryogenic properties. Significant amounts of Ni and Cr are responsible for high-temperature corrosion, oxidation, and carburization resistance. Other important elements such as Fe, Nb, and Mo, with smaller amounts of Al and Ti, increase the mechanical and corrosion resistance of this alloy. The face-centered cubic γ (NiCr) matrix in Inconel 718 is a solid solution partially responsible for high strength, but the main strengthening mechanism of Inconel 718 is the precipitation in the form of cubic (ordered face-centered) γ' ($\text{Ni}_3(\text{Al,Ti,Nb})$), body-centered tetragonal (DO_{22}) γ'' (Ni_3Nb), and orthorhombic (DO_a) δ (Ni_3Nb) phases distributed within the matrix and along grain boundaries. However, other phases detrimental to the applications of Inconel 718 in its wrought form are present and must be heat-treated to achieve the desirable precipitation phases to develop a higher-performing alloy. These properties are desirable for common applications such as tooling, but Inconel 718 has been more commonly used for applications in a wide range of temperatures from cryogenic tanks to most aircraft engine components and structural applications up to $\sim 700^\circ\text{C}$ including gas turbine blades, combustors, and rocket motors. (Mankins, et al. 1990; Smith 1981)

1.2 Properties and Applications of Inconel 625

Inconel 625 is a Ni-Cr-Mo alloy with an addition of niobium that has its solid-solution hardening of the NiCr face-centered cubic (γ) matrix. At elevated temperatures, molybdenum acts with the small addition of niobium, and other alloying elements such as iron, cobalt, titanium and aluminum, and stiffens the matrix. The difference in atomic diameter between nickel and its alloying elements ranges from 1 to 13%, in which the lattice expansion is a large factor for hardening at elevated temperatures. Molybdenum, however, is the most effective hardener of alloy 625 above $0.6T_m$ due to its slow diffusion rate in the high-temperature creep range. Aside from high strength, chromium provides excellent corrosion resistance and oxidation resistance near nickel's melting temperature (1450°C). Precipitation of intermetallic phases and carbides occur when the alloy is subjected to elevated temperatures ranging from $550\text{--}750^\circ\text{C}$. Inconel 625's wide service temperature range (from cryogenic to $\sim 980^\circ\text{C}$) allows

many industries, including aeronautical, aerospace, chemical, petrochemical, marine, and nuclear, to use this superalloy for many applications. (Ganesh, et al. 2010; Mankins, Lamb 1990; Shankar 2001)

1.3 Background of Additive Manufacturing

Over the past decade a variety of additive-layer manufacturing technologies employing electron and laser beam fabrication have demonstrated novel prospects for developing complex and multifunctional components with applications in biomedical, aeronautical, and automotive areas (Cormier et al., 2004; Murr et al., 2009; Murr et al., 2012a). In contrast to more conventional metal or alloy fabrication involving cast or wrought processing, electron and laser beam processing, especially electron beam melting (EBM) and selective laser melting (SLM) involve new directional solidification concepts as well as novel prospects for microstructure control through the development of scanning strategies or related process variables (Thijs et al., 2010; Bontha et al., 2009). These features produce solidification cooling rate and thermal gradient phenomena, which contribute to microstructure and microstructural architecture development and resulting mechanical properties.

Thijs et al. (2010) have shown that laser beam scan speed and beam power can control grain orientation and martensitic transformation in Ti-6Al-4V alloy. Similar phenomena have been demonstrated in the development of solidification maps to investigate trends in grain size and morphology in Ti-6Al-4V by Bontha et al. (2009). Murr et al. (2009) have compared Ti-6Al-4V microstructures for EBM and SLM fabrication where the more rapid SLM solidification cooling produced a propensity of α' -martensite. More recent observations of EBM and SLM fabrication of Ni-base and Co-base superalloys have demonstrated the development of columnar precipitates formed within the micron-size melt pools along with textured, columnar grains in the fcc matrix (Gaytan et al., 2010; Murr et al; 2011). Similar texturing of martensite laths has also recently been observed in the SLM fabrication of 17-4 PH stainless steel as well (Murr et al., 2012b). In these studies, EBM fabrication involved connected melt pools measuring 2-3 μm while SLM fabrication involved melt pool dimensions $\sim 1 \mu\text{m}$. EBM scanning differs from SLM scanning in fundamental ways which include the energy absorption and deposition within the additively-formed powder bed layers, beam focus and scan spacing, as well as powder bed pre-heat scanning and multiple or re-melt scanning. These thermo-

kinetic phenomena can influence precipitate or other phase development and transformation in complex ways, which differ notably from more conventional thermo-processing. (Amato, et al., 2012)

These recent technological innovations using laser and electron beams controlled by computer-aided software to build 3-D solid models from pre-alloyed metal powders allow for mass customization and the fabrication of complex parts used for long-term functionality. A big advantage of rapid manufacturing includes the elimination of tooling, which reduces production time and cost.

The research in this presentation has been published in the following papers:

1. Amato, K.N., Gaytan, S.M., Murr, L.E., Martinez, E., Shindo, P.W., Hernandez, J., Collins, S., and Medina, F. *Acta Materialia* 2011; 60(1): 2229-39.
2. Amato, K.N., Murr, L.E., Hernandez, J., Martinez, E., Gaytan, S.M., Shindo, P.W., and Collins, S. *Journal of Materials Science Research* 2012; 1(2).

Chapter 2: Research Objectives

The idea of this project is to determine a way to improve the properties of Inconel 718 and 625 while customizing their form to increase its range of applications via fabrication by selective laser and electron beam melting. Pre-alloyed precursor Inconel 718 and 625 powders were analyzed by optical metallography, scanning electron microscopy, and X-ray diffraction. The Inconel 718 powder was used to fabricate cylinders by selective laser melting using two different build methods; the cylinders were built in the z-axis orientation and the x-axis orientation, parallel to the build direction and perpendicular to the build direction, respectively. Cylinders were fabricated in either an Ar or N₂ environment and compared. The Inconel 625 powder was used to fabricate cylinders via two different processes: selective laser melting and electron beam melting. Sections of all cylinders were analyzed in both horizontal and vertical reference planes by optical microscopy, X-ray diffraction, scanning electron microscopy and transmission electron microscopy. Mechanical properties of powder and fabricated specimens were determined by macrohardness and microhardness measurements as well as tensile testing. As-fabricated specimens were HIP following a pre-anneal. Separate as-fabricated Inconel 718 cylinders were annealed. Similar analysis to as-fabricated specimens was performed on fabricated and HIP specimens and fabricated and annealed cylinders. Microstructural characteristics and mechanical properties of fabricated and fabricated and heat-treated specimens were compared to those of cast and wrought Inconel 718.

Chapter 3: Build Direction and Environment Comparison of Inconel 718

The contents of this chapter can be found in the following journal article:

Amato, K.N., Gaytan, S.M., Murr, L.E., Martinez, E., Shindo, P.W., Hernandez, J., Collins, S., and Medina, F. *Acta Materialia* 2011; 60(1): 2229-39.

In the present study, pre-alloyed, rapidly solidified (atomized) Inconel 718 powder served as a precursor for the production of additive manufactured components using selective laser melting (SLM). The SLM process utilizes an inert atmosphere (argon or nitrogen gas). This study represents a comprehensive microstructural and mechanical behavior characterization using optical metallography (OM), scanning and transmission electron microscopy (SEM and TEM employing energy-dispersive (X-ray) spectrometry (EDS)), and X-ray diffraction (XRD) analysis. Mechanical properties (hardness and tensile, including fracture surface analysis in the SEM) were also measured for as-fabricated and heat-treated components.

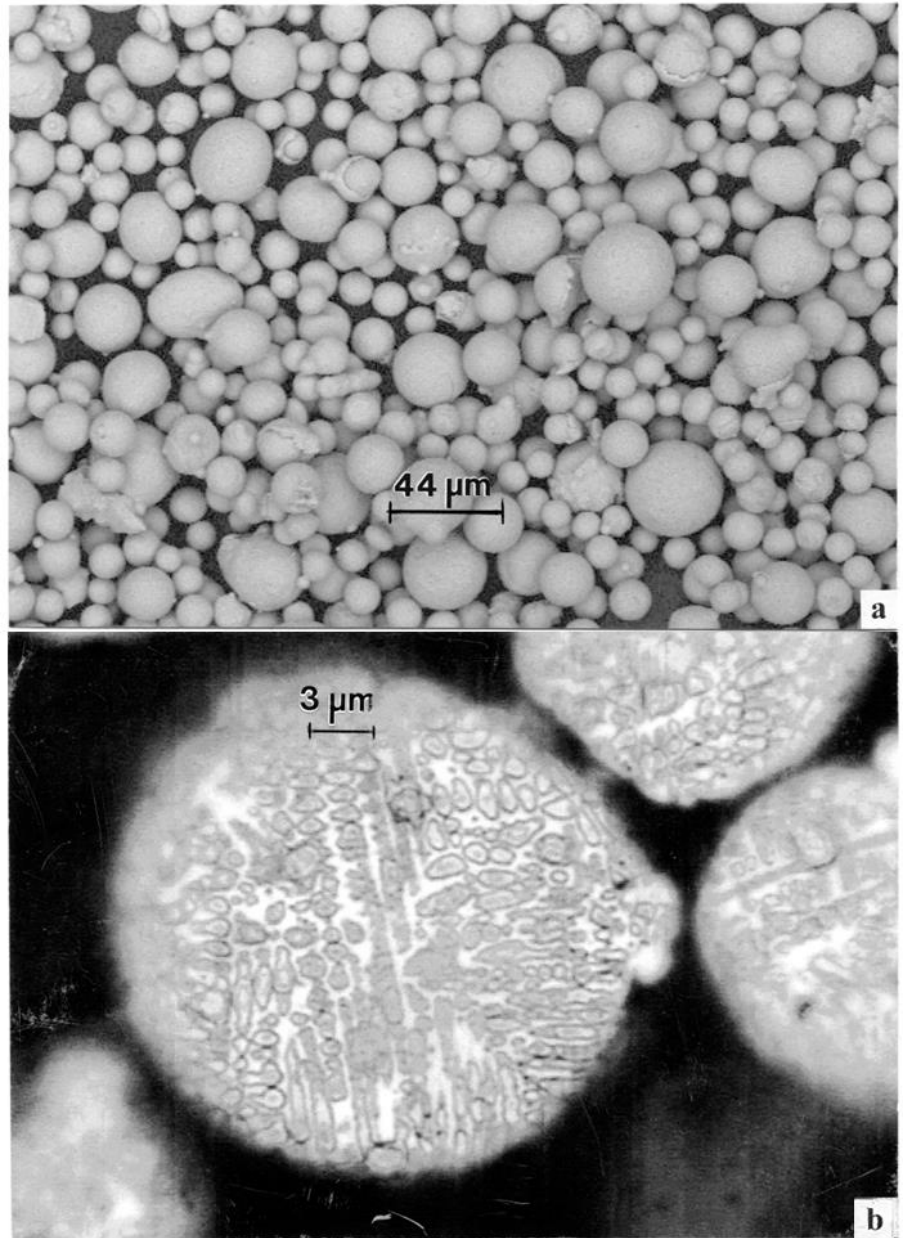


Figure 3.1. SEM views of the prealloyed (Inconel 718) precursor powder. (a) Lower magnification showing the range of powder sizes and spherical morphology. (b) OM image for powder particle etched cross-section showing interior microdendritic microstructure.

3.1 Experimental Methods

3.1.1 Precursor Powder and As-Fabricated Components

A pre-alloyed atomized Inconel 718 powder with a composition of 53.5Ni-19Cr-18.3Fe-5Nb-3Mo-1Ti-0.43Al was analyzed before being used to fabricate cylindrical components by selective laser melting. The powder size distribution and morphology was determined by the SEM image shown in Figure 3.1(a). The average particle size determined from this image is 17 μm . An OM image of a mounted, polished, and etched particle section shown in Figure 3.1(b) reveals the microdendritic structure of the powder.

3.1.2 Selective Laser Melting

Fabrication by selective laser melting was performed by an EOS M270 SLM system from EOS

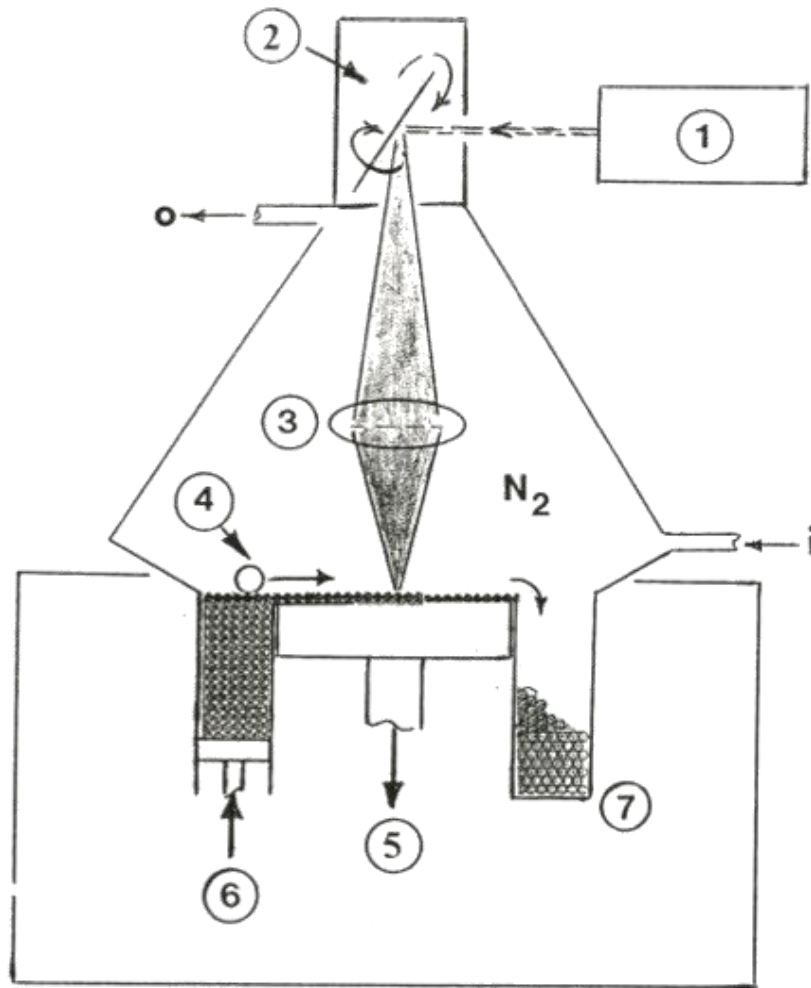


Figure 3.2. SLM system schematic: Electron gun ($\bar{1}$), rotating mirror lens system (2), beam focus lens (3), powder roller (4), build platform (5), powder feed (6), powder recycle container (7).

GmbH (Germany). The schematic in Figure 3.2 shows how the 0.2 kW Yb: YAG fiber laser beam (1), 100 μm in diameter, is scanned by a rotating lens mirror system (2) and then driven by an embedded CAD program (3) onto a powder bed. The mechanical recoater (4) rolls a layer of powder onto the build table (5) as powder is fed from a supply container (6). The excess powder is recycled after it is rolled into another container (7). The build table is heated to and maintained at 80°C throughout the build process. The beam scan

rate is 800 to 1200 mm/s during melting and scans in the x-y direction or alternating x and y directions for each layer. Efficient heat conduction and component cooling during SLM fabrication are achieved in a purified argon or nitrogen environment, which also provides oxidation resistance by purging oxygen from the system. The microstructure of the component can be altered by adjusting the beam scan speed, beam width, scan spacing, and scan strategies (directional or orthogonal x-y scans). Additionally, the layer may be remelted if rescanned by the melt scan, and a process anneal may occur if the beam is adjusted to re-heat the layer.

Cylindrical components with a diameter of 1.6 cm and a height of 8.75 cm were fabricated both perpendicular and parallel to the build direction, in the x-y axis and z-axis, respectively. Figure 3.3 shows fabricated cylinders in both transverse and longitudinal build directions. These cylinders were

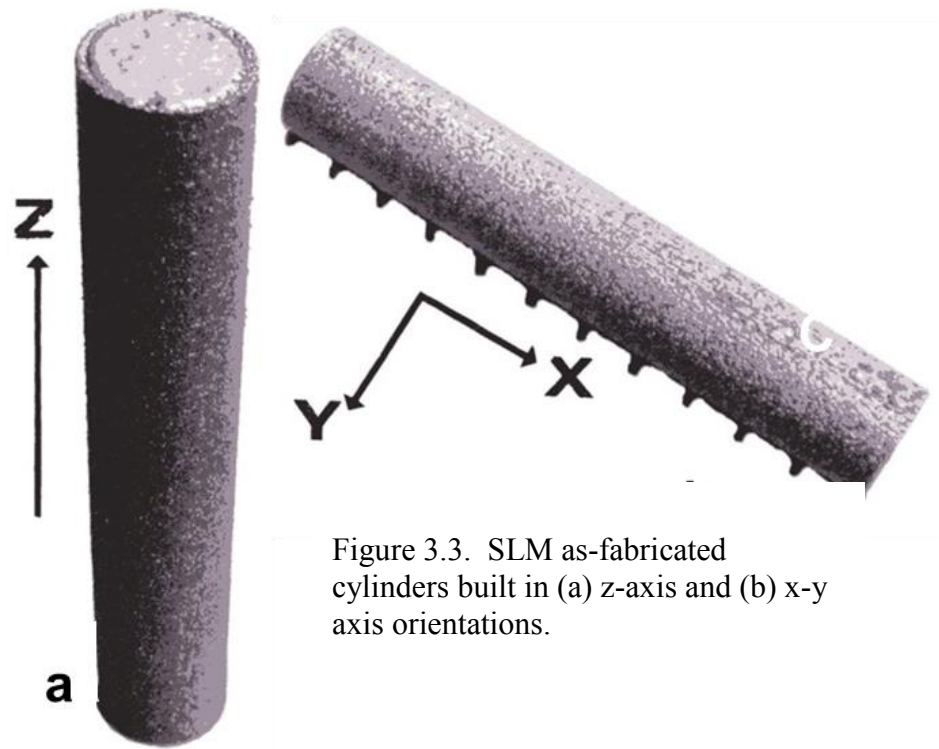


Figure 3.3. SLM as-fabricated cylinders built in (a) z-axis and (b) x-y axis orientations.

fabricated with alternating (x-y) scans in either argon or nitrogen gas environments surrounding the build components.

3.1.3 Heat Treatments

The as-fabricated cylinders were annealed at 982 °C under vacuum for 0.5 h, hot isostatic pressed (HIP) at 1163°C at 0.1 GPa for 4 h in argon. As-fabricated samples were also annealed in argon at 1160°C for 4 h. The microstructures of the HIP/annealed and annealed samples were compared to as-fabricated cylinders.

3.1.4 Microstructural Characterization

Optical Metallography

The microstructures for both the as-fabricated and HIP-annealed samples were observed by OM initially utilizing a Reichert MEF-4 A/M metallograph using digital imaging. Coupons were cut as horizontal (transverse) reference plane samples perpendicular to the beam direction (or build direction) or as vertical (longitudinal) reference plane samples parallel to the build direction. These coupons were mounted, ground, polished, and electro-etched in a solution of 70 mL phosphoric acid and 30 mL water, at room temperature; using 5V for etching times between 5s and 120s.

X-Ray Diffraction

XRD spectra were analyzed for the powder in Figure 3.1 as well as extracted coupons from transverse (horizontal) and longitudinal (vertical) reference planes from fabricated cylinders. The XRD system was a Bruker AXS-D8 Discover machine using a Cu target.

Scanning and Transmission Electron Microscopy

SEM imaging (as in Figure. 3.1(a)) employed a Hitachi S-4800 field emission (FE) SEM fitted with an EDAX-EDS system, and normally operated at 20 kV in the secondary electron or backscatter electron emission imaging modes. An EDAX energy-dispersive X-ray spectrometer (EDS) was also an attachment to the SEM for chemical analysis and elemental mapping. Extracted coupons were also examined in the TEM using a Hitachi H-9500, high-resolution, digital imaging system, operated at 300 kV. Specimens for TEM were prepared by grinding extracted coupons to a thickness of $\sim 200\ \mu\text{m}$, punching 3 mm discs, mechanically dimpling the discs, and electropolishing them in a Tenupol-5 dual jet system at a temperature of $\sim -30^\circ\text{C}$, using an etchant consisting of 200 mL perchloric acid and 800 mL methanol; at 13 V. The TEM was also fitted with a goniometer-tilt stage, which facilitated contrast control, selected-area electron diffraction pattern manipulation, and dark-field imaging. The TEM was also fitted with an EDAX energy-dispersive X-ray spectrometer (EDS) with a spatial resolution of chemical elements of roughly 20 nm on a side.

3.1.4 Mechanical Behavior

Microindentation (Vickers-HV) hardness and macroindentation hardness (Rockwell C-scale-HRC) using 0.25N and 1.5N loads, respectively, were made on specimen sections extracted from z-axis and x-axis cylinders parallel or perpendicular to the build direction and representing the horizontal and vertical reference planes correspondingly perpendicular to or parallel to the build direction. The microindentation hardness tester was a Shimadzu HVM-2000 digital measuring system. Measurements were averaged for 20 HV values and 10 HRC values measured.

Tensile specimens were machined from the as-fabricated Ar and N₂ gas built cylinders and the HIP-annealed cylinders representing both the vertical (z-axis) built specimens as well as the horizontal (x-axis) built specimens. Tensile testing was performed on a Universal Testing machine at room temperature ($\sim 22^{\circ}\text{C}$) at a strain rate of $\sim 10^{-3}\text{s}^{-1}$. Fracture surface examination was also performed using the SEM.

3.2 Results and Discussion

3.2.1 Microstructural Characterization

As-Fabricated Components

Figure 3.4(a) shows the appearance of melt pools and layer development as a result of alternating (x-y) melt scans every other layer when viewed in the vertical reference plane (in the build direction) for an x-axis oriented cylinder. This melt pool layer appearance has been observed for the SLM fabrication of Ti-6Al-4V components using a similar scanning strategy by Thijs et al. (2010). The melt pool width is observed to vary from $\sim 75\text{ }\mu\text{m}$ to $100\text{ }\mu\text{m}$ while the average layer thickness is observed to be $\sim 50\text{ }\mu\text{m}$. The magnified view in Figure 3.4(b) also shows the development of columnar grains and other regular columnar microstructures essentially parallel to the build direction (indicated by the arrow). When viewed in a 3-dimensional section as shown in Figure 3.5, the irregular, columnar microstructures shown in Figure 3.4(b) in the vertical reference plane are observed to compose an equiaxed or regular, spatial, columnar architecture having dimensions between 0.5 and $1\text{ }\mu\text{m}$ as observed in the horizontal reference plane section showing these arrays.

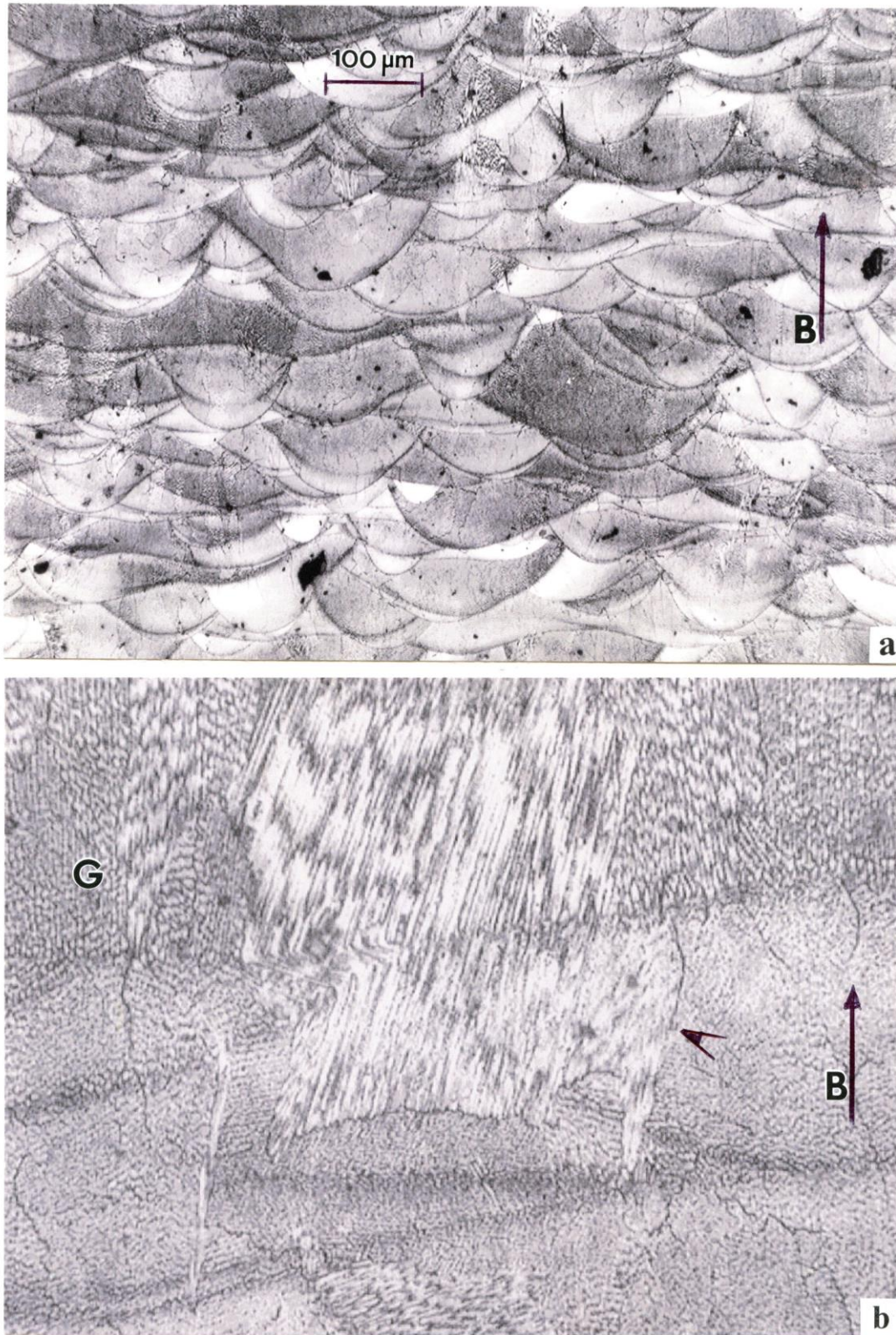


Figure 3.4. (a) Melt pool overlap and layer development observed in the vertical reference plane (parallel to the build direction shown by the arrow) for an x-axis oriented, as-fabricated cylinder (in argon). (b) Magnified view showing columnar grain structure (G) and fine columnar special features (shown by arrow). B indicates the build direction.

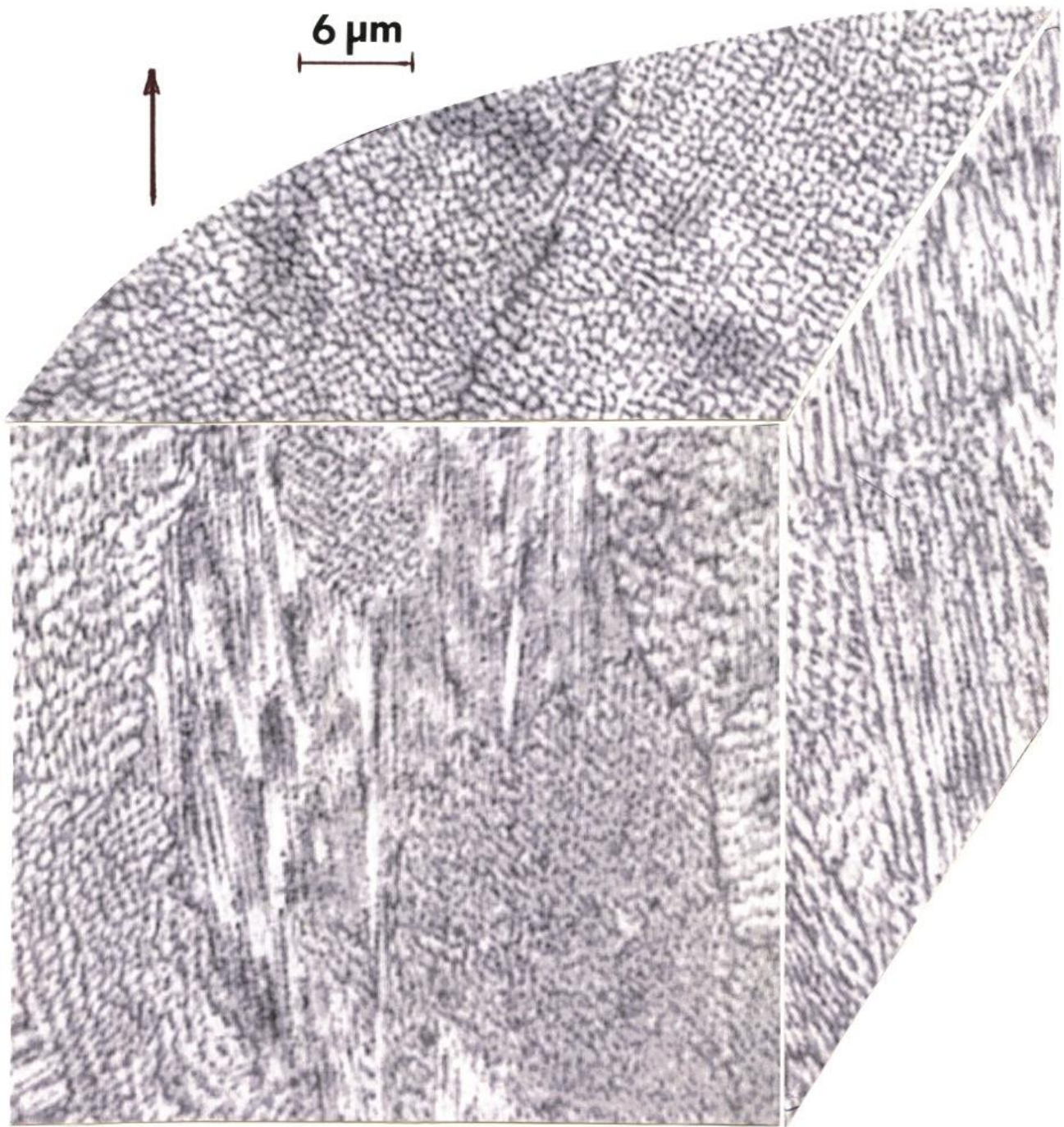


Figure 3.5. 3D optical metallograph (OM image) composite showing the details of columnar grains and fine arrays relative to the build direction shown by arrow (top left) for an as-fabricated (x-axis) cylinder in argon gas.

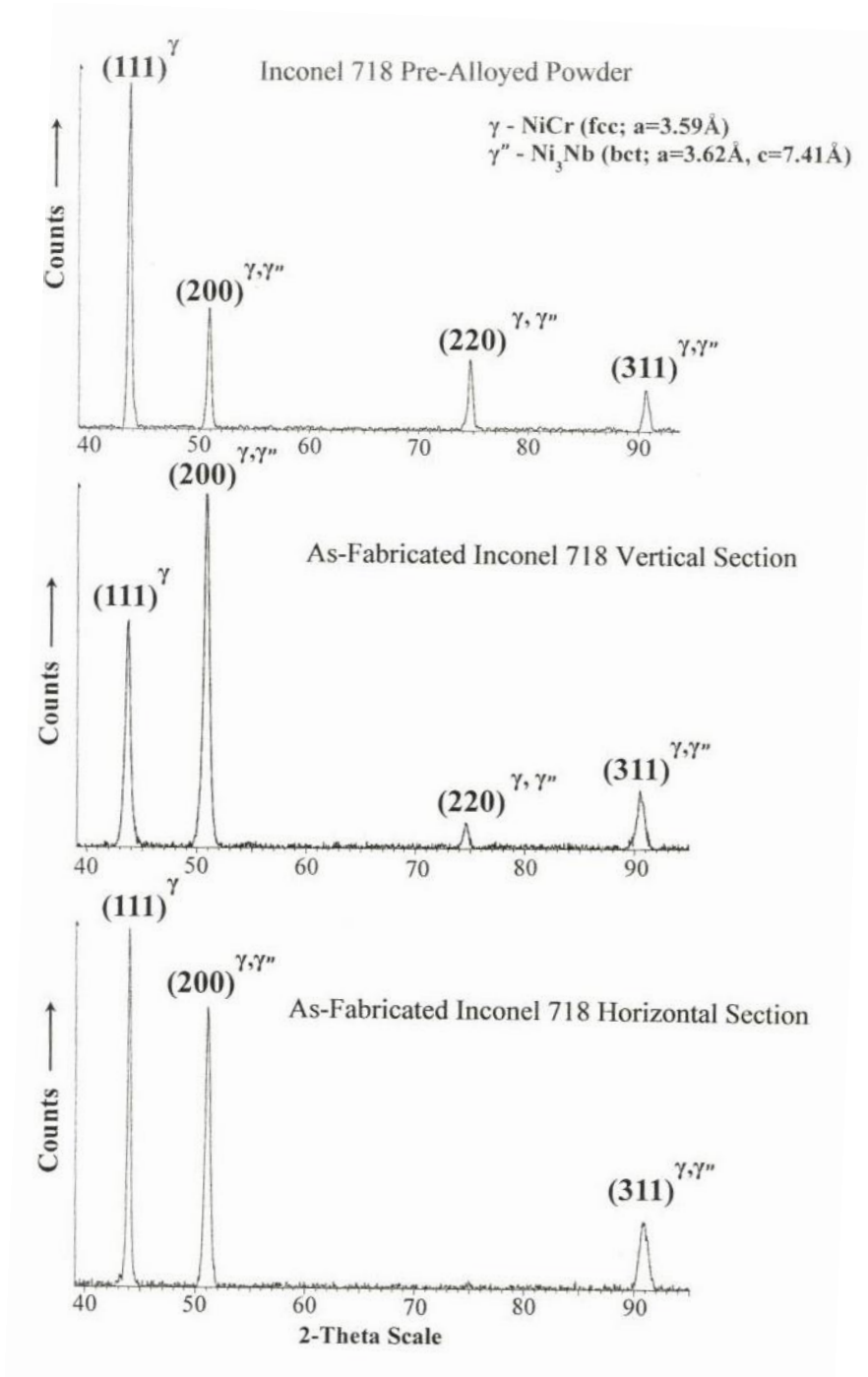


Figure 3.6. XRD spectra for (a) precursor Inconel 718 powder, (b) EBM as-fabricated (z-axis) cylinder in argon for the horizontal reference plane, (c) vertical reference plane.

Figure 3.6 compares the XRD analysis for the pre-alloyed Inconel 718 precursor powder with the

horizontal and vertical reference plane spectra for a z-axis oriented cylinder in Ar. The powder XRD spectra (Figure 3.6(a)) are coincident with solid-solution γ -fcc NiCr ($a=0.359$ nm; Space Group: Fm-3m) and exhibit a prominent (111) texture. In comparison, the XRD spectra for the as-fabricated Inconel 718 components (in both Ar and N₂) exhibited mixed (111) and (200) texture peaks in the horizontal reference plane (Figure 3.6(b)) and in the corresponding vertical reference plane (Figure 3.6(c)) for both z-axis and x-axis-oriented cylinders. The strong (200) texture is consistent with the EBM fabrication of Inconel 718 products by Strondl et al. (2008), where γ (fcc) grains were oriented with $\langle 100 \rangle$ parallel to the build direction and represented a “strong cube solidification and growth

texture, almost like a single crystal”.

The γ'' (bct) Ni₃Nb precipitate diffraction spectra coincide (or overlap) with the γ (fcc) matrix spectra as shown in Fig. 3.6(b) and (c) for $200\gamma//200\gamma''$ as well as $220\gamma//200\gamma''$.

Figure 3.7 provides a schematic composite showing these features as they relate to the scan geometry and melt-pool related layer development, as well as the columnar arrays

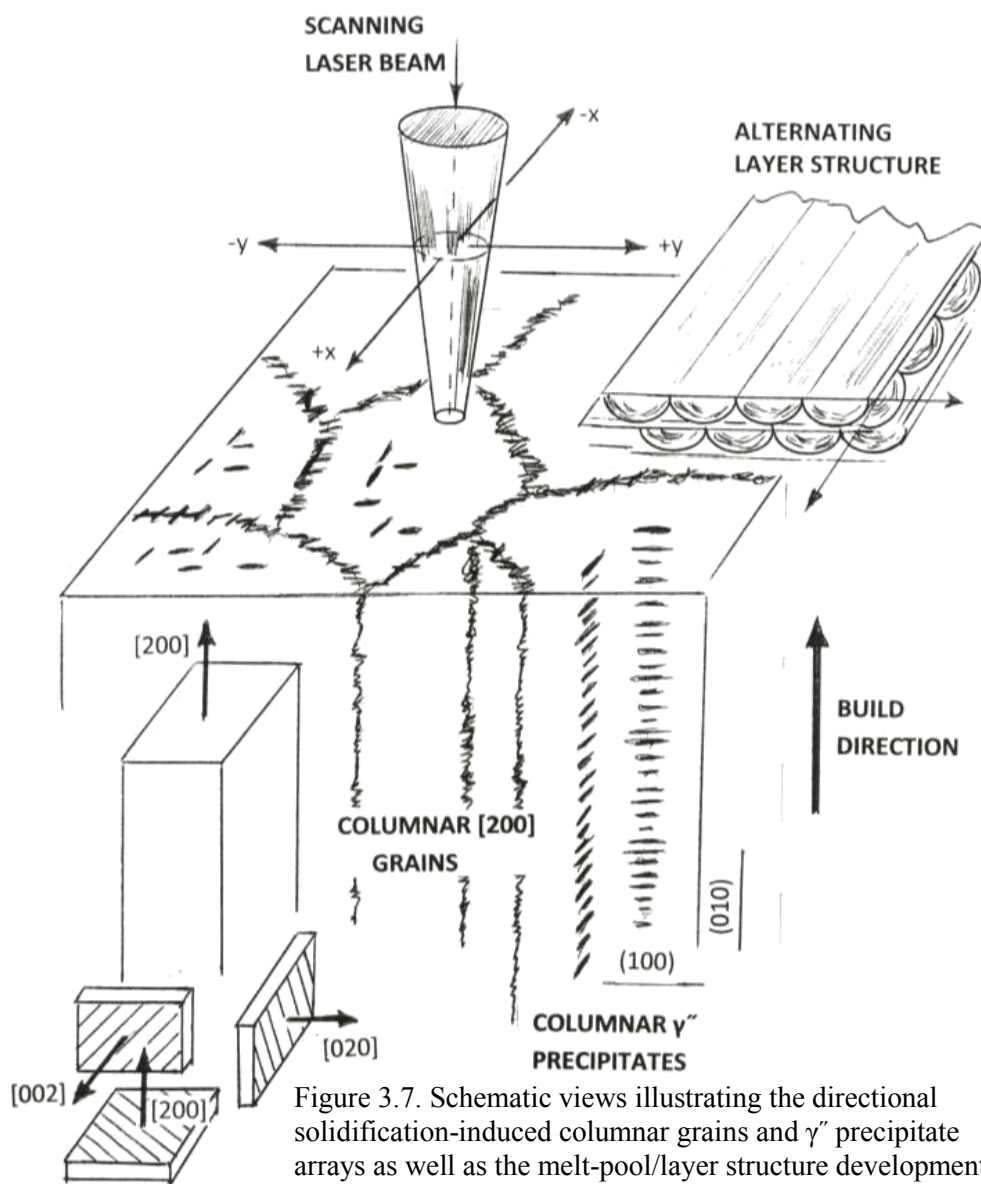


Figure 3.7. Schematic views illustrating the directional solidification-induced columnar grains and γ'' precipitate arrays as well as the melt-pool/layer structure development in SLM. The coincident plane variants for (100) [200] are shown at [002], [200] and [020].

formed as directional, epitaxial-like solidification phenomena related to the high-temperature gradients occurring during the SLM process.

Fabricated and HIPed Components

While Figure 3.5 shows these columnar architecture arrays for an x-axis cylinder built in an argon gas environment, Figure 3.8 shows a more regular columnar architecture spatially identical to Figure 3.5 for an x-axis oriented cylinder built in argon gas and HIPed at 1163°C for 4h in 0.1 GPa argon pressure, following an initial stress-relief anneal at 982°C for 0.5h. Figure 3.9 shows a similar 3D microstructural architecture composite for a z-axis oriented cylinder built in argon gas and HIPed as noted for Figure 3.8. Figure 3.10 shows a vertical section reference view for an SLM-fabricated x-axis cylinder built in a nitrogen gas environment and HIPed as noted for Figures 3.8 and 3.9. Figure 3.10 shows some recrystallized areas exhibiting a relatively uniform, dense distribution of precipitates, with remnants of the columnar microstructural architecture shown in Figure 3.5 for the as-fabricated product, and in Figures 3.8 and 3.9 for as-fabricated and HIPed products. Figure 3.11 represents a 3D composite for the as-fabricated (in nitrogen gas) and HIPed x-axis cylindrical component which is essentially identical to the 3D composite, columnar, microstructural architectures shown in Figures 3.8 and 3.9.

The columnar microstructural architectures shown in Figures 3.5, 3.8 and 3.9 to 3.11 are similar to those observed in alloy 625 components fabricated recently by electron beam melting (EBM) [8], where the columns were observed to be composed of γ'' -Ni₃Nb (bct) precipitates with spatial dimensions of $\sim 2 \mu\text{m}$, was more than twice that observed in Figures 3.5 to 3.11. Strondl et al [6] have also shown similar microstructural features in Inconel 718 fabricated by EBM, but the columnar γ'' architecture was not described in detail.

However, this does not provide unambiguous evidence for γ'' (bct) precipitation composing the columnar microstructural architectures in Figures 3.8, 3.9 and 3.11 because γ (fcc)($a=0.361 \text{ nm}$; Space Group: Fm-3m) precipitate spectra can essentially coincide with all of the γ (fcc)-NiCr matrix spectra as well as the γ'' 200 and 220 spectral peaks. Consequently, unambiguous identification of γ' and γ'' precipitates must rely on TEM observations of particle morphologies and dimensions, and especially selected-area electron diffraction (SAED) patterns and corresponding, systematic dark-field imaging as

illustrated in much earlier work on Inconel 718 ingots and related products by Paulonis et al. (1969), Kirman and Warrington (1971), Oblak et al. (1974), Sundararaman et al. (1992), and He et al. (1994).

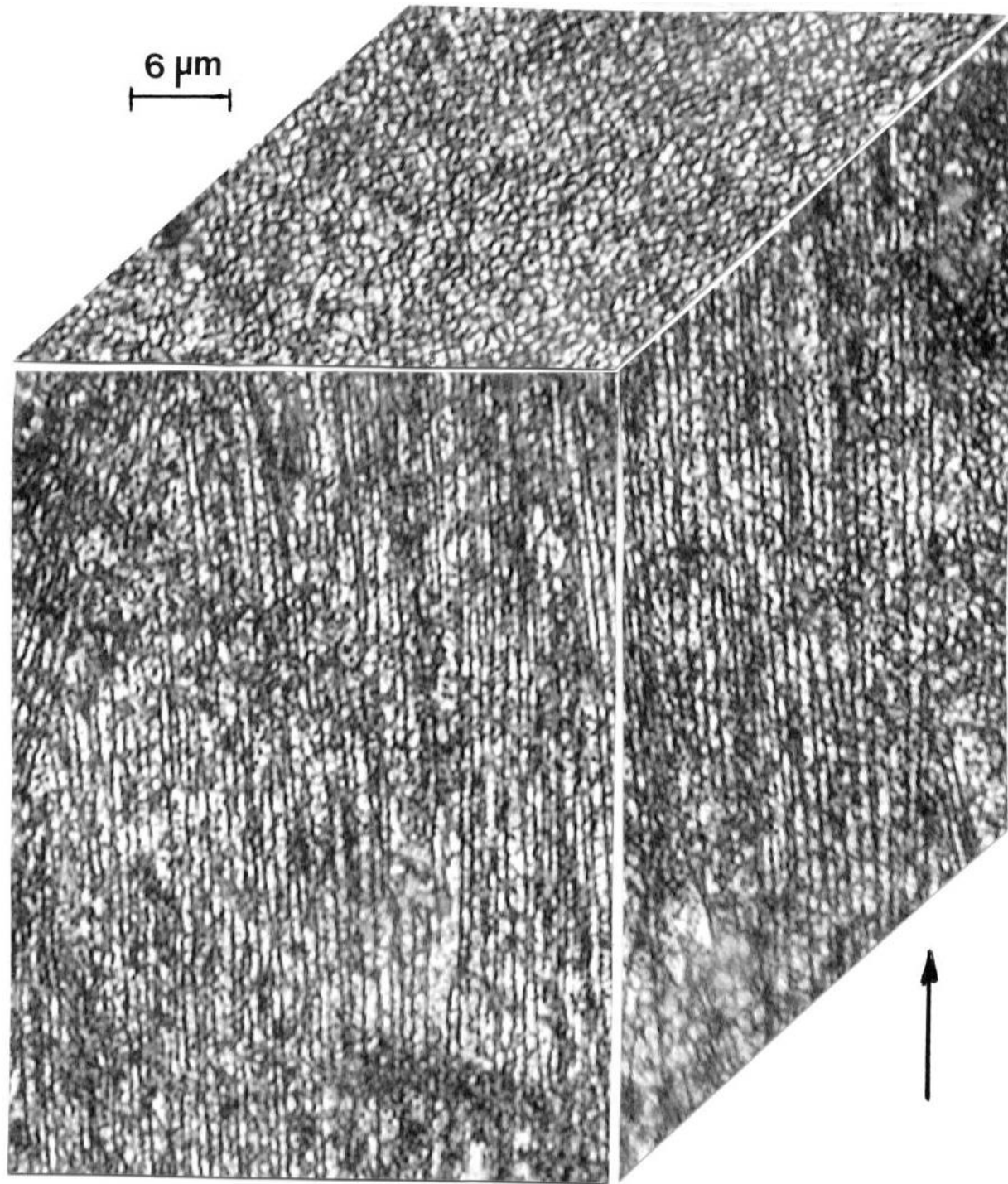


Figure 3.8. OM 3D composite view for a cylindrical component (x-axis) fabricated in argon and HIPed in argon. Build direction is noted by the arrow (bottom right).

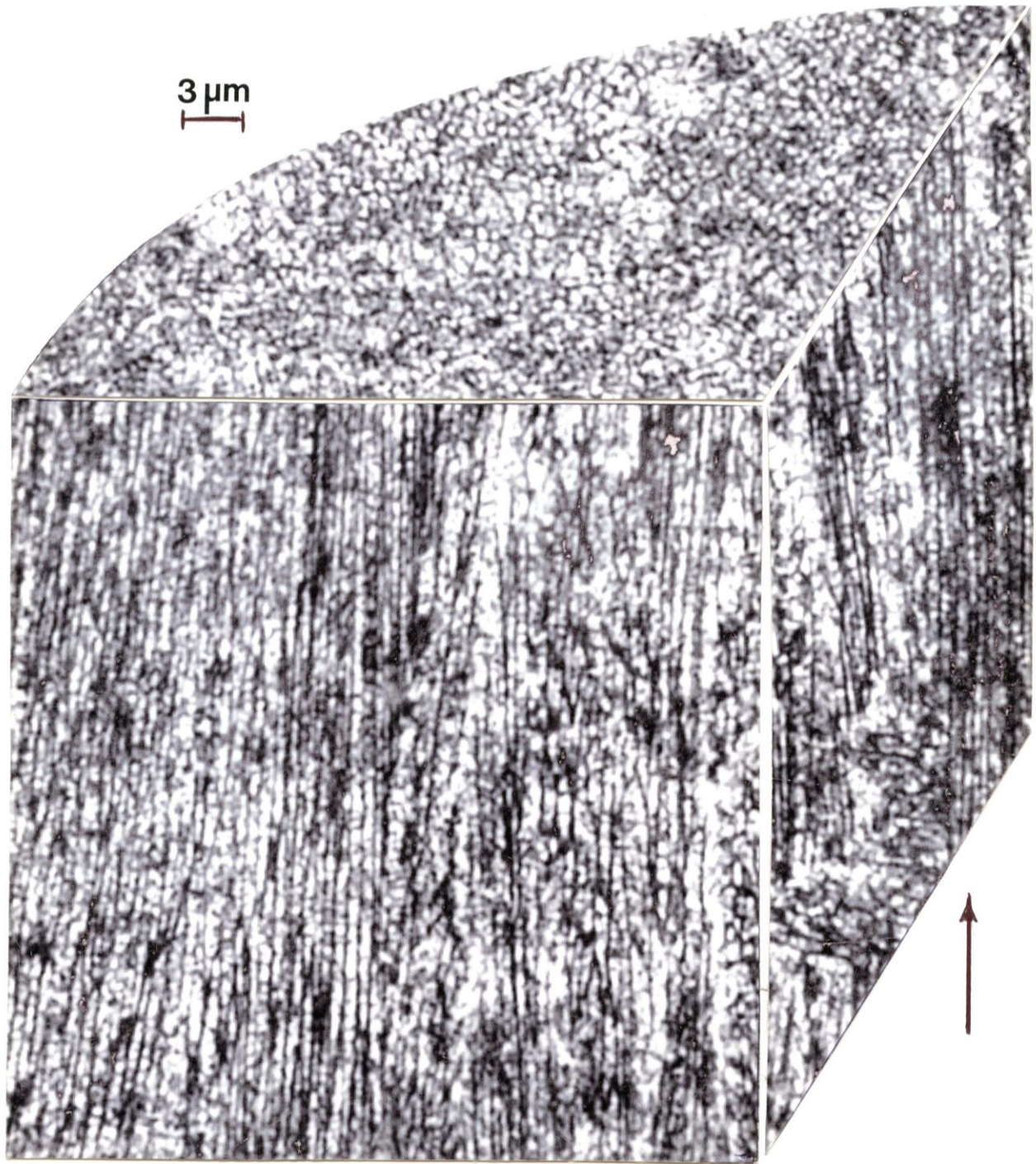


Figure 3.9 OM 3D composite view for a cylindrical component (z-axis) fabricated in argon and HIPed in argon. Build direction is noted by the arrow (bottom right).

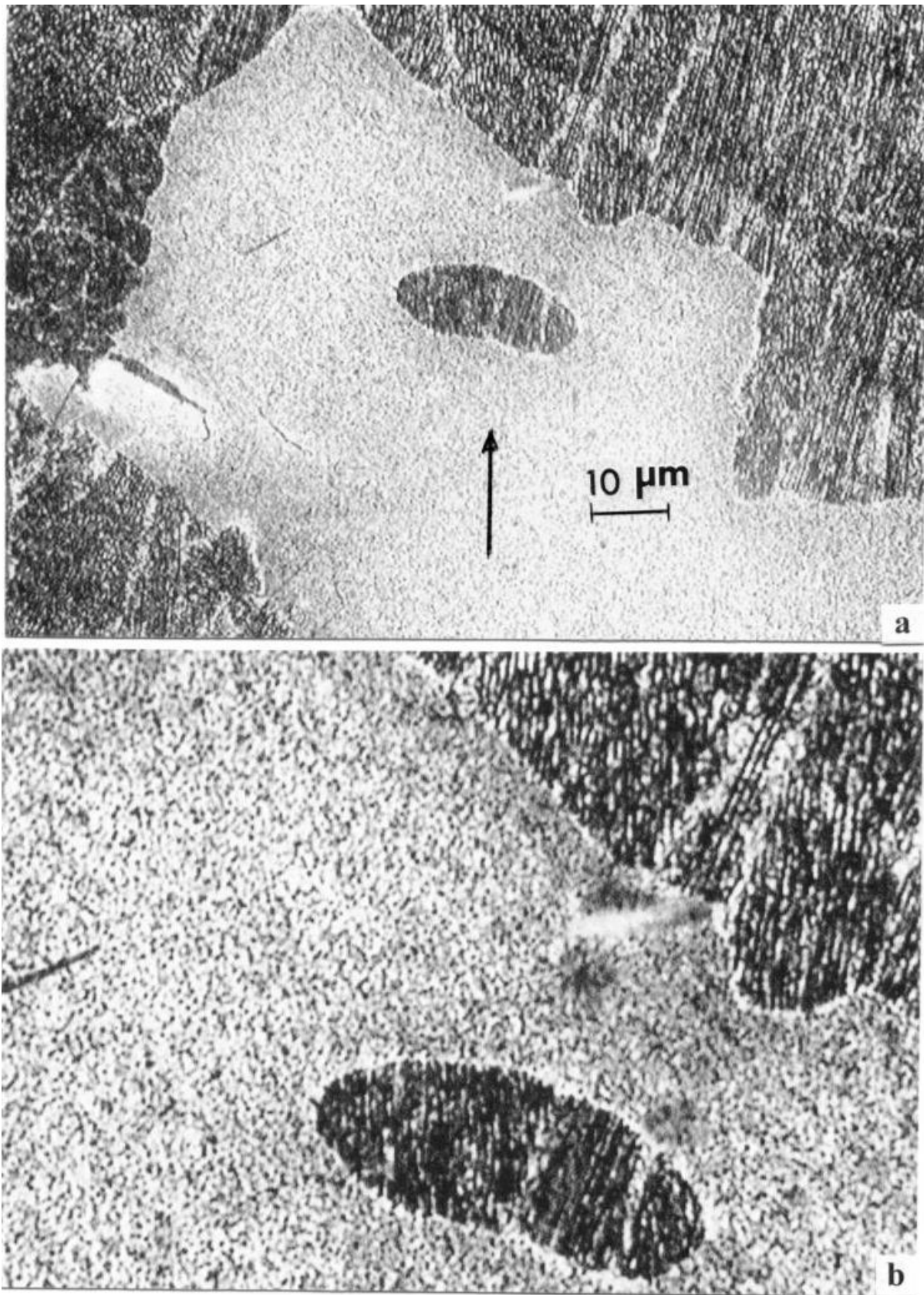


Figure 3.10. Vertical reference section (OM) views showing partial recrystallization for x-axis fabricated cylinder in nitrogen and HIPed in argon. Arrow in (a) shows the build direction. (b) shows a magnified view of (a).

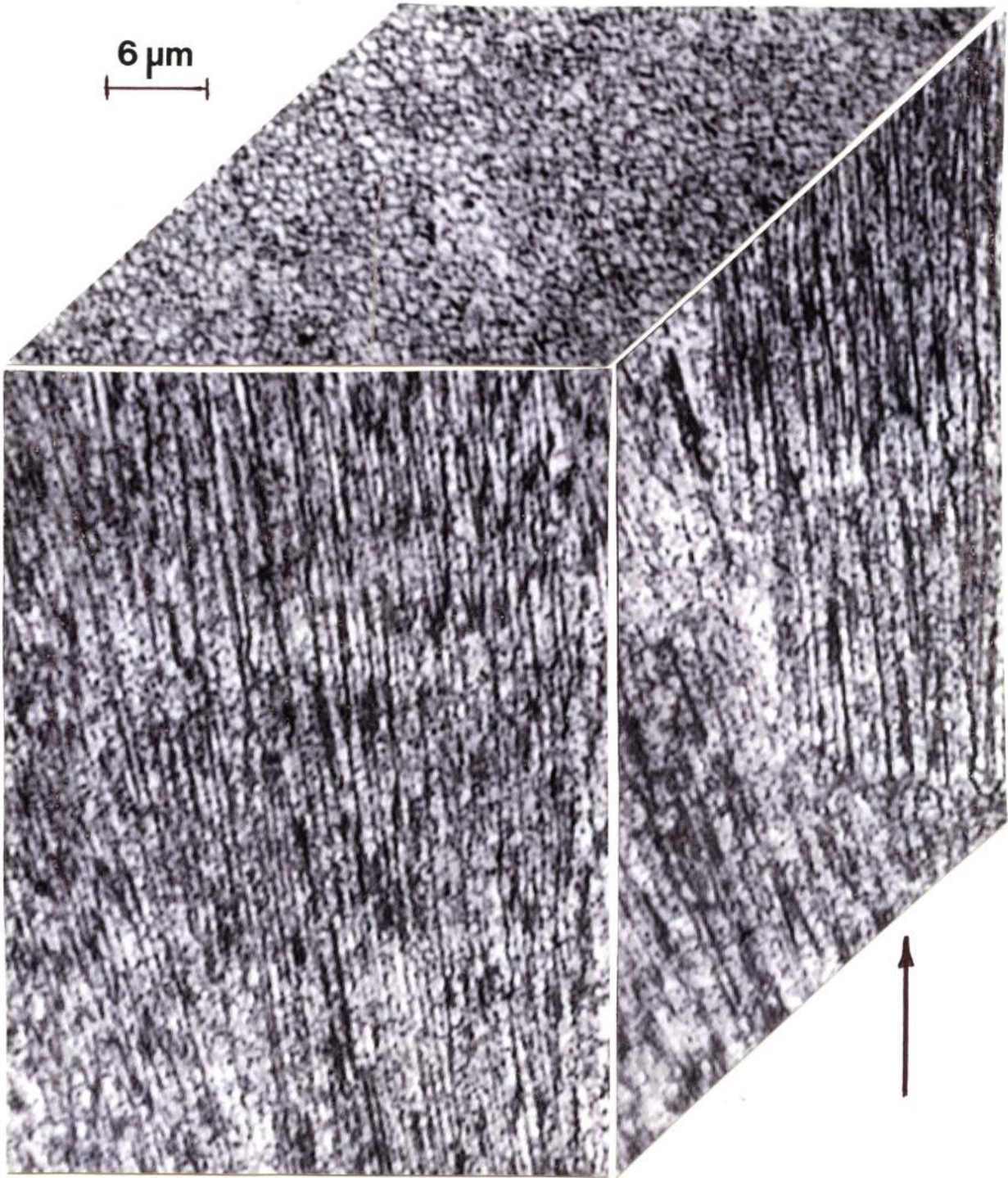


Figure 3.11. OM 3D composite view for a cylindrical component (x-axis) fabricated in nitrogen and HIPed in argon. Build direction is noted by the arrow (bottom right).

Figure 3.12 shows a magnified 3D TEM image composite corresponding to a section of Figure 3.9, which illustrates a variety of dense precipitates within these columnar [100] arrays and composing the apparent array boundaries. The horizontal surface view in Figure 3.12 shows oblate ellipsoidal or spheroidal particles as large as 250 nm (major axis dimension) immersed in a dense field of precipitates <10 nm diameter inside or in the boundaries of equiaxed arrays. Well-defined columnar arrays of elongated precipitates coincident with (100) are observed in the vertical reference plane in Figure 3.12, parallel to the build direction (arrow). These crystallographic features are shown by the (010) SAED pattern insert in the forward vertical reference plane in Figure 3.12. The columnar precipitate arrays are also parallel to columnar, very low-angle grain boundaries indicated by the arrow to the left in the vertical reference plane in Figure 3.12. From the TEM 3D composite in Figure 3.12, it is impossible to delineate between the cylindrical-like columnar precipitate arrays and the columnar grain boundaries or columnar grains many of which have a [100] (200) texture as shown in the corresponding XRD spectra in Figure 3.13. Figure 3.13 shows, in contrast to Figure 3.6(b) and (c), that the HIP-anneal process altered the texturing of the columnar precipitate arrays shown in Figures 3.8, 3.11 and 3.13, producing a dominant (200) texture in the horizontal reference plane and (200) and (220) texture in the vertical reference plane. The (200) texture is reflected in the (001) SAED pattern insert in Figure 3.12.

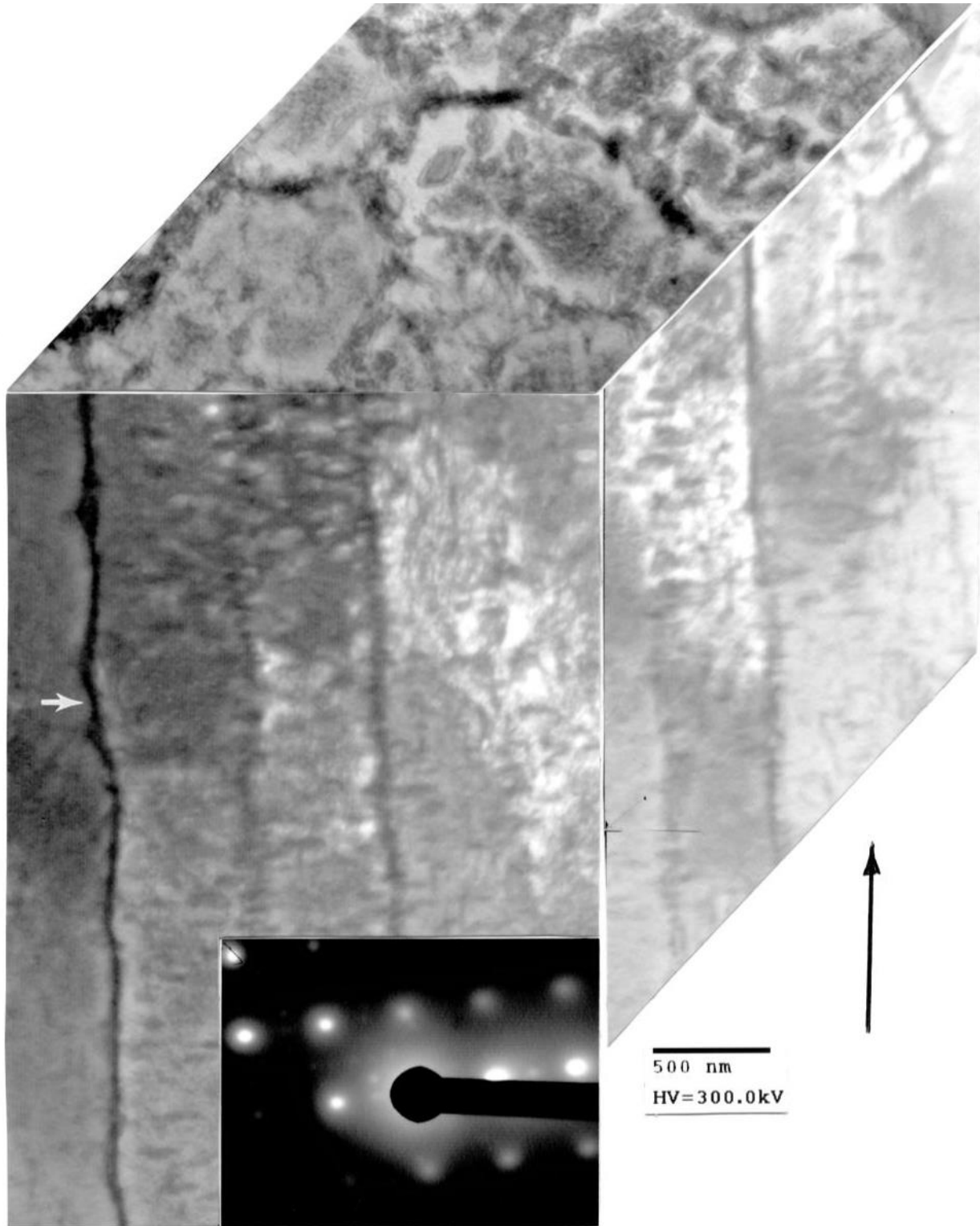


Figure 3.12. TEM-3D image composite view for an as-fabricated (in argon) z-axis cylinder HIPed in argon. The SAED pattern insert corresponds to a $\gamma[001]$ zone in the vertical reference plane as shown. The arrow to the right indicates the build direction.

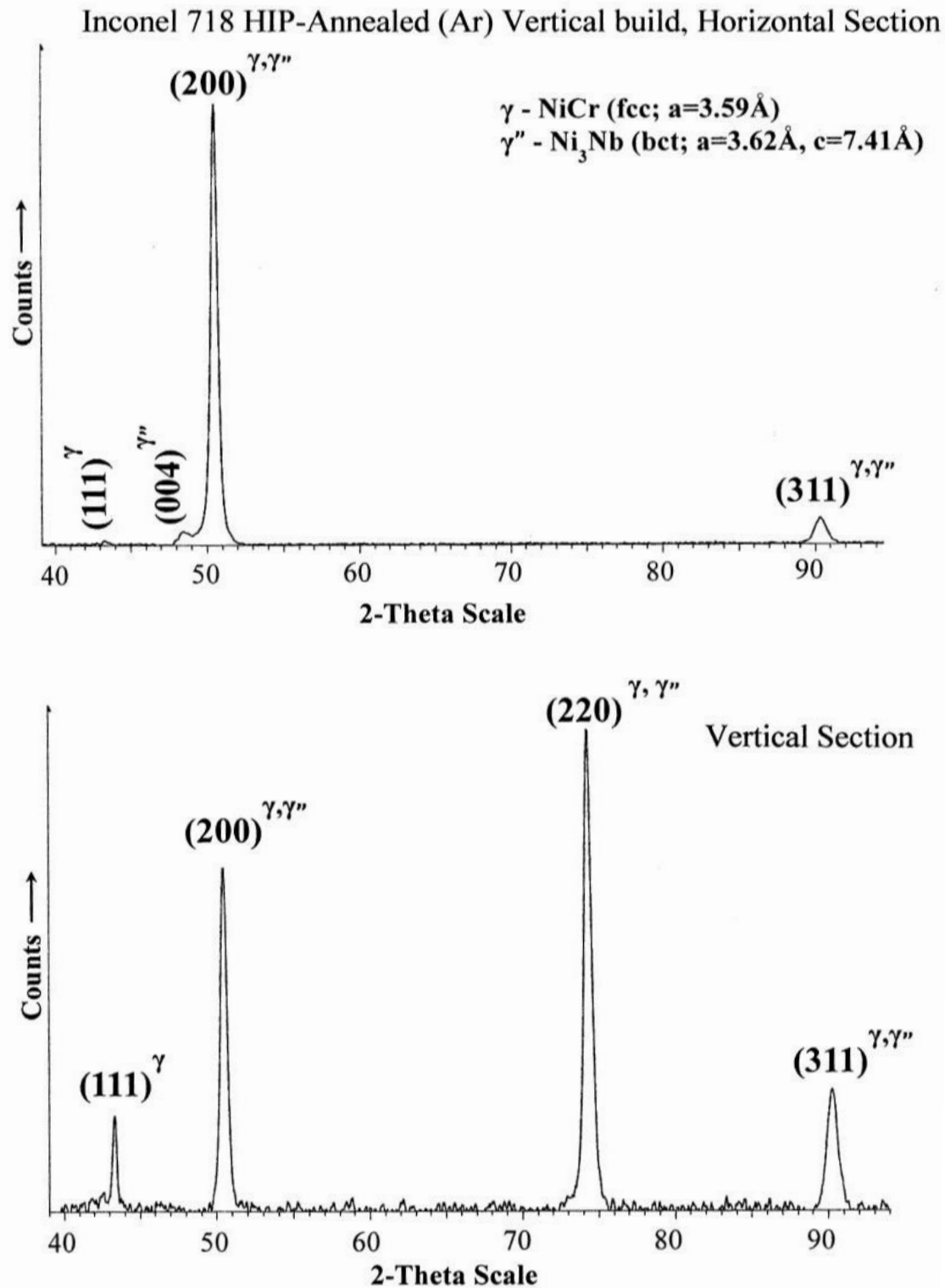


Figure 3.13. XRD spectra representing as-fabricated and HIPed (in argon) z-axis oriented specimen. (a) Horizontal reference plane (normal to the build direction). (b) Vertical reference plane (parallel to the build direction).

Figure 3.14 shows the details of a vertical reference plane section of columnar precipitates stacked like dinner plates, and coincident with the fcc matrix (100) planes. The elongated precipitates appear to be oblate spheroids or ellipsoids with the long axis (major axis dimension) coherent with the (100) planes of the fcc (NiCr) matrix. This is observed from the SAED (001) diffraction pattern insert, which clearly shows the γ'' (bct) diffraction spots and streaking of these spots in the [100] direction perpendicular to the major axis of the precipitates. Only the {100} (shown at (1) in Figure 3.14) and $\{\frac{1}{2} 1 0\}$ and $\{1 \frac{1}{2} 0\}$ type (bct) superlattice reflections (shown at (2) in Figure 3.14) for γ'' precipitates appear in the SAED pattern insert in Figure 3.14. The columnar stacks of γ'' precipitates in Figure 3.14 (parallel to the build direction shown by the arrow) are ~250 nm wide, with precipitate thicknesses of ~25-50 nm, spaced the same distance. In Figure 3.14, the propensity of γ'' precipitates are coincident (coherent) with the (100) planes while some are observed to be coincident with the other (010) variant. Dense and often irregular arrangements of various geometries and very small (regular) sizes of precipitates (γ'') also occur throughout the NiCr (fcc) matrix.

In retrospect comparing and examining Figures 3.3, 3.5, 3.6, 3.9 and Figures 3.11- 3.14 provides for a conceptual, mechanistic view of the SLM build process producing columnar (textured) grains and γ'' precipitate arrays.

The stacks of disc-like or oblate spheroidal γ'' precipitates implicit in Figure 3.14 appear to be created in successively formed melt pools as a consequence of their short interaction times and high conductive heat transfer, possibly facilitated by the argon or nitrogen gas environments, or their corresponding thermal conductivities. In this regard, it is interesting to consider that while the thermal conductivity (K_T) of nitrogen and argon gas is $0.026 \text{ Wm}^{-1}\text{K}^{-1}$ and $0.018 \text{ Wm}^{-1}\text{K}^{-1}$ respectively at 300 K, they both increase linearly up to more than 2000 K (Faubert 1972). Correspondingly, $K_T(\text{N}_2)/K_T(\text{Ar}) \cong 1.4$. While we have not observed any notable microstructural variances between specimens fabricated by SLM in nitrogen versus argon gas (corresponding Figures 3.8 and 3.11 for example), there may be subtle difference in properties for components fabricated in these gases utilizing the same build or scan strategies (or parameters).

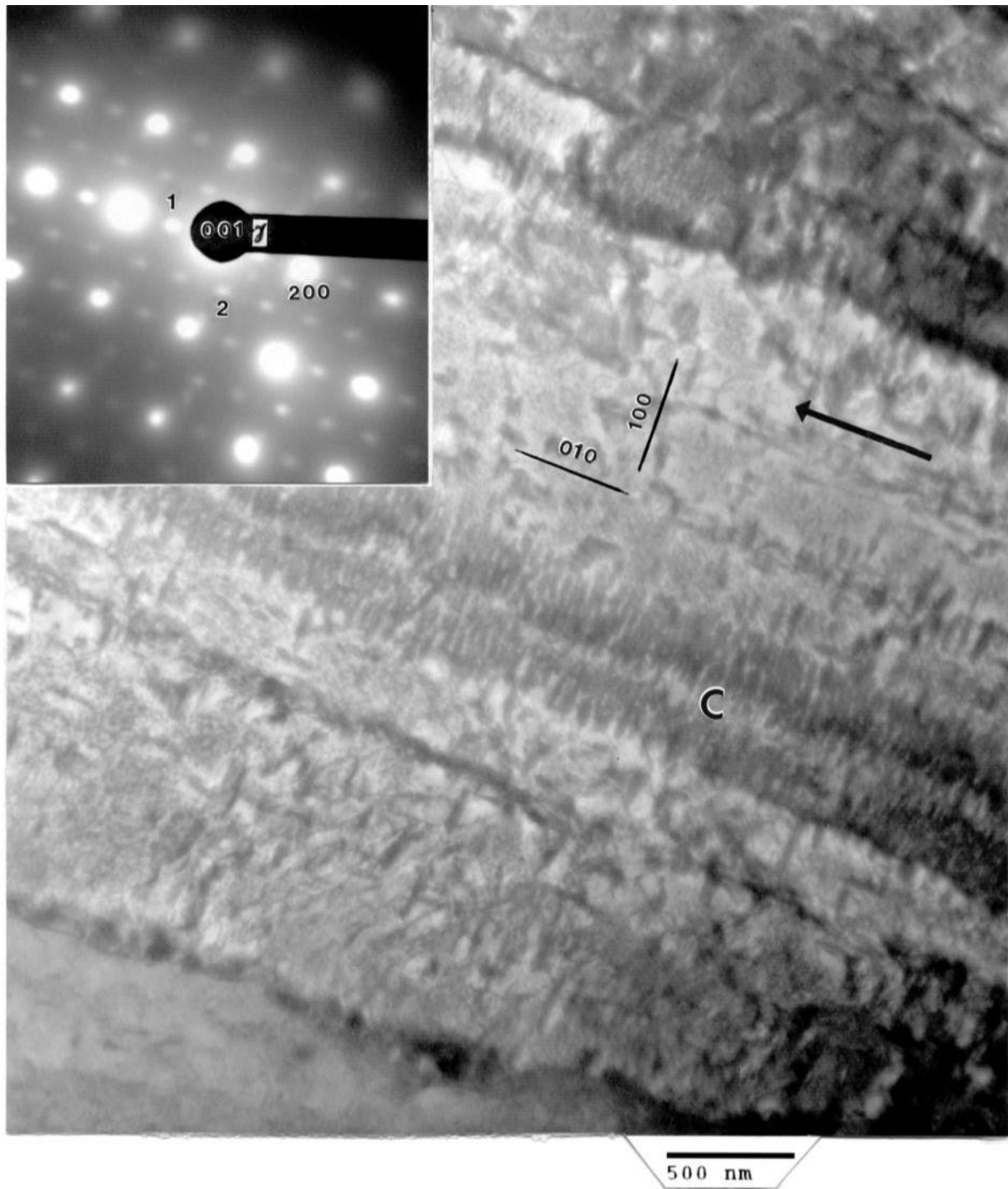


Figure 3.14. Magnified TEM bright-field image for a vertical reference plane section corresponding to Fig. 3.12. Lenticular-like/oblate ellipsoidal γ'' precipitates are coherent with $\{100\}$ planes in two prominent columns (c) which are parallel to the build direction noted by large arrow. Some precipitates are coincident with the $\{010\}$ variant shown. The SAED pattern insert shows a γ $[001]$

zone axis. γ'' $\langle \bar{1}00 \rangle$ and $\langle 1 \frac{1}{2} 0 \rangle$ reflections are noted by spots designated 1 and 2, respectively.

Fabricated and Annealed Components

While the HIPed-annealed specimens were only slightly recrystallized as shown in Figure 3.10, the recrystallized regions exhibited a dense, homogeneous precipitate distribution (Figure 3.10 (b)). However, the recrystallization was considerably more extensive for the as-fabricated components annealed in Ar at standard pressure for 4h at 1160°C. This feature is illustrated in Figures 3.15 and 3.16(a), which show corresponding horizontal and vertical reference plane observations for an x-axis cylinder fabricated in argon. Because of the etching, only traces of recrystallized grain boundaries are observed in Figure 3.15, while Figure 3.16(a) shows remnants of the melt pool-layering in the vertical plane parallel to the build direction noted by the arrow. By tailoring the etchant (5% HCl plus 95% water) and electroetching at 4V for 0.5 to 1 minute, both the recrystallized (NiCr-fcc) matrix grain and coherent twin boundary structure could be observed as shown in Figure 3.16(b).

Figure 3.17 shows, for comparison with Figures 3.5, 3.8, 3.9 and 3.11, a 3D composite view typical for the as-fabricated and annealed cylindrical samples. The unrecrystallized columnar γ'' precipitate zones (C) can be observed in contrast to the recrystallized and re-precipitated fcc matrix (R) where in contrast to the coherent γ'' oblate spheroidal/ellipsoidal precipitates in the columnar arrays, the precipitates in the recrystallized matrix in Figure 3.17 are more regular (cuboidal or spherical), with apparent diameters from Figure 3.17 of $\sim 300\text{nm}$. XRD spectra obtained for the horizontal and vertical reference planes corresponding to Figure 3.17 were, as shown in Figure 3.18, similar to those representing the as-fabricated and HIPed components shown in Figures 3.6 and 3.13, respectively, except for the variations in texture as a consequence of the more extensive recrystallization apparent in Figure 3.17. The XRD spectra corresponding to Figure 3.17 and shown for the horizontal and vertical reference planes in Figure 3.18, are similar to those for the HIP-annealed components illustrated in Figure 3.13. There is some additional prominence of (111) in both reference planes and some additional (200) and (220) prominence in the vertical reference plane for both Figures 3.13 and 3.18. Both Figures 3.13 and 3.18, representing annealing of the as-fabricated components, show some recognizable variances in spectral peak prominence, especially the suppression of (111), and recognizable prominence of (220) in the vertical reference plane parallel to the build direction. Figure 3.13(a) shows a (004) γ'' peak not present in other XRD spectra (Figures 3.6 and 3.18), while Figure 3.18 (b) shows a new peak

for the Ni_3Nb orthorhombic (δ) phase indexed as (201) δ ($a = 0.51$ nm, $b = 0.42$ nm, $c = 0.45$ nm; Space Group: Pmmn). The δ -phase is also referred to by some investigators as the β -phase [13]. While the precipitates distributed within the recrystallized regions (marked R in Figure 3.17) may be γ' (fcc- Ni_3Nb), the corresponding spectral peaks overlap the fcc NiCr matrix peaks since the lattice parameters only differ by 0.012 nm (0.3%). Correspondingly, except for the (004) γ'' spectral peak in Figure 3.13(a), there is no clear delineation of the precipitate identity in the XRD patterns (Figures 3.6, 3.13 and 3.18) as noted previously.



Figure 3.15. Horizontal reference plane (OM) view for recrystallized microstructures following as-fabricated (argon) and annealed treatment (argon) for an x-axis oriented cylinder.

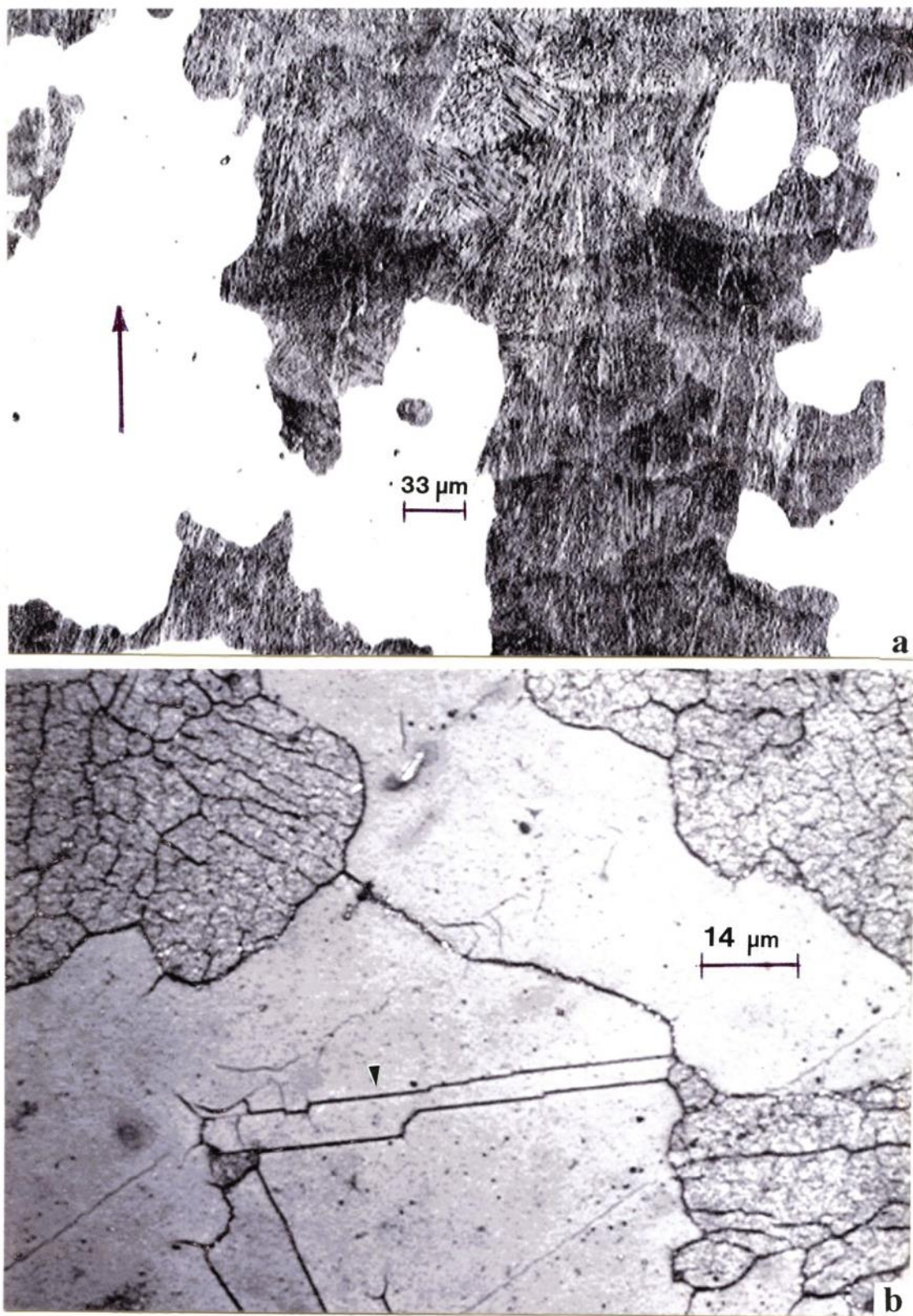


Figure 3.16. (a) Vertical reference plane (OM) view for recrystallized microstructures corresponding to Figure 3.15, showing melt pool interaction and layering in remnant columnar microstructure. Arrow denotes the build direction. (b) Horizontal plane reference (OM image) corresponding to (a) etched to reveal the recrystallized grain and annealing twin (γ) boundaries (arrow).

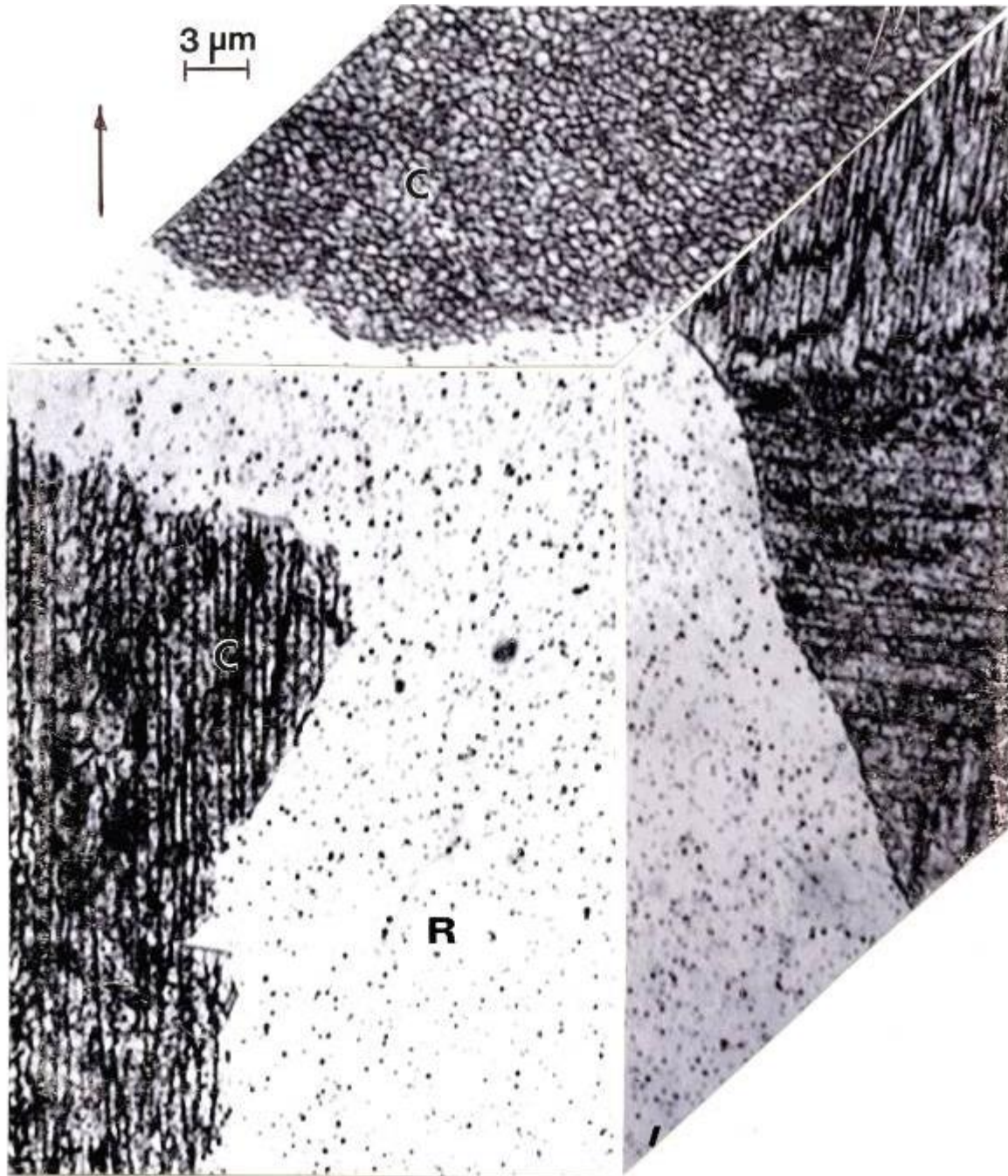


Figure 3.17. OM 3D composite view for the annealed (4h @1160°C) argon-fabricated, x-axis cylinder. The recrystallized regions are denoted R. Selective etching reveals homogeneous globular precipitates. C indicates the original (remnant) columnar microstructural architecture arrays. Arrow at upper left denotes the build direction.

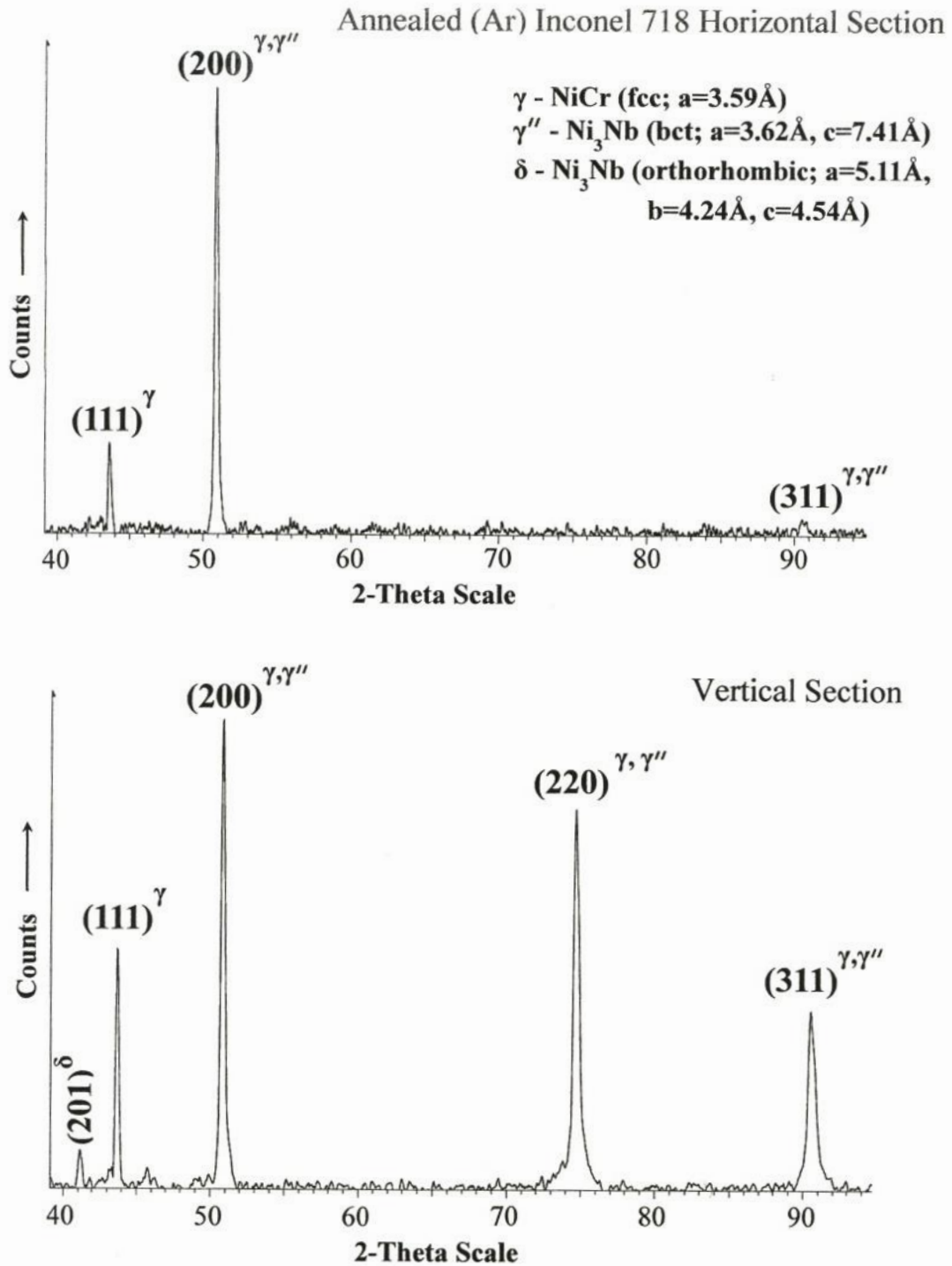


Figure 3.18. XRD spectra representing the as-fabricated and annealed (4h @1160°C) specimens corresponding to Fig. 3.17. (a) Horizontal reference plane. (b) Vertical reference plane.

Figure 3.19 illustrates this feature for a typical recrystallized region in the horizontal reference plane characterized by Figure 3.17. The magnified TEM image portion in Figure 3.19 shows oblate ellipsoidal γ'' precipitates having an average minor axis dimension of ~ 7 nm and a major axis coincident with $\{001\}$ of ~ 35 nm, or a ratio $D/d = 5$. The reduced magnification dark-field image insert in Figure 3.19 shows these aligned γ'' precipitates using the $[00\bar{1}]$ reflection indicated by the small arrow in the SAED pattern insert in Figure 3.19. The white arrow in Figure 3.19 illustrates the $[00\bar{1}]$ direction, which is perpendicular to the coincident (001) planes. This dense γ'' precipitate occurrence is similar to observations of Slama et al. (1997) for aging of Inconel 718 at 750°C for 4h to 98h and He et al. (1994) for solution treatment of alloy 718 up to 1050°C for 1h. The interesting feature of the present observations (in Figure 3.19) is the dense arrangement of fine γ'' precipitates which have re-precipitated 100°C above this temperature, although the 4h anneal corresponded to the aging time for the optimum volume fraction of precipitates. The γ'' precipitate dimensions shown in Figure 3.19 are also consistent with those observed for alloy 718 aging at 750°C for 4h (Slama, et al. 1997), and up to 1050°C for 1h (He, et al. 1994).

The occurrence of the δ -phase (or β -phase: orthorhombic – Ni_3Nb) in the XRD spectrum of Figure 3.18 was observed at grain boundaries or more specifically those boundaries characterizing the recrystallization front separating the unrecrystallized γ'' regions from the recrystallized regions illustrated typically in Figure 3.17, as shown in Figure 3.20. The magnified and tilted views of 3.20 (a), 3.20(b) and 3.20(c), respectively, show a denuded zone surrounding a δ -phase precipitate from a high density of coherent γ'' -phase fine precipitates in the recrystallized region. This interfacial occurrence of δ precipitates is characteristic of many earlier observations in grain boundaries of annealed, wrought Inconel 718 alloy (Sundararaman, et al. 1992, He, et al. 1994, Slama, et al. 1997, Azadian, et al. 2004, Li, et al. 2002).

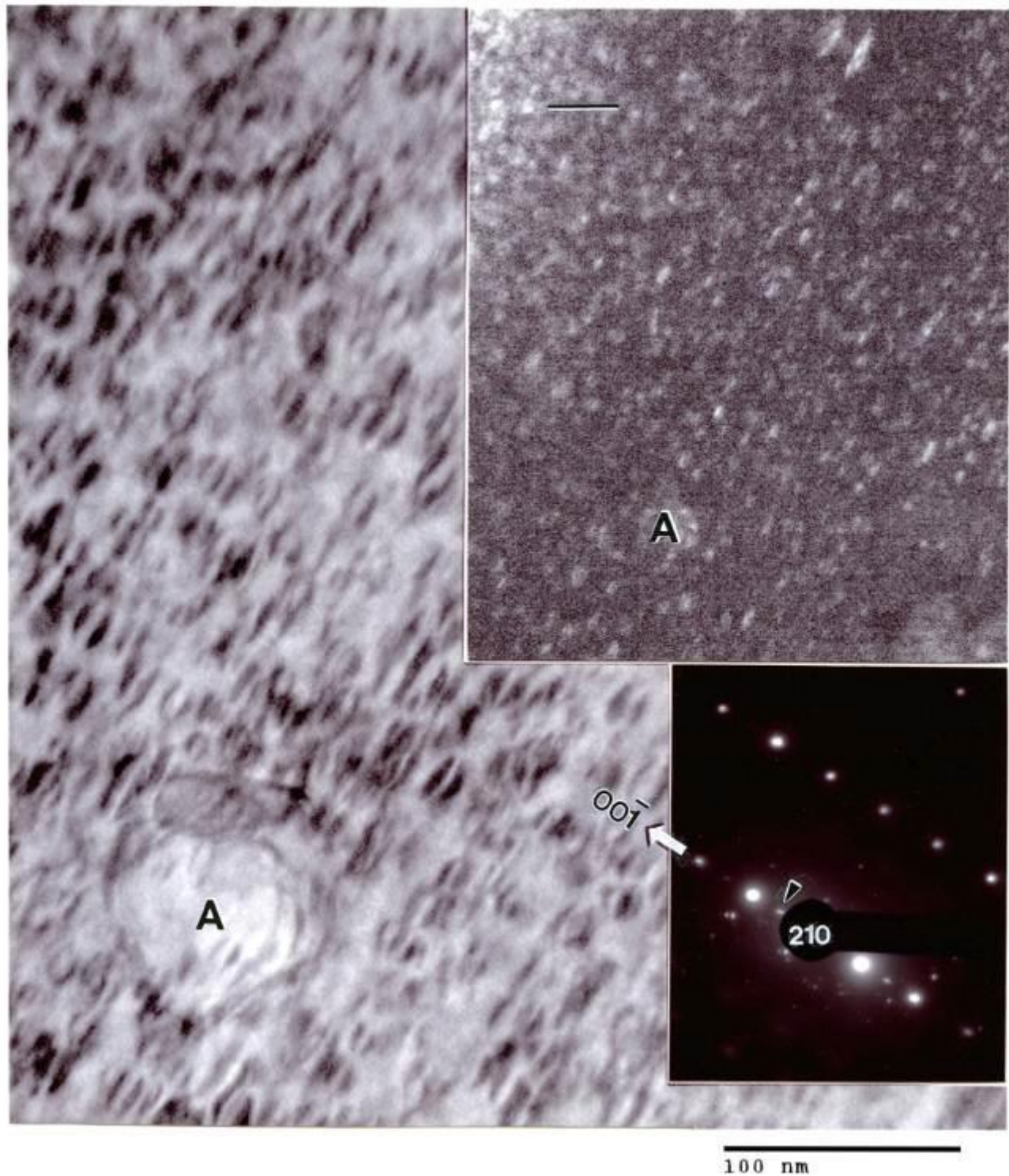


Figure 3.19. TEM observation of dense γ'' precipitation in recrystallized regions for annealed SLM-fabricated Inconel 718. The enlarged view shows oblate ellipsoidal γ'' precipitates coincident with (001) (or $(00\bar{1})$) planes while the lower magnification dark-field image insert shows these precipitates imaged with the $[00\bar{1}]$ (bct) reflection at small arrow in the SAED pattern insert. The surface orientation is noted as the $[210]$ fcc zone. A indicates a common reference for the enlarged view and the reduced magnification, dark-field image insert. Note the magnification bar in the dark-field insert is the same as shown in the bright-field image.

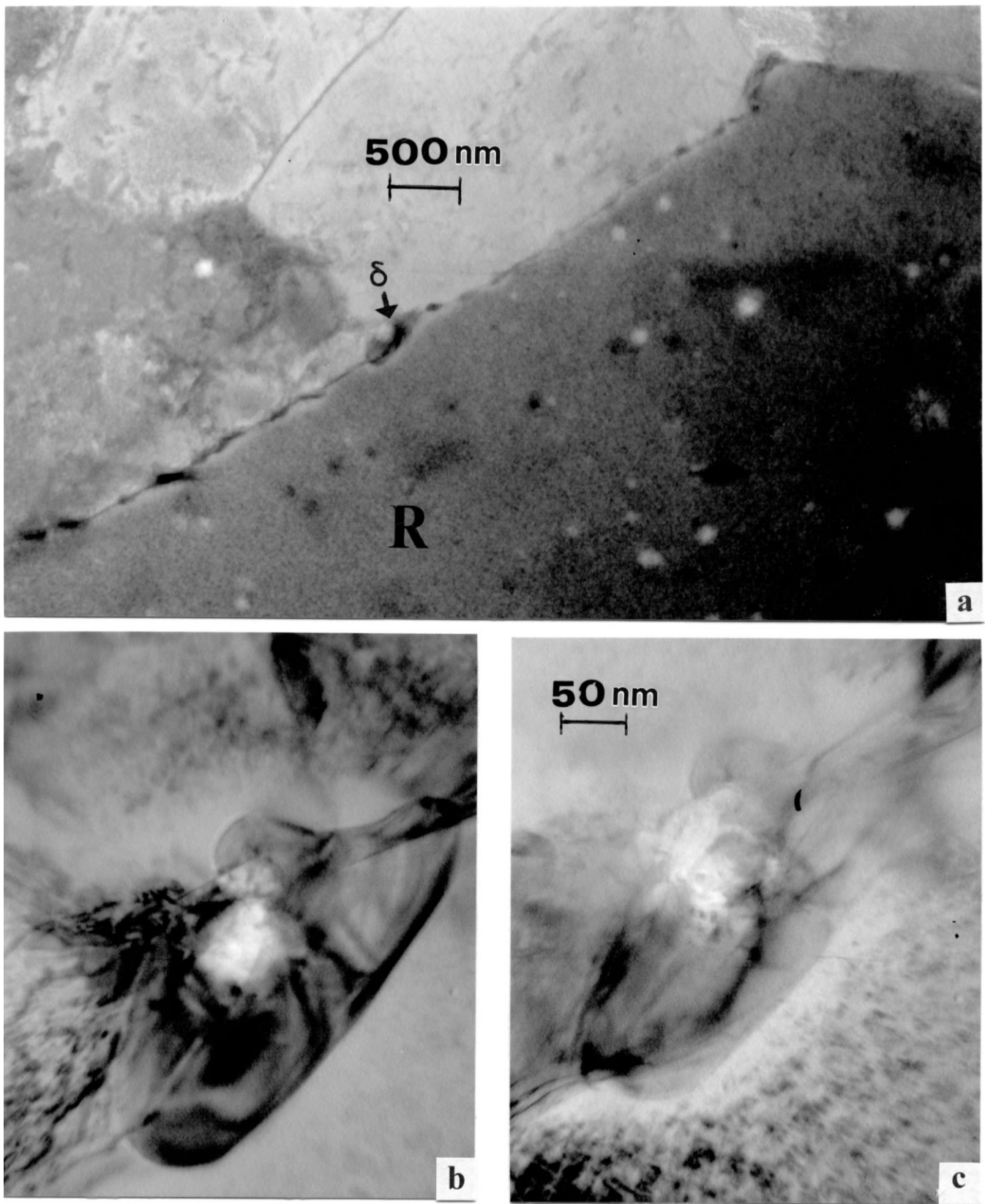


Figure 3.20. δ precipitate at a grain boundary separating an unrecrystallized grain from a recrystallized grain. (a) shows recrystallized grain as (R). (b) magnified view of precipitate. (c) tilted view of (b).

3.2.2 Mechanical Behavior

Wrought Inconel 718 has been largely used in critical components for turbine engine fabrication because of its relatively high mechanical properties up to about 700°C. The γ'' -phase has been the principal strengthening agent (Sundararaman, et al. 1992, He, et al. 1994, Slama, et al. 1997, Azadian, et al. 2004, Li, et al. 2002), especially during isothermal aging in the 550°C to 900°C temperature range (Slama, et al. 1997, Li, et al. 2002, Eiselstein 1965). While the present study has not involved systematic aging, hardness and tensile measurements have been made and compared as illustrated in Table 3.1.

Table 3.1 compares hardness (both Vickers (HV) and Rockwell C-scale (HRC)) measurements along with tensile behavior for SLM-fabricated cylinders, fabricated and HIPed cylinders, and fabricated and annealed cylinders at selected orientations and in argon or nitrogen gas atmospheres. These selected measurements are also compared with nominal wrought and annealed Inconel 718 and aged alloy 718 mechanical behaviors. It is observed that the Vickers microindentation hardness for the SLM-argon-fabricated x-axis cylinder components averaged ~ 3.9 GPa for the horizontal and vertical reference planes while the corresponding HIPed component averaged 5.7 GPa, in contrast to 4.6 for the SLM-fabricated and annealed (4h @ 1160°C) component. These hardness results can be compared to the microindentation hardness evolution for isochronal tempering (@4h) of wrought Inconel 718 in the temperature range of 500 to 850°C by Slama et al. (1997). In this work (Slama, et al. 1997), the hardness (HV) between 500°C and 600°C remained constant at 2.8 GPa while samples quenched from 990°C had a hardness of 2.5 GPa. After tempering at 650°C, the hardness was 3.5 GPa. The maximum hardness of 4.7 GPa occurred at 750°C, decreasing to 4 GPa at 800°C @4h and to 2.8 GPa at 850°C. Corresponding HRC values for the SLM-fabricated components as well as the HIPed samples averaged 32 HRC and 40 HRC, respectively in contrast to wrought, annealed and aged values of 24 HRC and 45 HRC, respectively.

While the measured hardnesses in Table 3.1 for the SLM-fabricated and treated component cylinders are comparable to wrought Inconel 718 behavior, the yield (Y) and ultimate tensile strength (UTS) slightly exceed the wrought-annealed products, while the elongation is essentially the same. However, the aged, wrought Inconel 718 strength (yield and UTS) exceeds the SLM-fabricated and treated products,

although the elongation is significantly reduced. There is a consistent variance of yield and UTS for the x-axis oriented specimens and the z-axis oriented specimens (between 5 and 6 percent) for both the argon atmosphere fabricated cylinders and the nitrogen atmosphere fabricated components. This difference is due primarily to the variance in the directional, columnar grain and γ'' microstructural architecture relative to the tensile axis. While there is a comparable variance in the 0.2% offset yield strength between the argon and nitrogen gas atmospheres, there is no corresponding UTS or elongation variance, and it is concluded that the gas environment (argon or nitrogen) did not significantly influence the corresponding SLM-built components. There were also no corresponding microstructural (γ'') variances for specimens fabricated in argon or nitrogen, and correspondingly treated.

3.3 Summary

The SLM fabrication of cylindrical components of Inconel 718 from pre-alloyed powder in both argon and nitrogen atmospheres produces an unusual, columnar microstructural architecture composed of primarily $\langle 200 \rangle$ textured γ'' -phase precipitate columns within directionally solidified and similarly textured grains. The γ'' -phase ($\text{bct-Ni}_3\text{Nb}$) precipitates were coincident and coherent with the $\gamma(\text{fcc})$ matrix $\{001\}$ and $\{010\}$ planes for $[200]$ and $\{100\}$ as well for $[020]$ or $[002]$ texture. These findings are completely consistent with wrought Inconel 718 alloy characterized in detail over the past several decades.

In the as-fabricated form, the γ'' -phase precipitates are oblate spheroids/ellipsoids nominally measuring 100 nm in the major axis dimension (D) and 25 nm in the minor axis dimension (d): $D/d = 4$. The corresponding microindentation hardness for specimens fabricated as horizontal cylinders with their axis perpendicular to the scan build direction (x-axis orientation) was 3.9 GPa. Upon HIPing in argon at 1163°C for 4h (preceded by a stress-relief anneal at 982°C for 0.5h) the Vickers microindentation hardness increased to 5.7 GPa for the same cylinder orientation. There was a marked preference for $\langle 200 \rangle$ texture and the γ'' -phase precipitate columns become more regular, producing arrays spaced $\sim 0.8 \mu\text{m}$. HIPing also resulted in a 5 to 10 percent volume fraction of recrystallized material where the γ'' -phase precipitate columns dissolved, and a homogeneous precipitation of primarily coherent, spherical or cuboidal-like precipitates occurred. There was a 5 to 6% variance in the strength of cylinders

fabricated in the x-axis orientation (normal to the build direction) or the z-axis orientation (parallel to the build direction) as a consequence of the orientation of the columnar γ'' -phase architecture: parallel to the z-axis cylinders axis, and perpendicular to the x-axis cylinder axis; correspondingly parallel and perpendicular to the tensile axes, respectively.

SLM-fabricated and annealed (1160°C @ 4h) cylinders exhibited a much higher volume fraction of recrystallized γ (fcc) material (> 50%) and characterized by the same homogeneous distribution of spherical γ' precipitates along with a few volume percent of δ -phase (orthorhombic) Ni_3Nb nucleated at the unrecrystallized/recrystallized grain boundaries (interfaces). There was a small (~ 25 nm) wide denuded zone separating these δ -phase precipitates from a high density of coherent γ'' -phase precipitates composing the background of the recrystallized areas, in which the homogeneous, cuboidal/spherical γ' precipitates occurred. These fine γ'' precipitates averaged 35 nm along their major axis dimension and ~ 7 nm along the minor (oblate) axis dimension: $D/d = 5$; in contrast to the larger precipitate sizes in the as-fabricated and as-fabricated and HIPed components noted above. The corresponding microindentation hardness (HV) was 4.6 GPa, about 24% lower than the HIPed samples but still 18% higher in contrast to the as-fabricated samples. There was no apparent or consistent variance in mechanical behavior for Inconel 718 alloy components fabricated in argon gas in contrast to nitrogen gas.

Table 3.1 Mechanical properties for Inconel 718 cylindrical components fabricated by selective laser melting (SLM) in argon or nitrogen.

Tensile orientation ^a & processing ^b condition	ARGON GAS					NITROGEN GAS				
	Hardness		Tensile Properties			Hardness		Tensile Properties		
	HV (GPa) ^d	HRC ^d	Y(0.2%) ^e	UTS ^f	Elong. (%)	HV (GPa) ^d	HRC ^d	Y(0.2%) ^e	UTS ^f	Elong. (%)
Z-axis As Fab.	--	--	--	--	--	--	--	--	--	--
X-axis As Fab.	3.8/3.9	30/33	--	--	--	--	--	0.83	1.12	25
Z-axis HIP/anneal	5.6/5.8	38/39	0.85	1.14	28	5.5/5.6	35/38	0.88	1.14	30
X-axis HIP/anneal	5.5/5.8	33/35	0.89	1.2	28	5.4/5.6	36/38	0.93	1.2	27
X-axis Anneal (4h)	4.5/4.7	39/40	--	--	--	--	--	--	--	--
Nominal ^c Wrought (annealed)	--	24	0.83	1.1	31	--	--	--	--	--
Nominal ^c wrought (aged)	--	45	1.4	1.6	16	--	--	--	--	--

^a Tensile orientation refers to build convention shown in Fig. 3(b). Z-axis refers to cylinders built parallel to the build direction; X-axis refers to cylinders built with axis perpendicular to the build (or beam) direction.

^b Processing conditions: As-fabricated (As-Fab.); fabricated cylinders stress relief annealed at 982°C for 0.5h in vacuum and HIPed at 1163°C for 4h in argon at 0.1 GPa pressure (HIP + anneal); fabricated cylinders annealed in argon at 1160°C for 4h. (Anneal (4h)).

^c Nominal wrought Inconel 718 data from Special Metals Corp. (www.specialmetals.com).

^d Vickers microindentation hardness (HV) and Rockwell C-scale hardness (HRC) are measured in the horizontal plane/vertical plane normal to or parallel to the build direction (Fig. 3(b)).

^e 0.2% engineering offset yield strength in GPa. Data is average of 4 tests.

^f UTS (ultimate tensile strength) in GPa. Data is average of 4 tests

Chapter 4: Inconel 625 Fabricated by Selective Laser and Electron Beam Melting

This chapter's content is available in the following journal article:

Amato, K.N., Murr, L.E., Hernandez, J., Martinez, E., Gaytan, S.M., Shindo, P.W., and Collins, S. Journal of Materials Science Research 2012; 1(2).

In the present study we compared the precipitation and columnar grain development in alloy 625 fabricated by EBM and SLM, along with associated microstructures and corresponding mechanical behavior: tensile and hardness properties. Microstructures, particularly precipitation features developed during HIPing of the EBM and SLM-fabricated alloy 625 were also examined along with the resulting mechanical properties. Light optical microscopy (LOM), scanning and transmission electron microscopy (SEM and TEM) and X-ray diffraction (XRD) were used to characterize the associated and comparative microstructures and microstructural architectures represented by columnar precipitate arrays.

4.1 Fabrication Process Comparison: EBM vs. SLM

A schematic view of the electron beam melting (EBM) system is shown in Figure 4.1(a). Cylinders fabricated for the research presented herein were manufactured using an Arcam A2 EBM system from Arcam AB (Sweden) and an EOS M270 SLM system described in Chapter 3. Since 2005, these systems have been commercially available. Both systems feed powder onto a bed from cassettes in a compacted layer via raking or rolling. These layers, several particles thick, are scanned and selectively melted by an electron or laser beam (as shown in Figure 4.1(a) and 3.2, respectively). Figure 4.1(b) shows the microdendritic structure and variance in particle size of the Inconel 625 powder that is rapidly solidified in an inert environment such as argon or nitrogen. The distribution of particle sizes and near-spherical shape increases the efficiency in flow and layer packing as well as a more uniform melt. Table 4.1 compares the elemental analyses for the EBM and SLM powders and representative fabricated

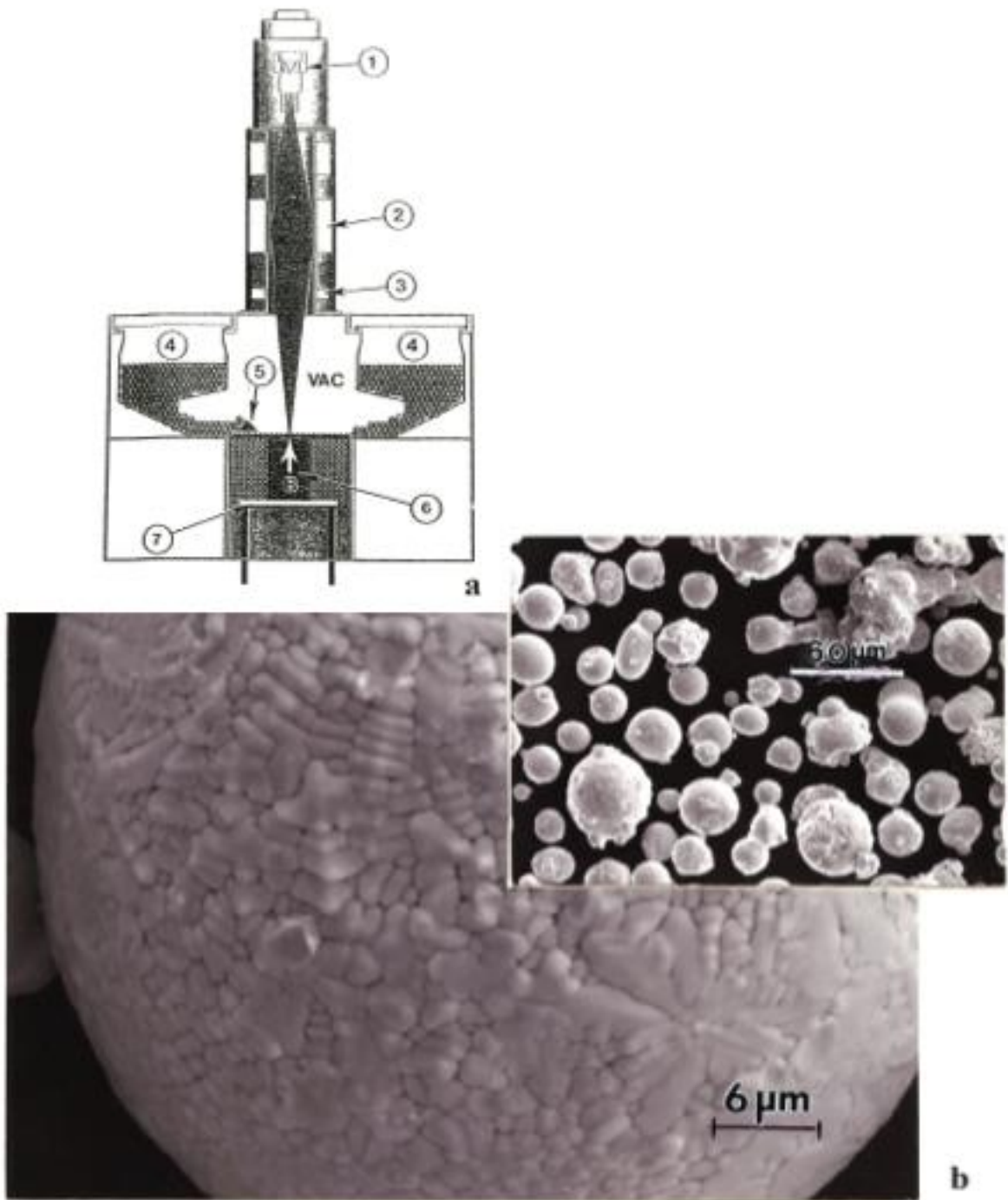


Figure 4.1 (a) EBM system schematic: Electron gun (1), Beam focus lens (2), Beam scan coils (3), Powder cassettes (4), Powder layer rake (5), Building component (6), build platform (7). (b), SLM powder microstructure and low magnification insert. (a) is adapted from Murr et al. (2012a)

components. The average powder sizes were measured to be 22 μ m and 20 μ m for the EBM and SLM powder, respectively.

In the EBM system (Figure 4.1(a)), an electron beam is generated in an electron gun (1) where it is focused through an electromagnetic lens system (2) after being accelerated by a 60 kV potential. The beam, directed by an embedded CAD program (3), selectively melts the powder. Unlike in the SLM, which maintains a constant low temperature, the powder bed is preheated to 0.8 T_m (T_m is the melting temperature) with a high beam current (~30mA) and multiple passes of the beam at a scan rate of $\sim 10^4$ mm/s. The scan rate is reduced to $\sim 10^2$ mm/s and the current is reduced to ~5 to 10 mA for the final melt scan, which produces melt pools with a size determined by the beam diameter and scan spacing. After the build table (7) has been preheated, powder is gravity fed onto it from cassettes (4) and raked (5) in

Table 4.1. Chemical Composition for Alloy 625 EBM and SLM Precursor Powders and Fabricated Components

Material Component	Element (wt. pct.)									
	Ni	Cr	Fe	Mo	Nb	C	Mn	Si	Al	Ti
Nominal Standard	61	22	3.2	9.0	3.5	0.02	0.1	0.1	0.2	0.3
EBM Precursor powder mass analysis	65.7	21.3	0.4	9.3	3.7	0.004	-	-	-	0.002
EBM Precursor powder EDS analysis	59.1	18.8	-	7.6	3.0	-	-	-	-	-
EBM as-fabricated Z-cylinder EDS analysis	61.1	19.2	-	8.8	4.7	-	-	-	-	-
SLM Precursor powder mass analysis	64.8	21.7	<0.1	8.9	3.5	<0.01	0.47	0.39	0.05	0.08
SLM as-fabricated X, Y cylinder EDS analysis	64.2	21.2	-	9.4	5.2	-	-	-	-	-

an even layer. The build table moves downward after each successive layer of the component (6) has been melted. The build direction is indicated by the arrow B in Fig. 4.1(a), which is in the z-direction in relation to the x-y scan direction of the powder layers. The EBM system operates in under a vacuum of $<10^{-4}$ Torr. To enhance heat conduction and component cooling, the pressure is increased to $\sim 10^{-2}$ Torr by a helium gas bleed near the build area, where SLM which achieves this in an inert environment.

4.2 Experimental Methods

4.2.1 Microstructural Characterization

Microstructures of Inconel 625 powders and cylinders fabricated by EBM and SLM were examined using LOM and XRD before SEM and TEM analyses. The LOM, SEM, XRD, and TEM analysis were as mentioned in Chapter 3. To bring out annealing twin structures in LOM, samples were additionally electro-etched with 5% hydrochloric acid for 1-10 s.

4.2.2 Mechanical Testing

Microhardness and macrohardness measurements were made using the same process as mentioned in Chapter 3.

Tensile specimens were machined from the as-fabricated and as-fabricated and HIPed EBM cylinders as well as the SLM as-fabricated and HIPed cylinders. Tensile specimens were machined from the as-fabricated cylinders HIPed at 0.1 GPa for 4 h at 1120°C ($\sim 0.84T_m$, where T_m was 1335°C). Tensile tests were conducted at a strain rate of $\sim 10^{-3} \text{ s}^{-1}$ at room temperature (22°C). The fabricated and HIPed specimens were also tested at 538°C (1000°F). Fracture surfaces were also examined in the SEM.

4.3 Results and Discussion

4.3.1 Microstructural Characterization

EBM As-Fabricated Components

Figure 4.2 shows a 3D LOM composition typical for columnar Ni_3Nb (bct: $a = 0.362 \text{ nm}$, $c = 0.741 \text{ nm}$; space group: $I4/mmm$) γ'' -precipitate platelets oriented in the build direction (arrow in Figure 4.2), and corresponding to roughly $2 \mu\text{m}$ melt pool dimensions characteristic of the EBM beam scan geometry. Figure 4.3 shows a TEM magnified view of the Ni_3Nb (γ'') precipitate platelets, which are coincident with the NiCr γ -matrix (fcc, $a = 0.359 \text{ nm}$; space group: $Fm\bar{3}m$) $\{111\}$ planes as discussed in detail by Murr et al. (2011). Note in Figure 4.3 that the γ'' platelets are associated with columnar, low-angle boundaries, which help to define the columnar arrays. Dense dislocation substructures are also observed to be associated with the precipitates. It might also be noted that the selected-area electron diffraction (SAED) pattern for the TEM image area shown in Fig. 4.3 for γ'' precipitate columns in an

EBM fabricated component was indexed with a [220] (or [110]) zone axis, and the corresponding crystallographic directions are noted in Fig. 4.3.

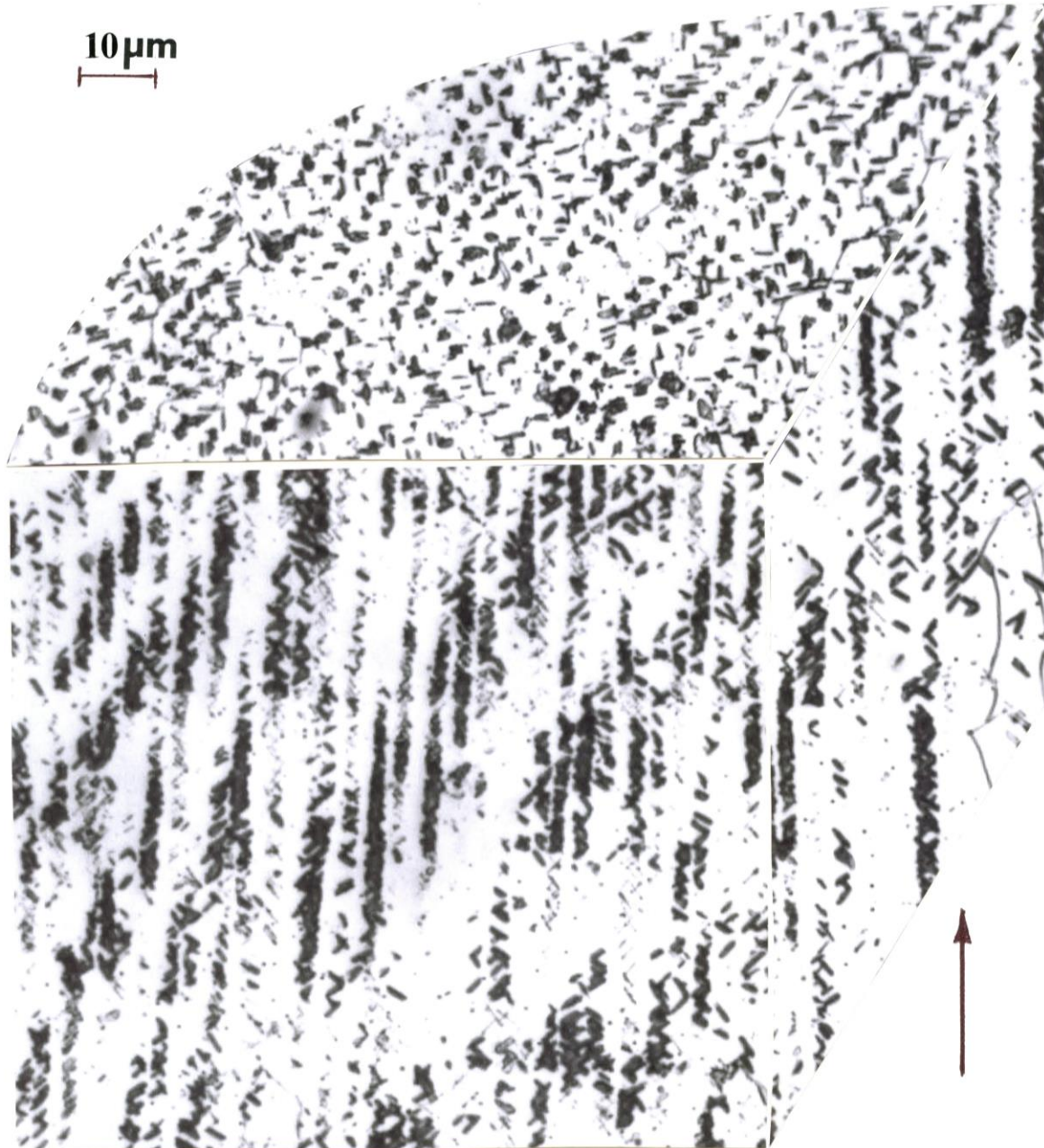


Figure 4.2. 3D LOM image composition for EBM fabricated component section showing columnar, precipitate platelets. Arrow at lower right shows the build direction.

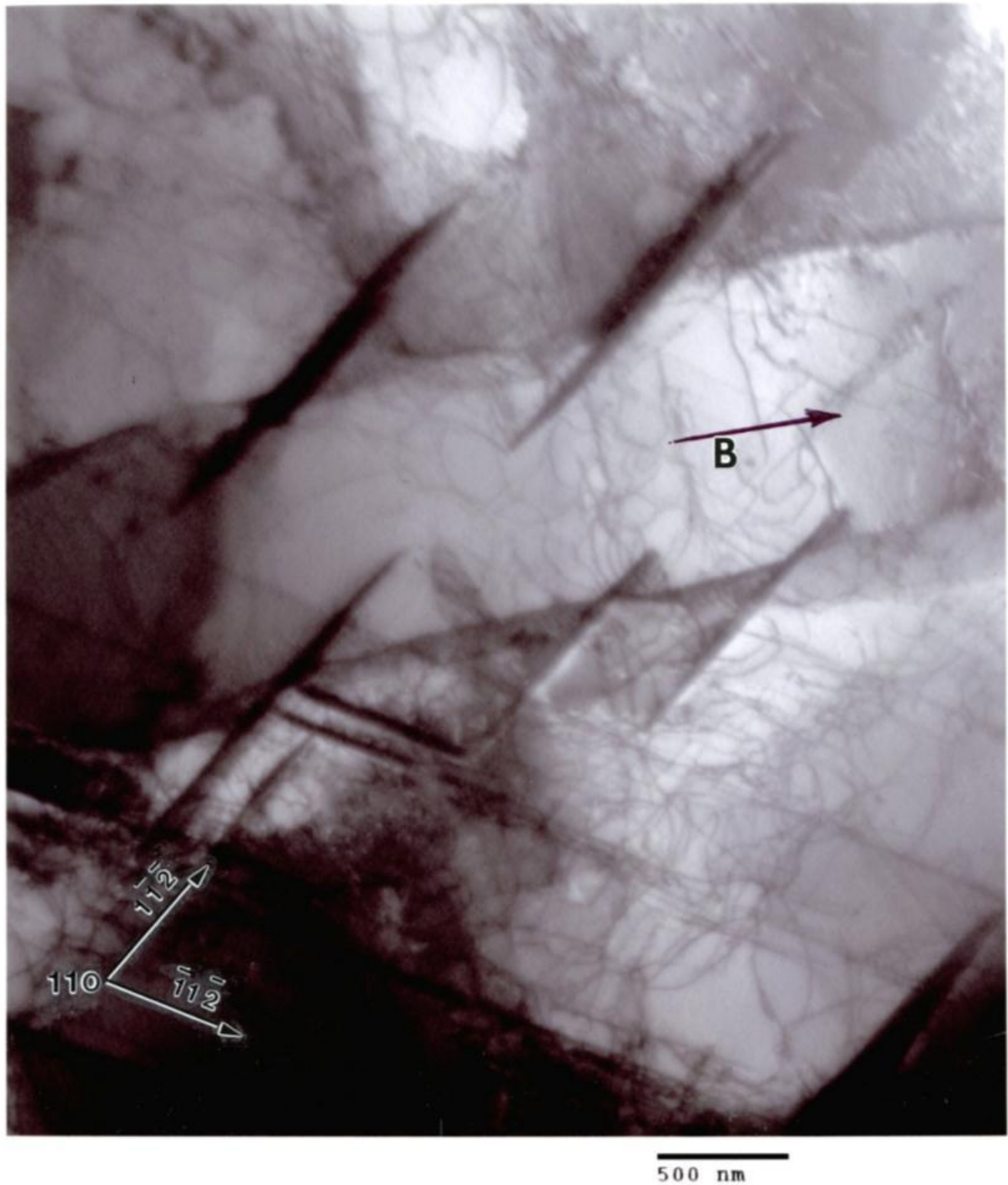


Figure 4.3. TEM vertical plane section view (parallel to the build direction (B) showing γ'' precipitate platelets coincident with the NiCr fcc matrix $\{111\}$ planes. The grain surface orientation is (110). The build direction marked B is coincident with the arrow in Fig. 4.2.

The columnar precipitate arrays shown in Figures 4.2 and 4.3 are also oriented (textured) in the [200]

direction parallel to the build

direction. These columnar arrays are

also coincident with the as-fabricated

cylinder (Z) axis as evident from the

XRD spectrum shown for the

horizontal section perpendicular to

the build direction (B in Figures 4.2

and 4.3) in Figure 4.4. The vertical

section XRD spectra also show the

[220] texture in the plane parallel to

the build direction in Figure 4.2, and

is coincident with the [110] zone

corresponding to Figure 4.3. The

Ni₃Nb (bct) precipitate platelet

spectra coincide with fcc (γ)-NiCr

peaks noted in Figure 4.4. Columnar

grains, primarily oriented in the

[200] direction shown in the XRD

spectra in Figure 4.4, are roughly 10

μm in diameter as shown lightly

etched in the 3D LOM composition

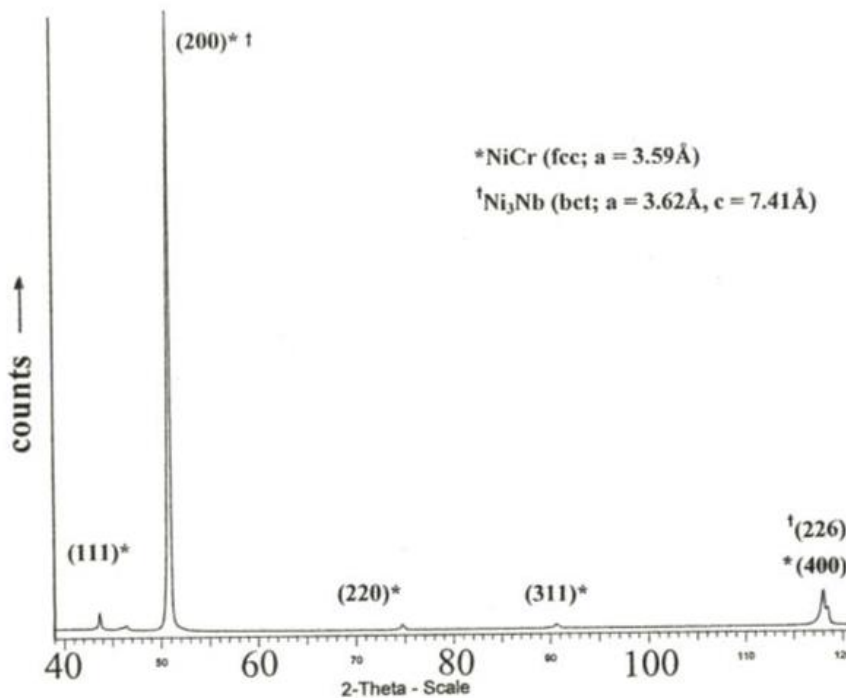
in Figure 4.2.

SLM As-Fabricated Components

Figure 4.5 shows a 3D LOM

image composition typical for the as-

HORIZONTAL SECTION



VERTICAL SECTION

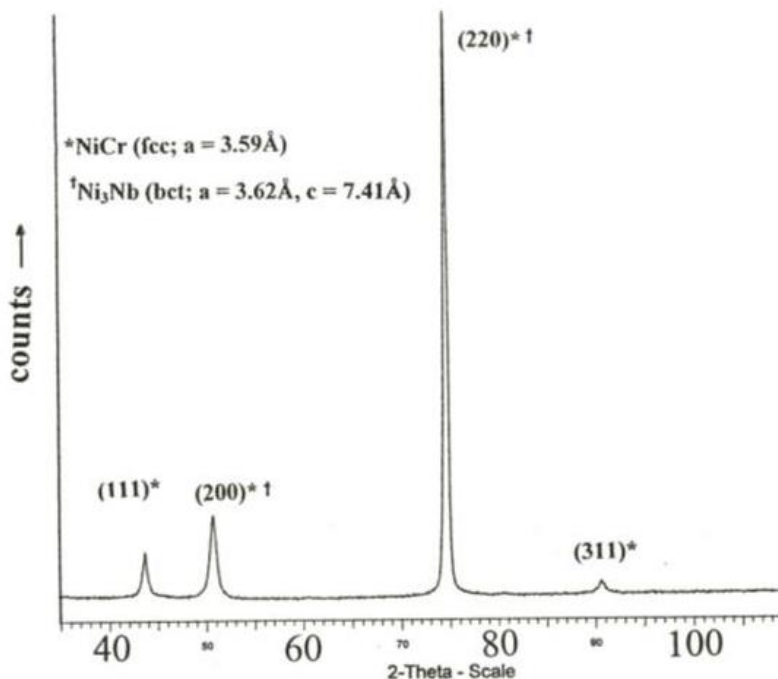


Figure 4.4. XRD spectra corresponding to the horizontal and vertical reference planes in Figure 4.2 (EBM).

fabricated, Z-axis oriented cylinders built in the direction parallel to the cylinder axis. In contrast to Figure 4.2 at the same magnification, there are several very notable differences. First is the presence of melt (layer) banding characteristic of laser melt scanning (Thijs et al., 2010). The dark contrast, which distinguishes these bands, arises by enhanced precipitation of γ'' (bct-Ni₃Nb). Second, and in the context of γ'' precipitation, it is readily apparent in Figure 4.5 that the columnar precipitate arrays are roughly half or less the γ'' precipitate column spacing for EBM components shown in Figure 4.2. The actual γ'' column array widths are also roughly 3 times those for SLM-fabricated (Z-axis) components as shown in Figure 4.5.

The precipitates in the columnar arrays of Figure 4.5 are also not large platelets or discs similar to those shown in Figures 4.2 and 4.3. Additionally, (as shown in Figure 4.6 in contrast to the XRD spectra in Figure 4.4) the orientation in the horizontal reference plane normal to the build direction is [200], while for the vertical reference plane parallel to the build direction, the orientation is also [200] for SLM (Figure 4.6) and [220] for EBM fabrication (Figure 4.4). Note that, as in the XRD spectra for EBM-fabricated (Z-axis) components in Figure 4.4, the γ'' (bct-Ni₃Nb) precipitate phase spectra coincide with select fcc-NiCr spectral peaks.

In contrast to Z-axis built components, cylindrical components were also built in the X-Y plane perpendicular to the build direction. These X-Y (or XY)-axis components exhibited similar macrostructure-microstructure features to those shown in Figure 4.5 for Z-axis built, SLM components. Figure 4.7 shows a slightly more magnified 3D LOM image composition than Figure 4.5 showing irregular, columnar precipitate arrays along with oriented, low-angle grain boundaries (6B) and characteristic SLM melt-scan banding. Again, it is especially notable to recognize the difference between the γ'' precipitate columns for EBM in Figure 4.2 and the γ'' precipitate columns for SLM in Figure 4.7. The XRD spectra for the horizontal and vertical reference planes in Figure 4.7 (indicated by H and V, respectively) are also shown in Figure 4.8, which, as noted previously for Figure 4.6, shows different, preferred orientations or textures than those exhibited for EBM-fabricated components shown in Figure 4.4. The prominence of [111] and [200] are particularly notable for SLM component texture (Fig. 4.8).

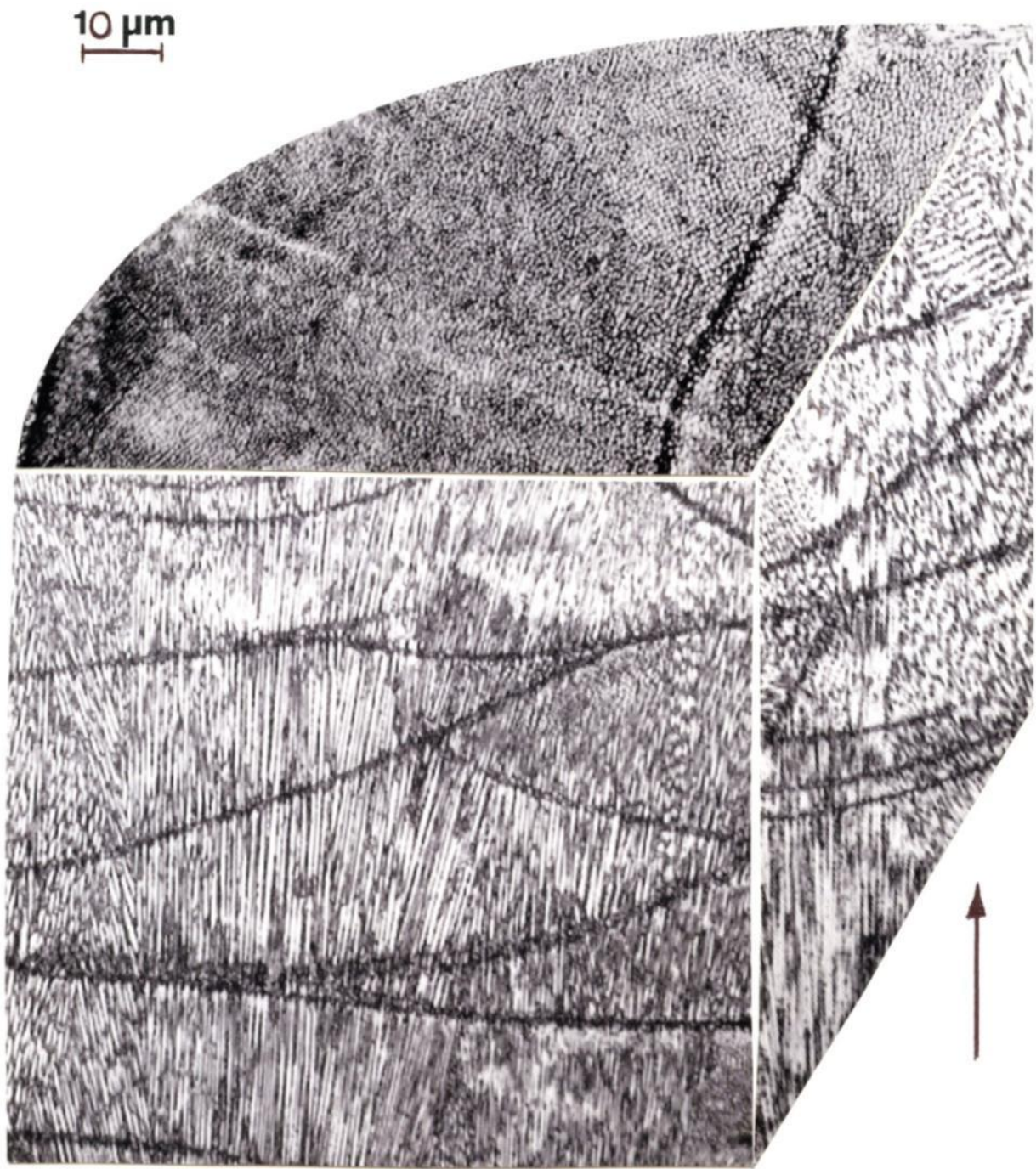


Figure 4.5. 3D LOM composite section for an SLM (Z-axis) fabricated component. Note build direction represented by the arrow is parallel to the Z-axis orientation.

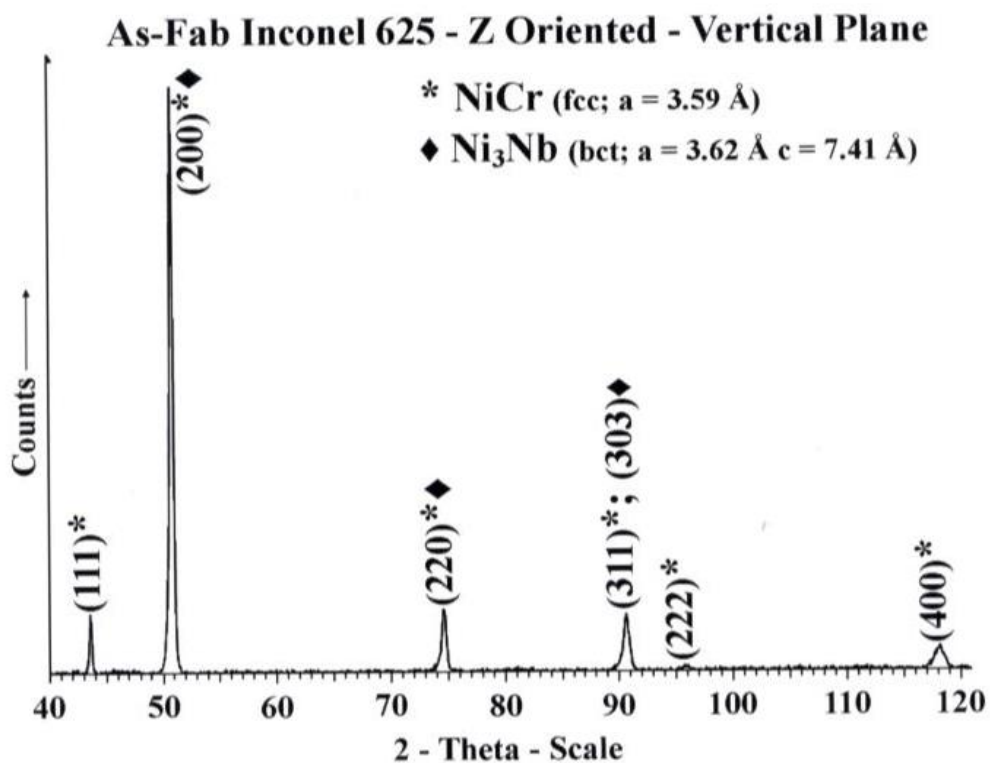
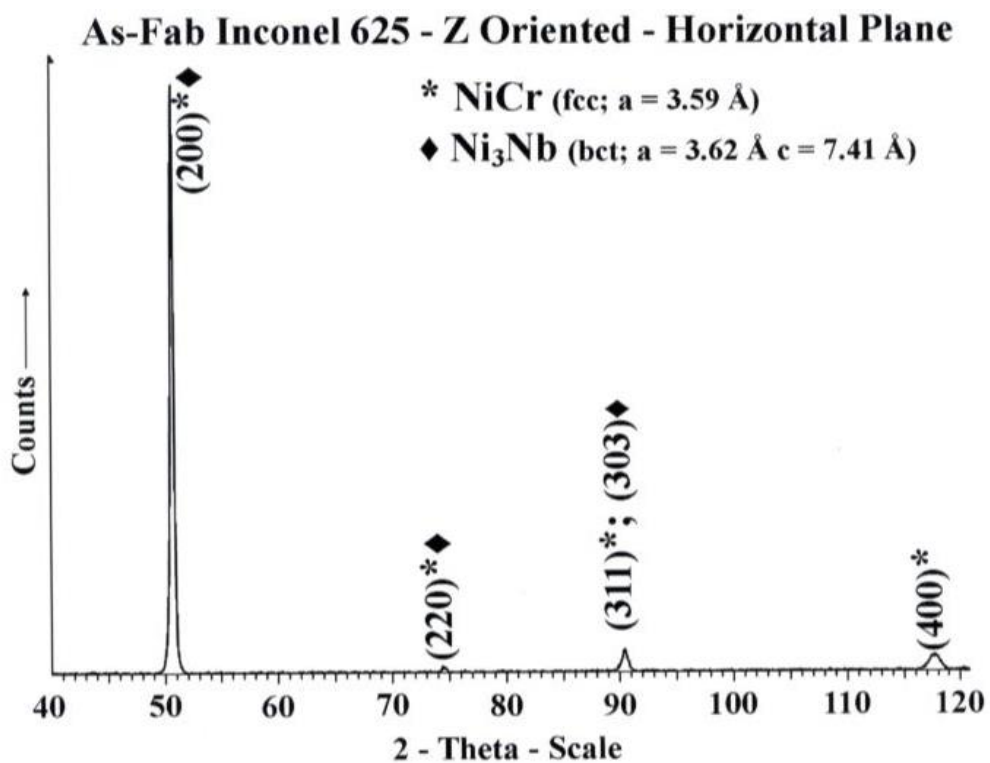


Figure 4.6. XRD spectrum corresponding to the vertical and horizontal reference planes represented in Figure 4.5.

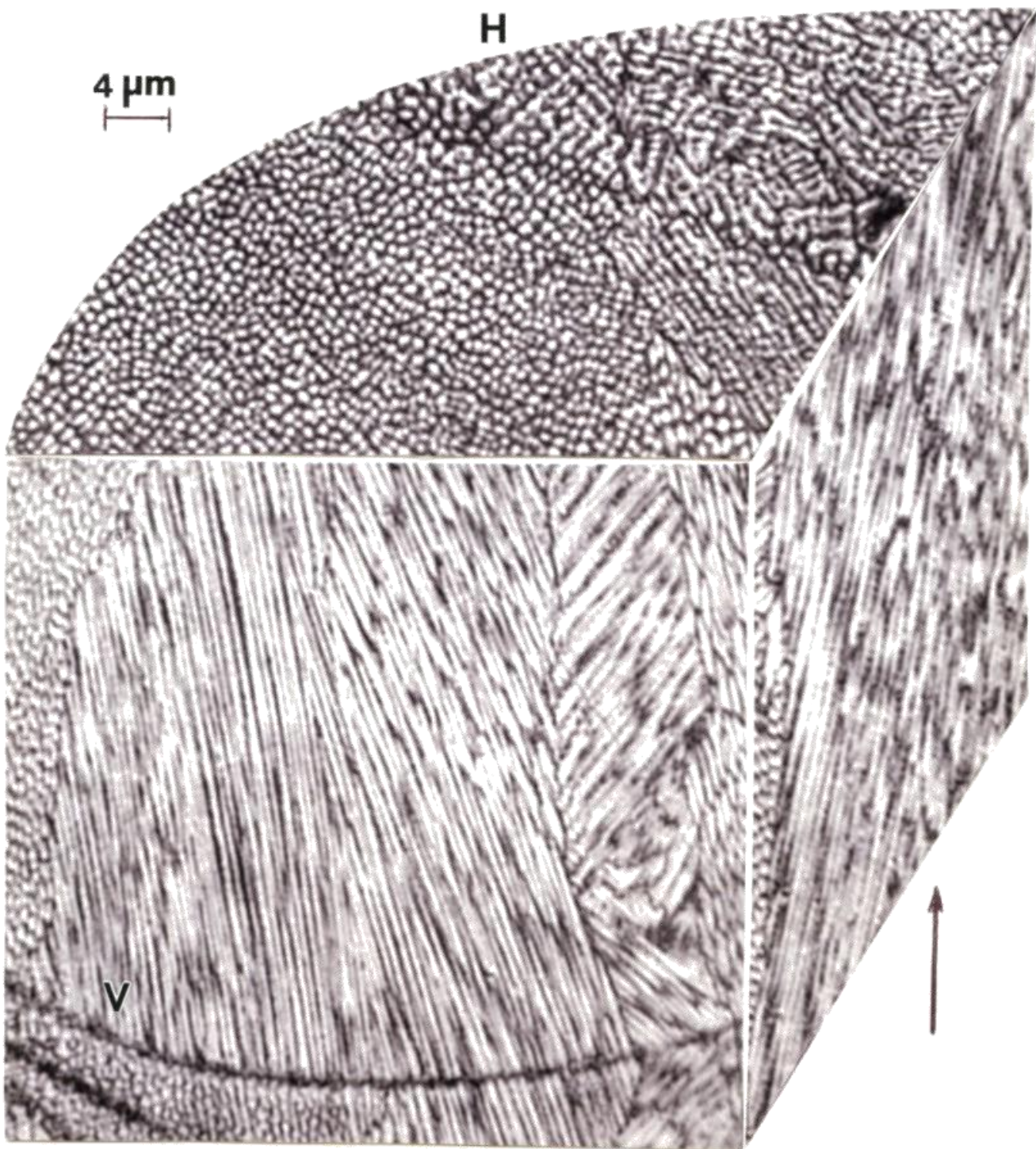


Figure 4.7 3D LOM composite section for an SLM (X, Y-axis) fabricated component. Note build direction represented by the arrow at lower right which is perpendicular to the X, Y-axis, of the cylindrical component.

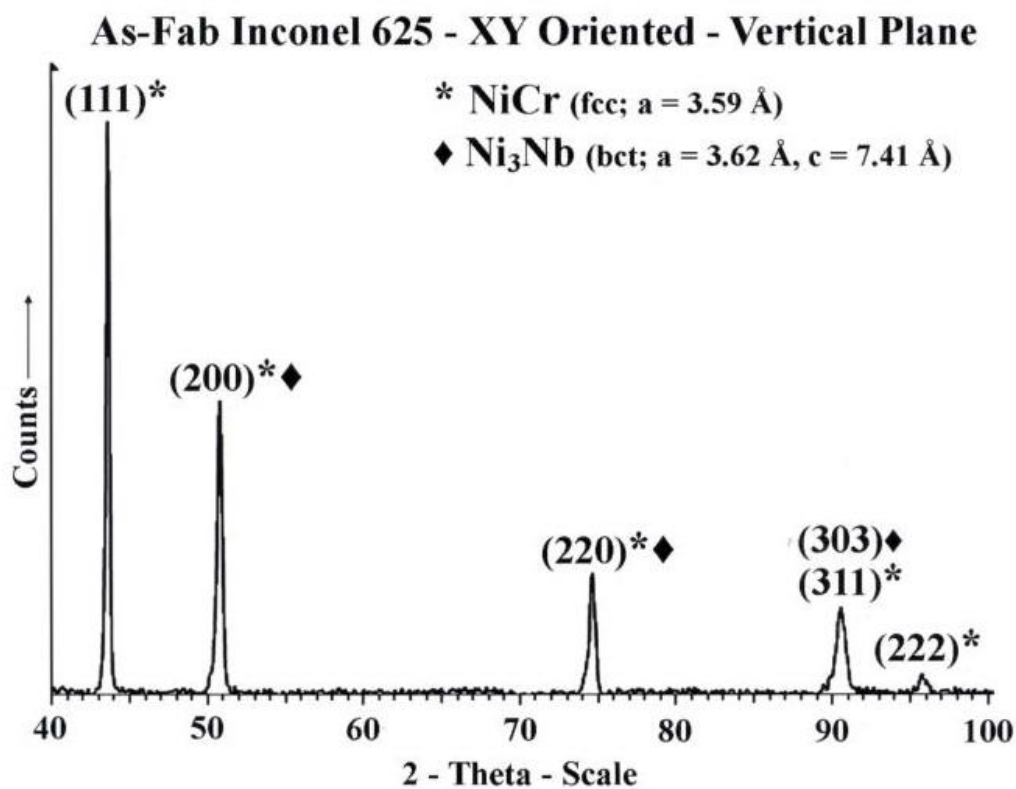
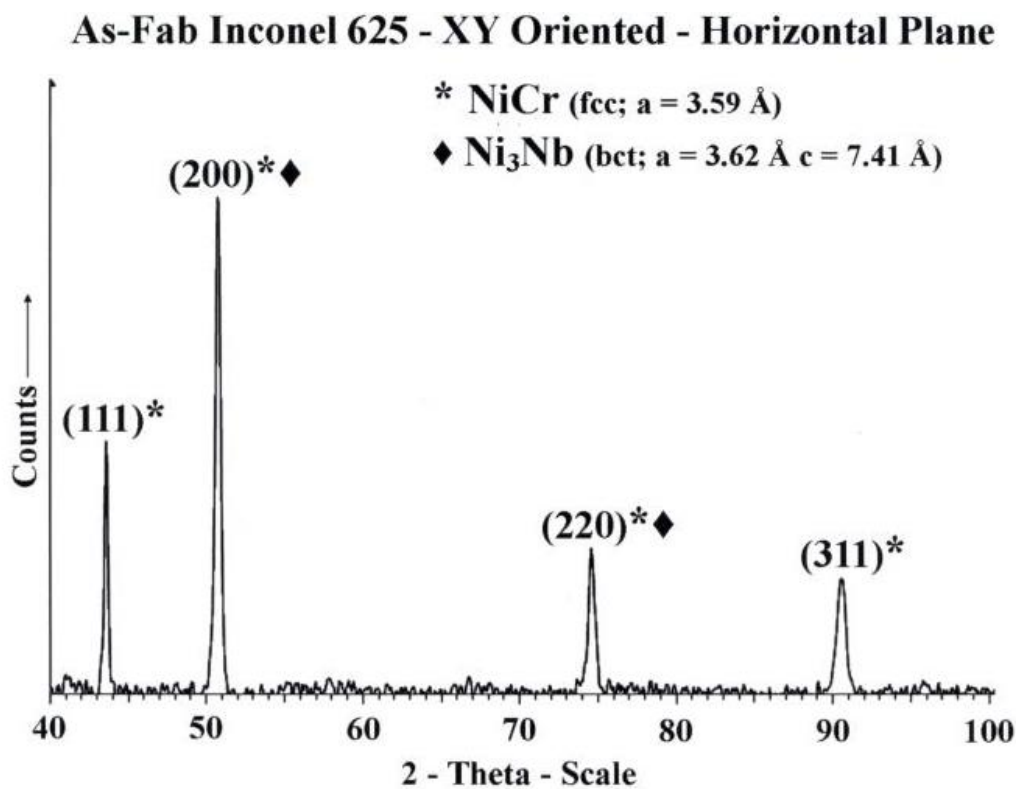


Figure 4.8. XRD spectrum corresponding to the vertical and horizontal reference planes represented in Figure 4.7.

Figure 4.9(a) and (b) illustrate the significant difference in γ'' precipitate morphology and size for the SLM fabricated cylinders (XY-axis) in contrast to those shown in Figure 4.3 for EBM fabrication. Comparison of Figures 4.3 and 4.9(b) also illustrate the smaller precipitate column spacing for SLM versus EBM-fabricated components. Similar, dense dislocation arrays are also associated with the very fine (nano-size) γ'' precipitate columnar arrays as shown in Figure 4.9(b). Examination of Figures 4.9(a) and (b) in contrast to Figure 4.7 suggests that the precipitate columns form as cylindrical arrays at the edges or transition regions of the melt pools, rather than the center of the melt pools. The (112) orientation for the horizontal reference plane view in Figure 4.9(a) SAED pattern insert also demonstrates that the dislocation-precipitate arrays are dominated by the melt pool geometry rather than texture, which is dominated by [200] as shown in Figure 4.8.

Figure 4.10 shows a magnified TEM image representing the precipitate reference at P in Figure 4.9(b). To the right in Figure 4.10 the fine γ'' precipitates and heavy dislocation substructure composing the columnar arrays prominently depicted in Figure 4.7. The precipitates at P in Figure 4.10 appear to be a small cluster of three γ'' precipitate particles with diameters ranging from 10 to 20 nm. Somewhat larger precipitates are shown in the column to the right in Figure 4.10, and there is evidence for precipitation on dislocations as well.

Figures 4.11 and 4.12 show a sequence of analytical components, which examine the composition of the fine γ'' precipitates. In Figure 4.11, a vertical reference section of a XY-oriented cylinder is examined in the TEM. The small section of a precipitate column shown bounded by the dashed-line box is magnified in Figure 4.12(a). Arrows delineate a short section of precipitates in Figure 4.12(a) and (b), where Figure 4.12(b) represents a Nb-X-ray map using the Nb window for the EDS (elemental) spectra shown in Figure 4.12(c). Because of the very small size of the globular, nano-precipitates (γ''), there is no discernable Ni signal associated with the 100 nm long strip between the arrows in Figures 4.12(a) and (b).

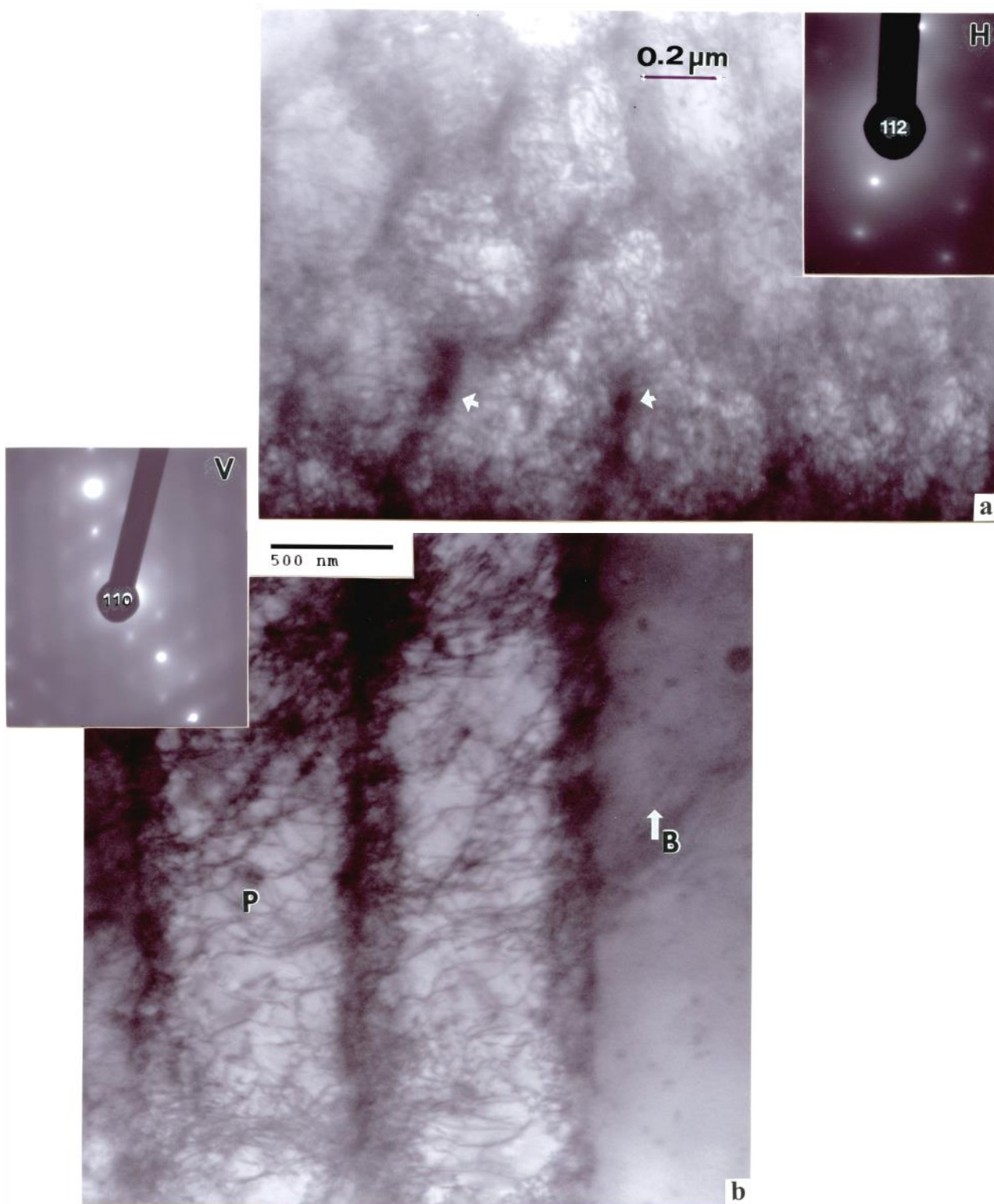


Figure 4.9. TEM bright-field images in the (a) horizontal (H) and (b) vertical (V) reference planes for Figure 4.7. P in (b) designates a precipitate (γ'') cluster. The build direction is denoted by white arrow (B) at right in (b) SAED pattern inserts show (112) orientation in the horizontal (H) plane (a), and (110) orientation in the vertical (V) plane (b). Note arrows in (a) show precipitate clusters within dislocation cell-like arrays.

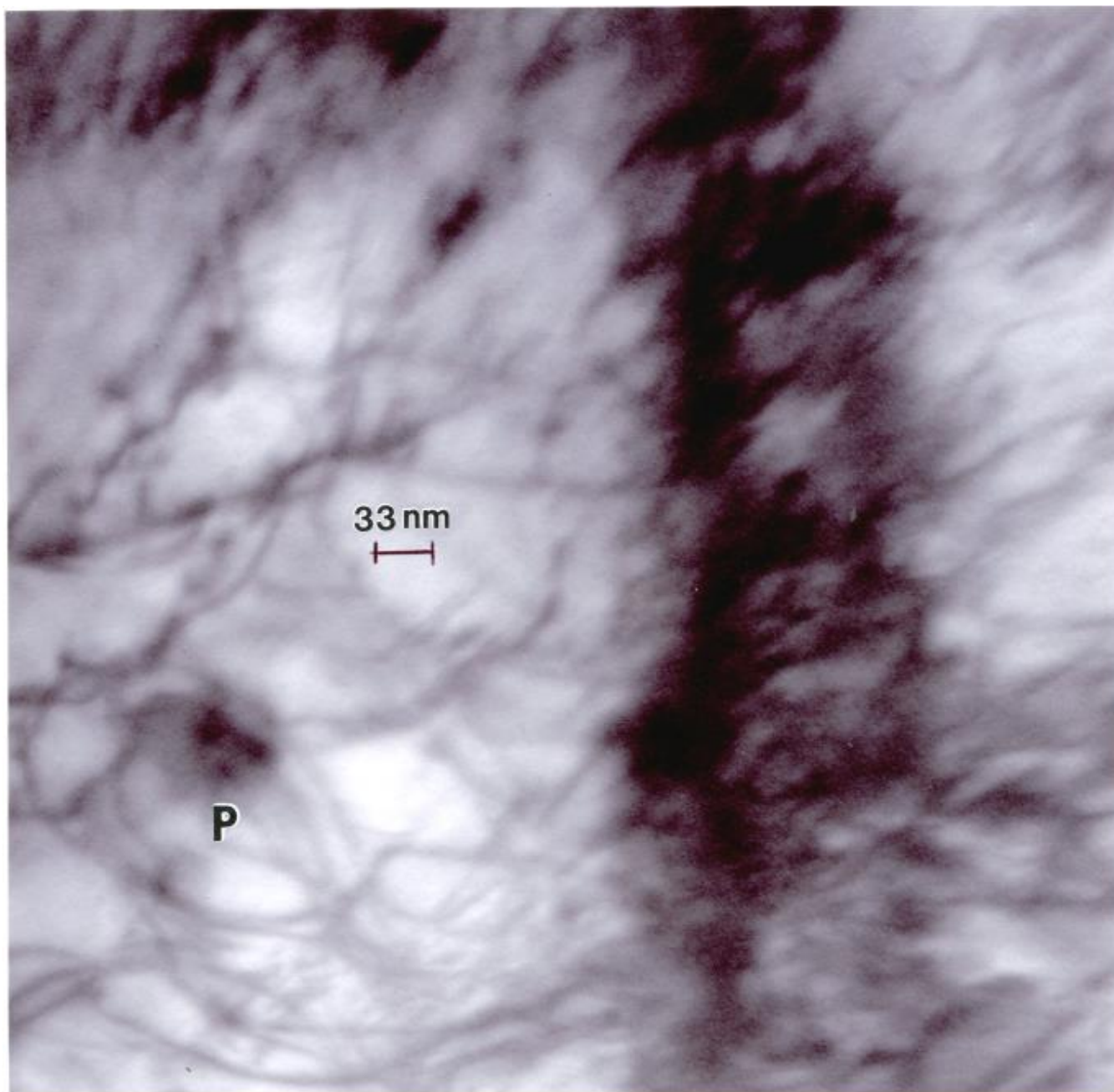


Figure 4.10. TEM magnified view in Figure 4.9, P designates precipitate cluster in Figure 4.9. Column of precipitate clusters and dense dislocations is shown at right.

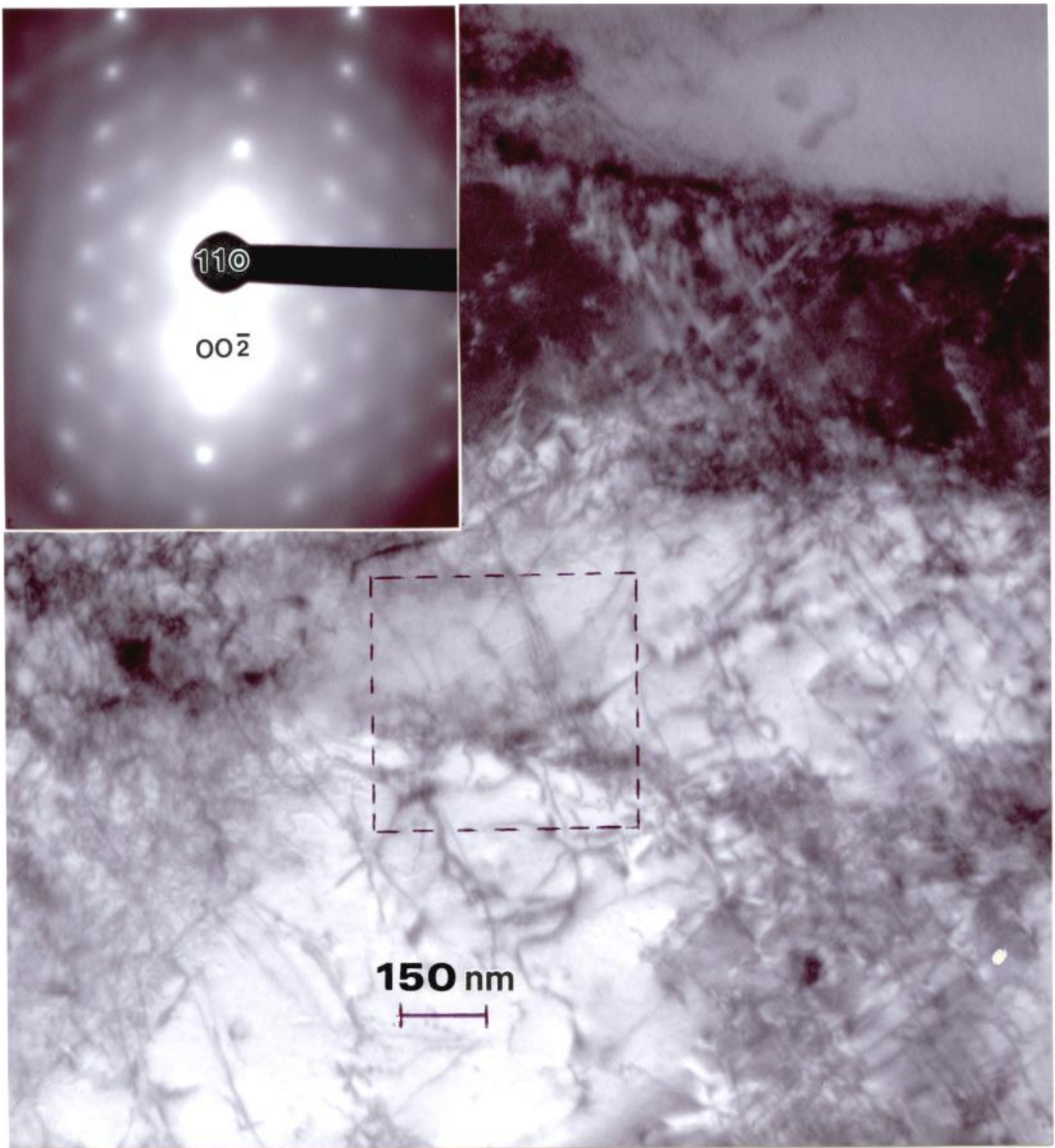


Figure 4.11. TEM image showing γ'' precipitation arrays. Reference section of array is enclosed in the dotted box. The SAED pattern insert shows the (110) grain surface orientation. The operating reflection for diffraction contrast is shown to be $g = [00\bar{2}]$.

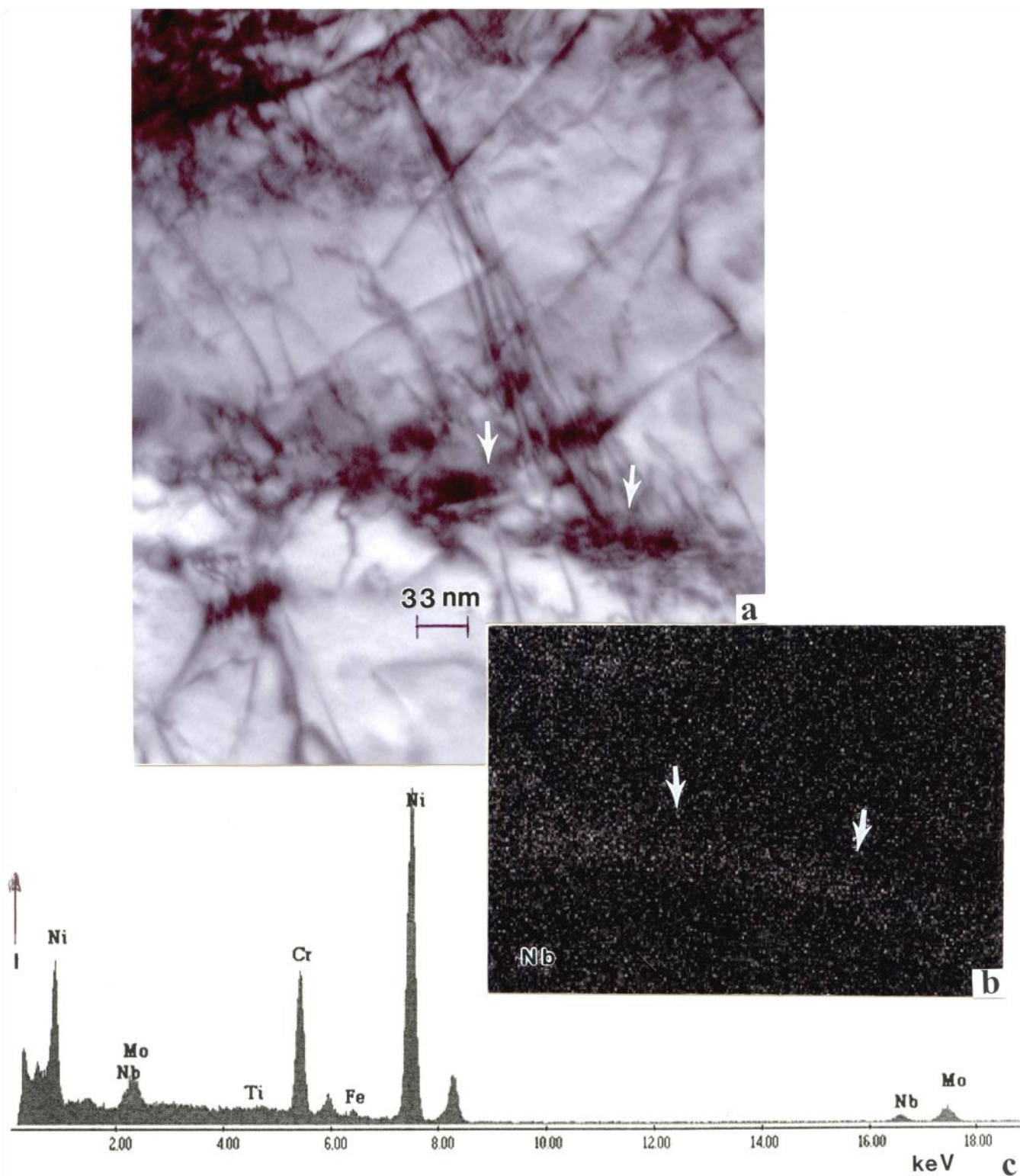


Figure 4.12. Magnified TEM image for Fig. 4.11 showing precipitate clusters within the dotted reference box. Arrows in (a) show precipitate clusters (aggregates) which exhibit Nb-rich features shown in the corresponding Nb-X-ray map in (b). (c) shows the TEM-EDS spectrum for (a).

The SAED pattern inserts in both Figures 4.9 and 4.11 for corresponding TEM images in an SLM-fabricated component are, as in Figure 4.3, a [110] zone axis. Again, comparing these common crystallographic features in Figures 4.3 and 4.9 point up the notable difference in γ'' precipitate morphology and size discussed above for EBM versus SLM fabrication. This is due in large part because of the notable difference between the cooling or solidification phenomena, where SLM beam scan produces considerably more rapid cooling (Murr et al., 2009; 2012a) which appears to restrict precipitate nucleation and growth. This is also exaggerated by building X-Y-oriented cylinders, which cool much differently from the Z-axis oriented cylinders. Beam scan and especially melt scan variances are especially notable on comparing Figures 4.2 and 4.5. Figure 4.13 compares LOM and SEM images showing the vertical reference plane melt-scan-related banding for SLM-fabricated components. The γ'' precipitates, which delineate these bands, are illustrated more prominently in the SEM image of Figure 4.13(b).

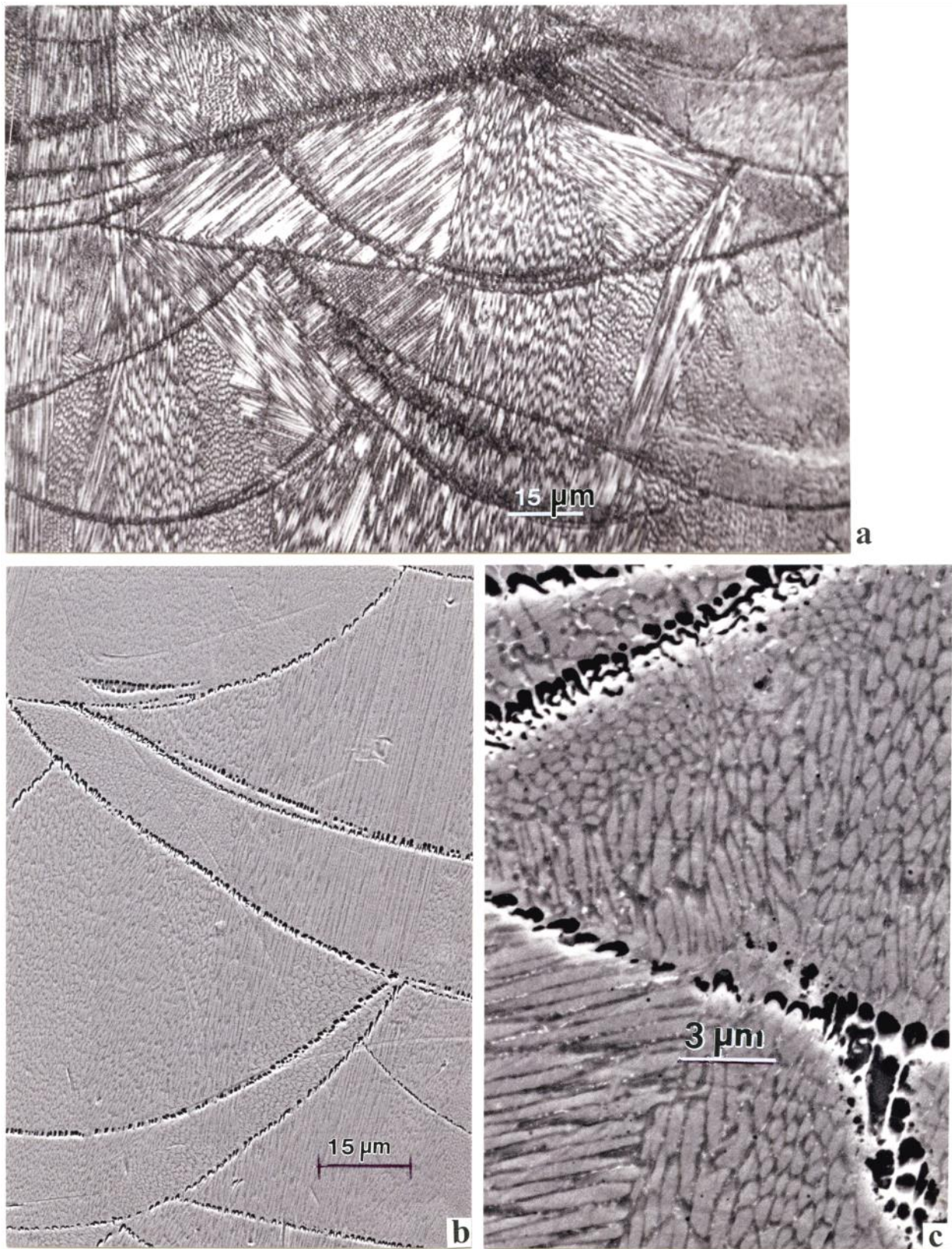


Figure 4.13. SLM-laser melt-scan banding. (a) LOM image in vertical reference plane for X,Y-axis cylindrical component (b) SEM image showing γ'' precipitate/second-phase formation within the melt bands. (c) Magnified SEM image showing melt-band precipitates.

EBM Fabricated and HIPed Components

Figure 4.14 shows a 3D LOM image composition for the EBM-fabricated and HIP components showing characteristic equiaxed grains and annealing twins representing the low-stacking-fault free energy fcc NiCr matrix (Murr, 1975). The average grain size was observed to be $\sim 50\text{ }\mu\text{m}$, including the annealing twins. The matrix contains a dense distribution of precipitates along with continuous precipitate arrays in many grain boundaries presumed to be high energy (Murr, 1975).

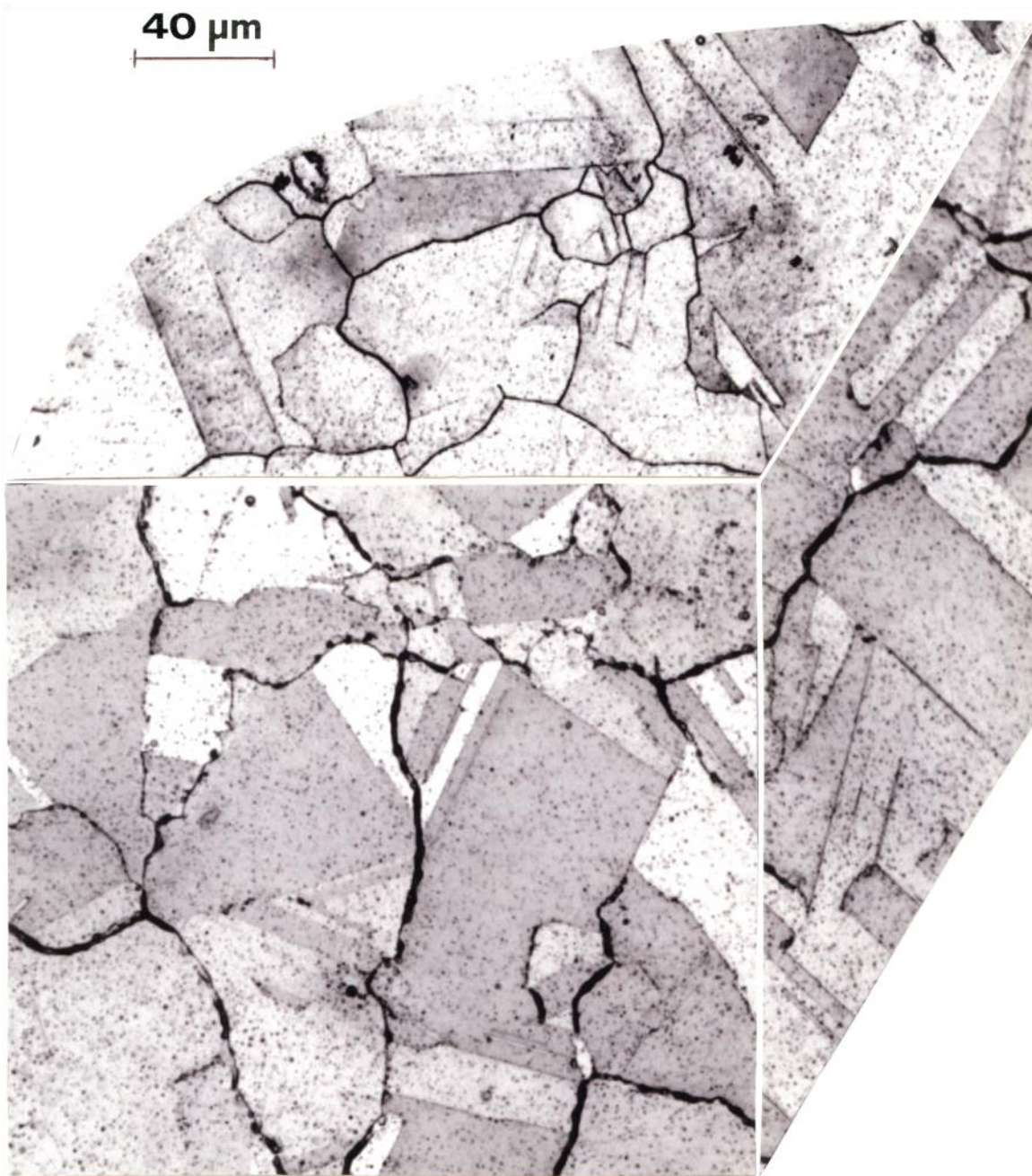


Figure 4.14. EBM fabricated and HIP (Z-axis) component 3D LOM composition showing equiaxed, fcc (NiCr) grain structure and associated precipitation.

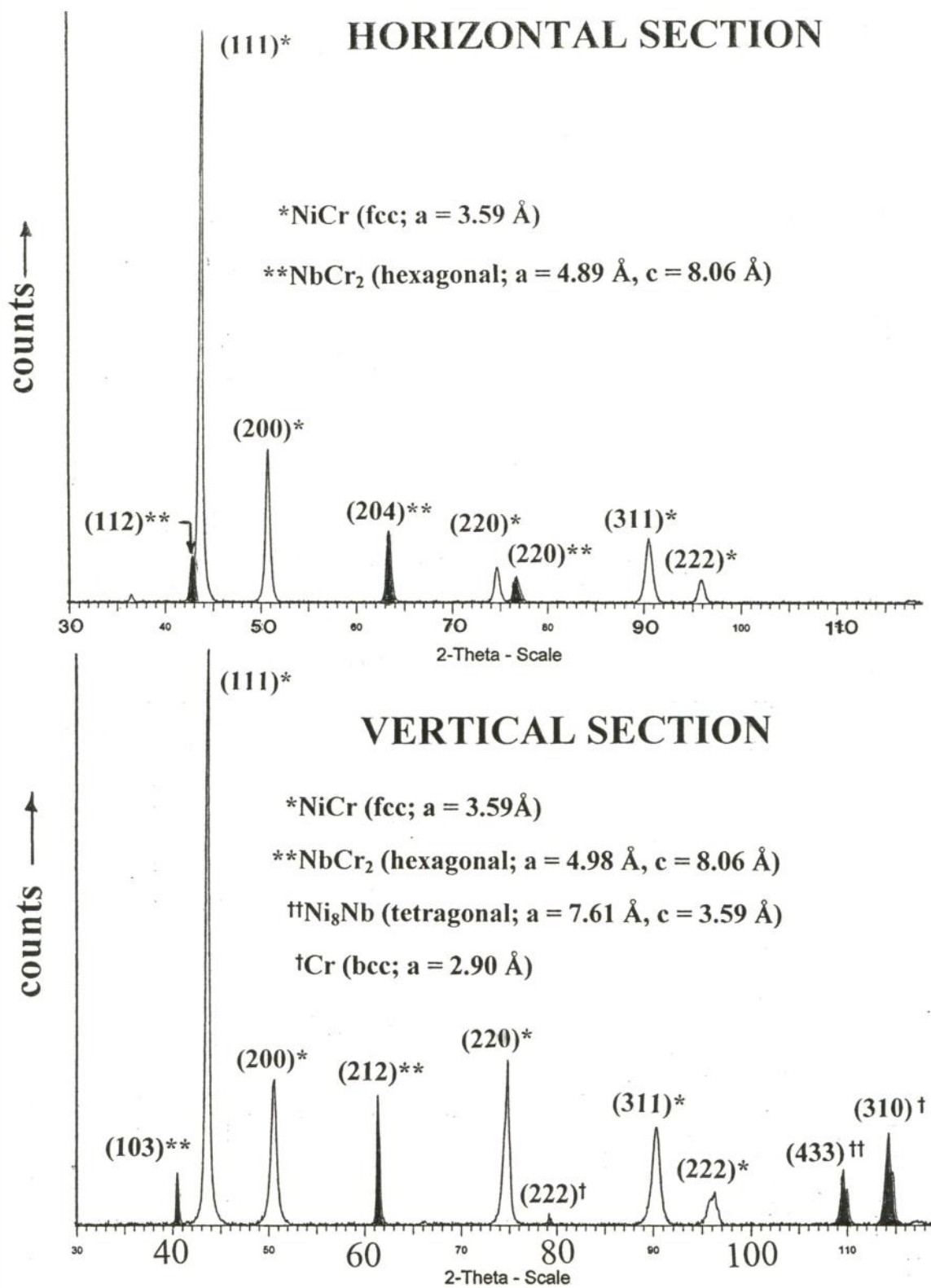


Figure 4.15. XRD spectra corresponding to the horizontal and vertical reference planes in Fig. 4.14. Prominent precipitation peaks are dark shaded.

Figure 4.15 shows the corresponding XRD spectra for Fig. 4.14, where dark (shaded) peaks represent the precipitation: NbCr_2 (laves: hexagonal; $a = 0.49 \text{ nm}$, $c = 0.81 \text{ nm}$, space group: $P6_3 \text{ mmc}$), nickel-rich, Ni_8Nb (tetragonal; $a = 0.76 \text{ nm}$, $c = 0.36 \text{ nm}$; space group: $P(0)$); and pure Cr precipitates. These are represented typically in the TEM image in Fig. 4.16, which shows a low-energy annealing twin with no precipitation in the boundaries (Murr et al., 2011). In contrast, Fig. 4.17 shows an analytical sequence showing a Cr inclusion (precipitate) at the edge of an electropolished foil section. The bright-field TEM image in Fig. 4.17(a) is in a (110) grain orientation shown by the SAED pattern in Fig. 4.17(b). Figure 4.17(c) shows the precipitate EDS analysis in contrast to the matrix EDS analysis shown in Fig. 4.17 (f), in contrast to Table 4.1. Figure 4.17(d) and (e) show corresponding Cr and Ni elemental maps utilizing the EDS analysis in Fig. 4.17(c).

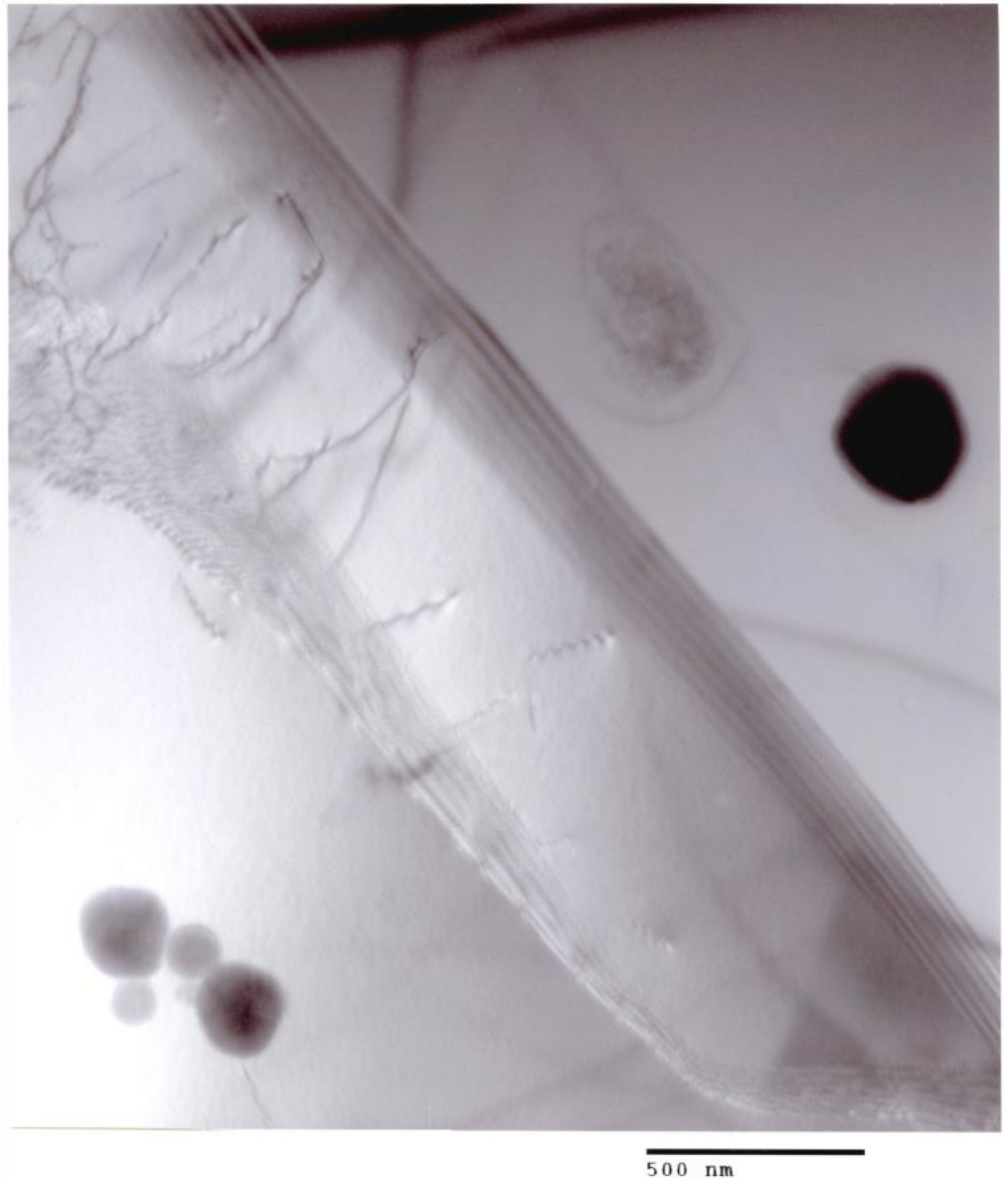


Figure 4.16. TEM bright-field image showing typical intergranular precipitates (NbCr_2) corresponding to Fig. 4.15. Coherent annealing twin is shown in the image center (upper left to lower right).

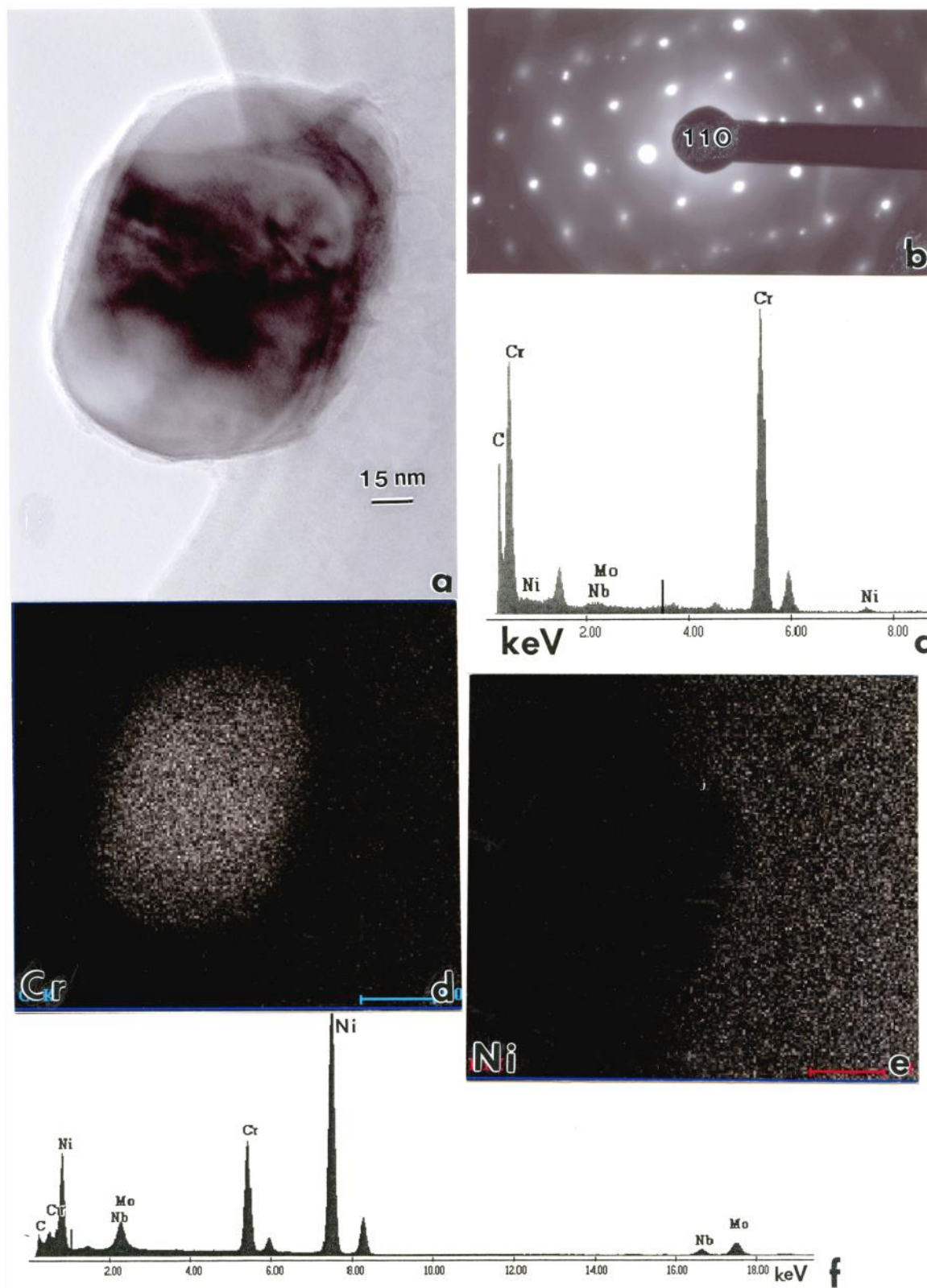


Figure 4.17. Analytical sequence showing Cr precipitate in EBM fabricated and HIP component. (a) TEM image of precipitate at foil edge. (b) SAED pattern showing (110) orientation for supporting NiCr matrix. (c) EDS spectra for precipitate in (a). (d) Cr map using (c). (e) Ni map for (a). (f) EDS spectrum for NiCr matrix.

SLM Fabricated and HIPed Components

Figures 4.18 and 4.19 show 3D LOM image composites for SLM cylindrical components fabricated in the Z-axis direction and XY-axis directions and HIPed, respectively. Although the HIP-annealed microstructures shown in Figs. 4.18 and 4.19 emulate the equiaxed NiCr grain structure containing coherent annealing twins or twin boundaries shown for EBM fabricated-HIP samples shown represented typically in Fig. 4.14, there are notable differences. The most notable difference is the apparently larger intergranular precipitates, with the largest precipitates shown in Fig. 4.18. Precipitation in the grain boundaries occurs in a similar fashion with continuous precipitation or second-phase appearance along some boundaries. There is no precipitation along the low-energy, coherent twin boundaries in either Figs. 4.14, 4.18, or 4.19.

As shown in the XRD spectra for corresponding horizontal and vertical reference planes for EBM-fabricated and HIP components in Fig. 4.15, and in supporting data contained in Figs. 4.16 and 4.17, precipitation involves NbCr_2 (hexagonal; space group: P_{63}/mmc ; $a = 4.98 \text{ \AA}$, $c = 8.06 \text{ \AA}$) laves precipitates, pure (bcc) Cr precipitates, and Ni_8Nb (tetragonal) precipitates (Murr et al., 2011). In contrast, the XRD spectra corresponding to Figs. 4.18 and 4.19 shown in Fig. 4.20 and 4.21, respectively, indicate smaller amounts of NbCr_2 (hexagonal) laves precipitates, MoNb (bcc) precipitates and NiNb (rhombohedral) precipitates. These findings are consistent with the fundamental differences in microstructures developed in EBM versus SLM-fabricated components. The large, intergranular precipitates shown in Fig. 4.18 are MoNb polyhedra having sizes ranging from $0.2 \text{ }\mu\text{m}$ to $\sim 1 \text{ }\mu\text{m}$.



Figure 4.18. SLM fabricated and HIP (Z-axis) component 3D LOM composition showing equiaxed, fcc (NiCr) grain structure and associated precipitation.

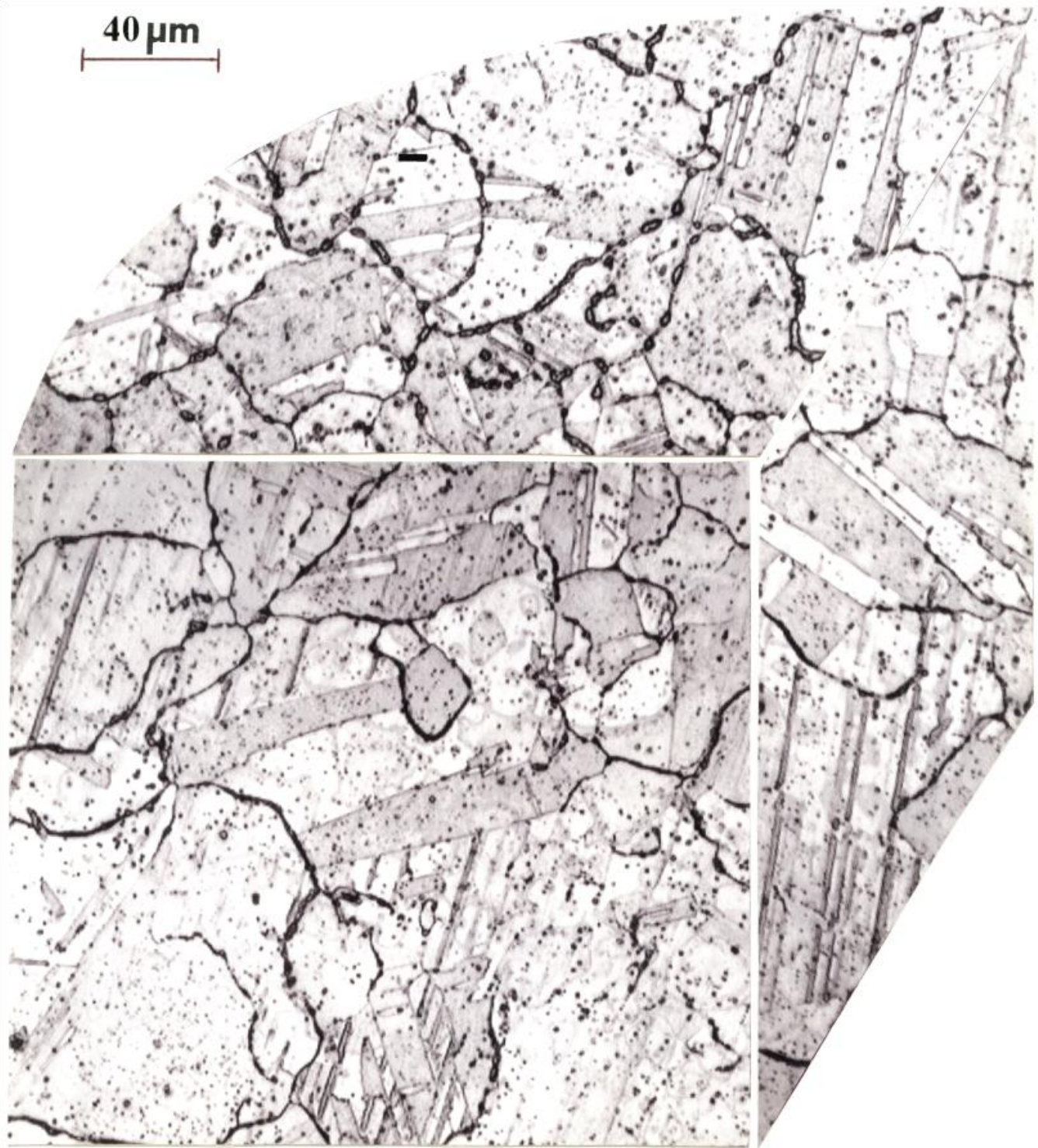


Figure 4.19. SLM fabricated and HIP (X, Y-axis) component 3D LOM composition showing equiaxed, fcc (NiCr) grain structure and associated precipitation.

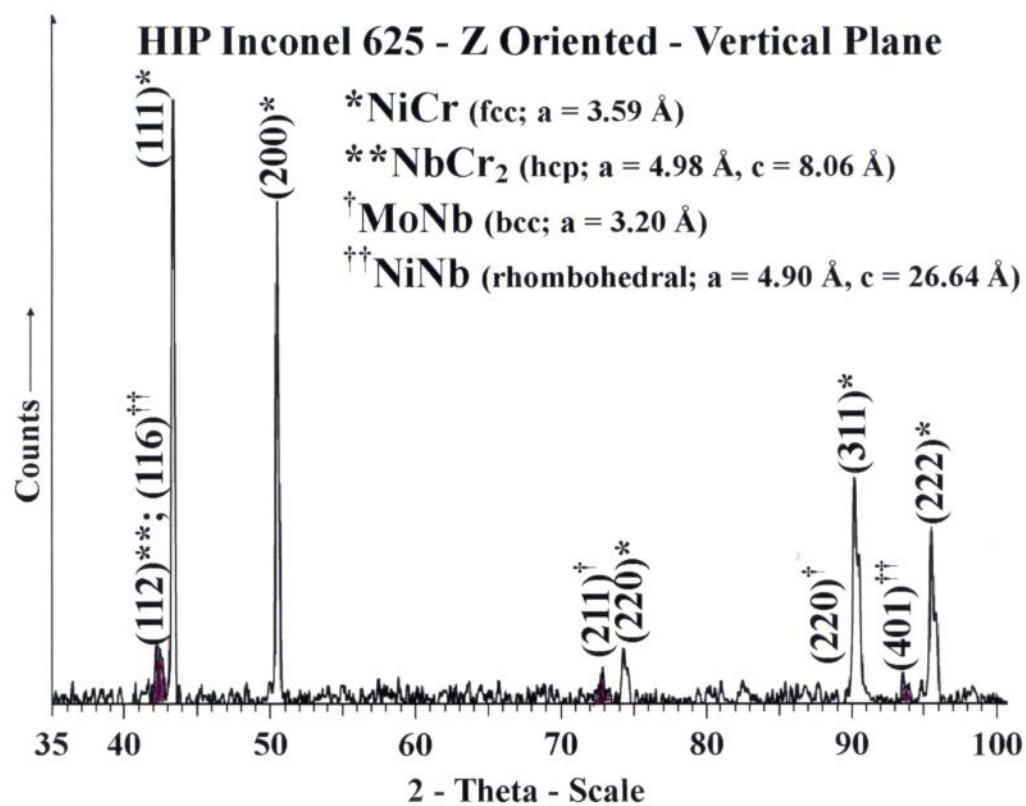
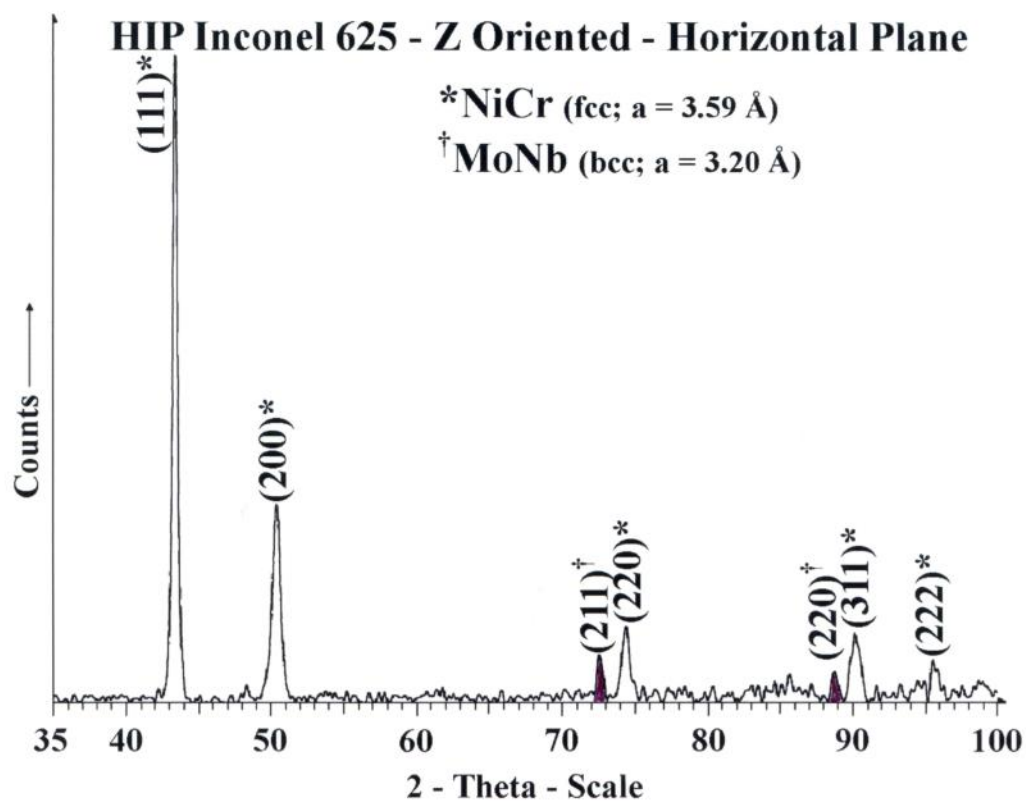


Figure 4.20. XRD spectra corresponding to horizontal and vertical reference planes in Fig. 4.18. Precipitation peaks are dark shaded.

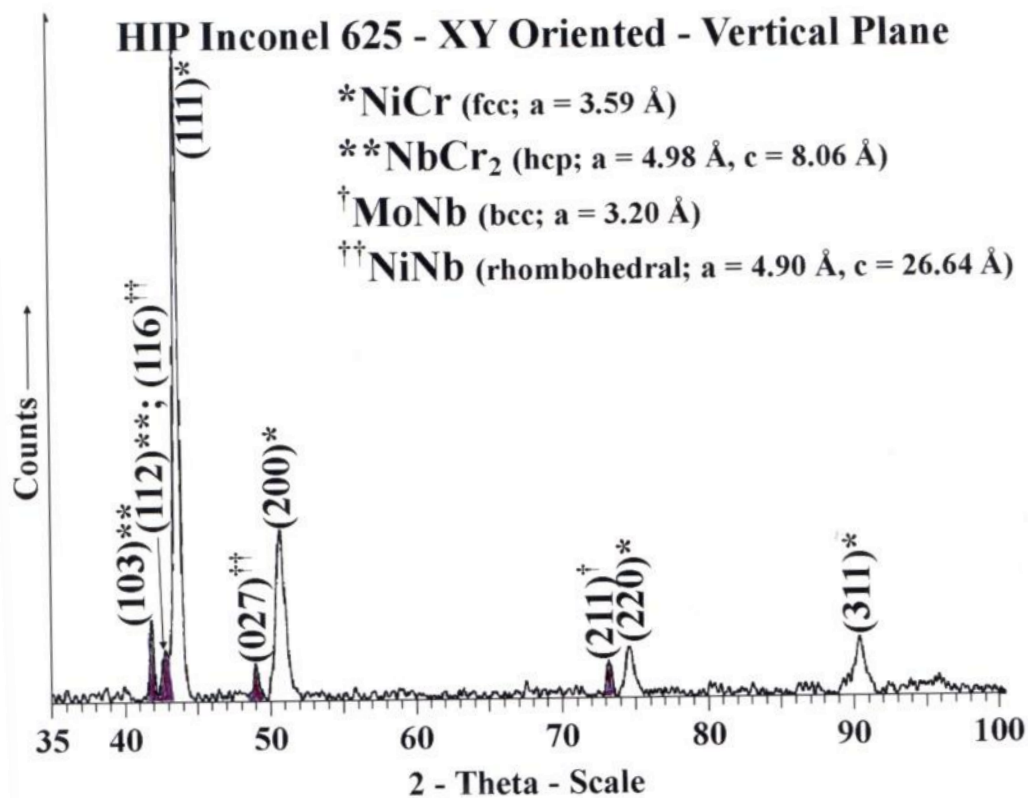
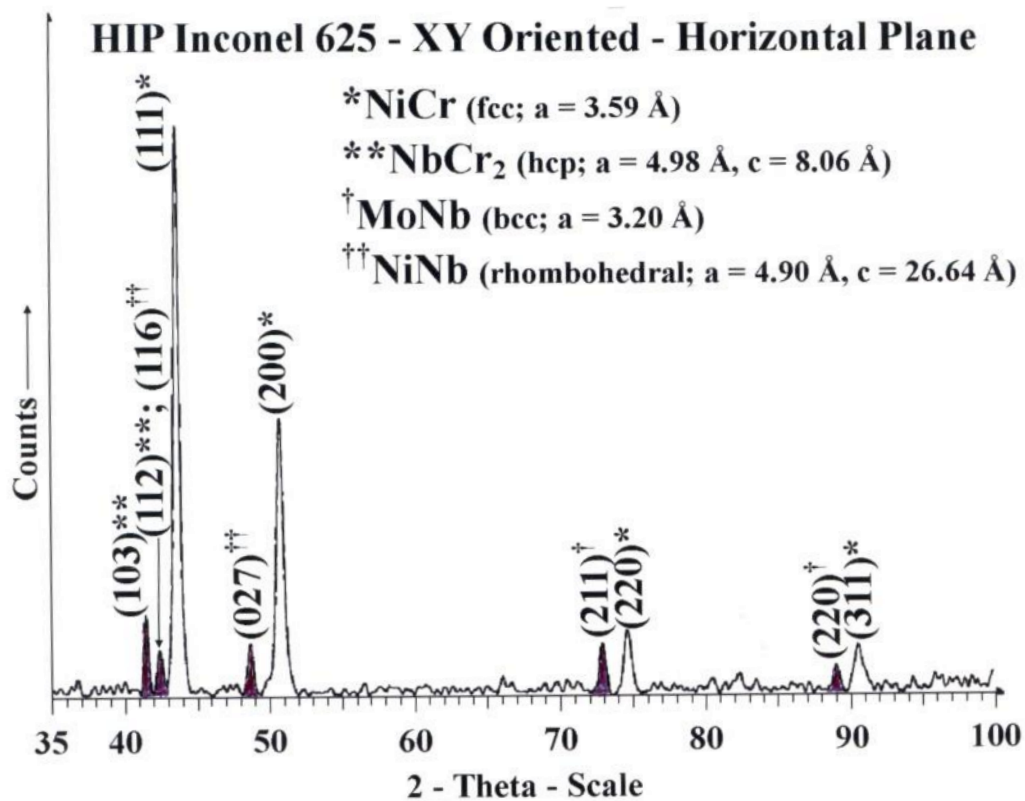


Figure 4.21. XRD spectra corresponding to horizontal and vertical reference planes in Fig. 4.19. Precipitation peaks are dark shaded.

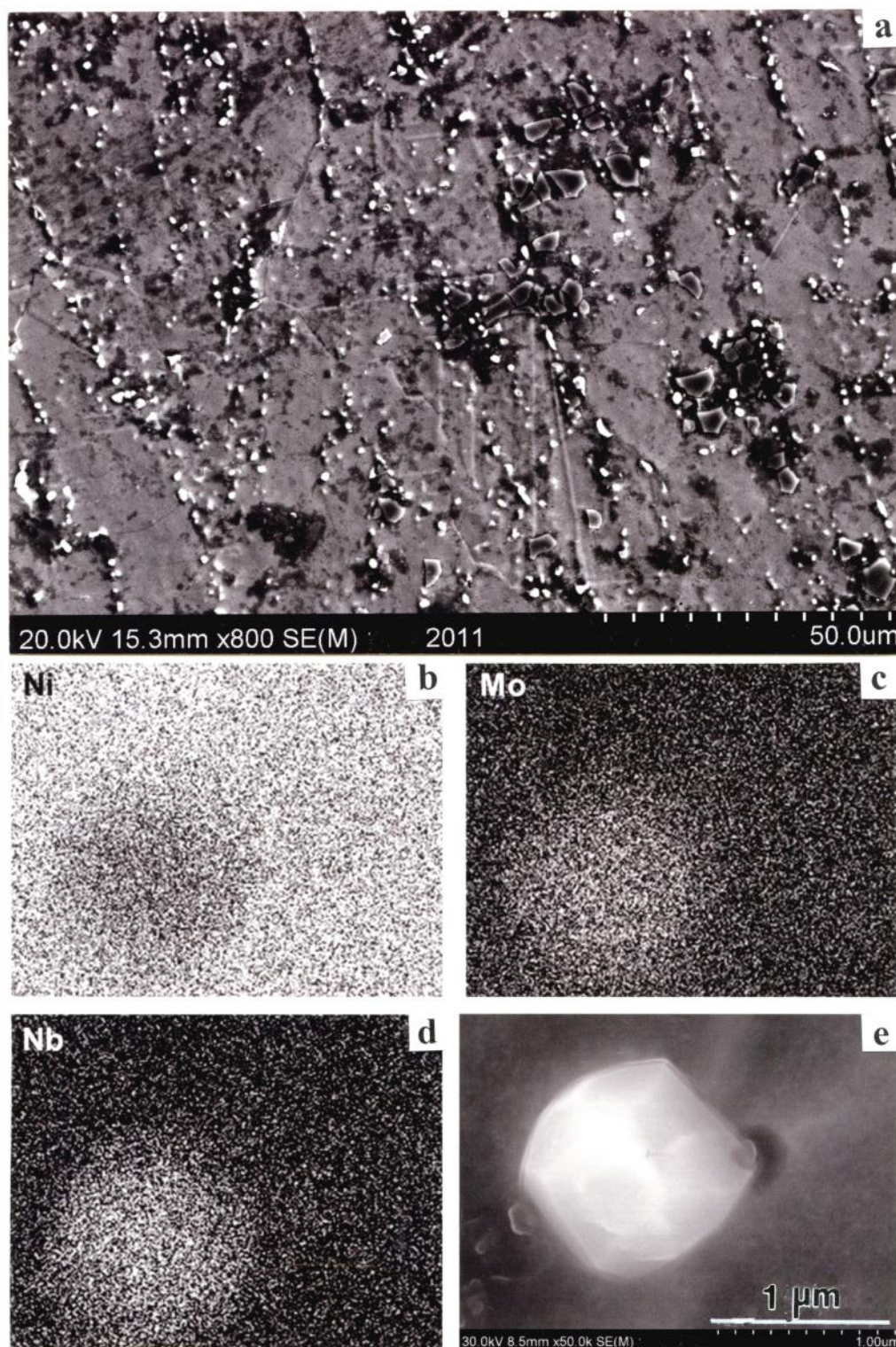


Figure 4.22. SLM (Z-axis) fabricated and HIP component observed in vertical reference plane (Fig. 4.18). (a) SEM image of precipitates. (b) to (d) show corresponding EDS elemental X-ray maps. (e) Precipitate image.

Figures 4.22 and 4.23 illustrate analysis sequences using SEM and EDS in the SEM for SLM – Z-axis fabricated and HIP components. Figures 4.22(e) and 4.23(a) clearly show the faceted, polyhedral MoNb single-crystal precipitates remaining after LOM etch. The elemental spectrum in Fig. 4.23(c) shows, in contrast to the background spectrum shown for comparison in Fig. 4.17(f), for example, the Nb and Mo peak prominence, while the corresponding elemental X-ray maps in Fig. 4.23(b) and (d) confirm the precipitate species shown in the XRD spectra for Fig. 4.20.

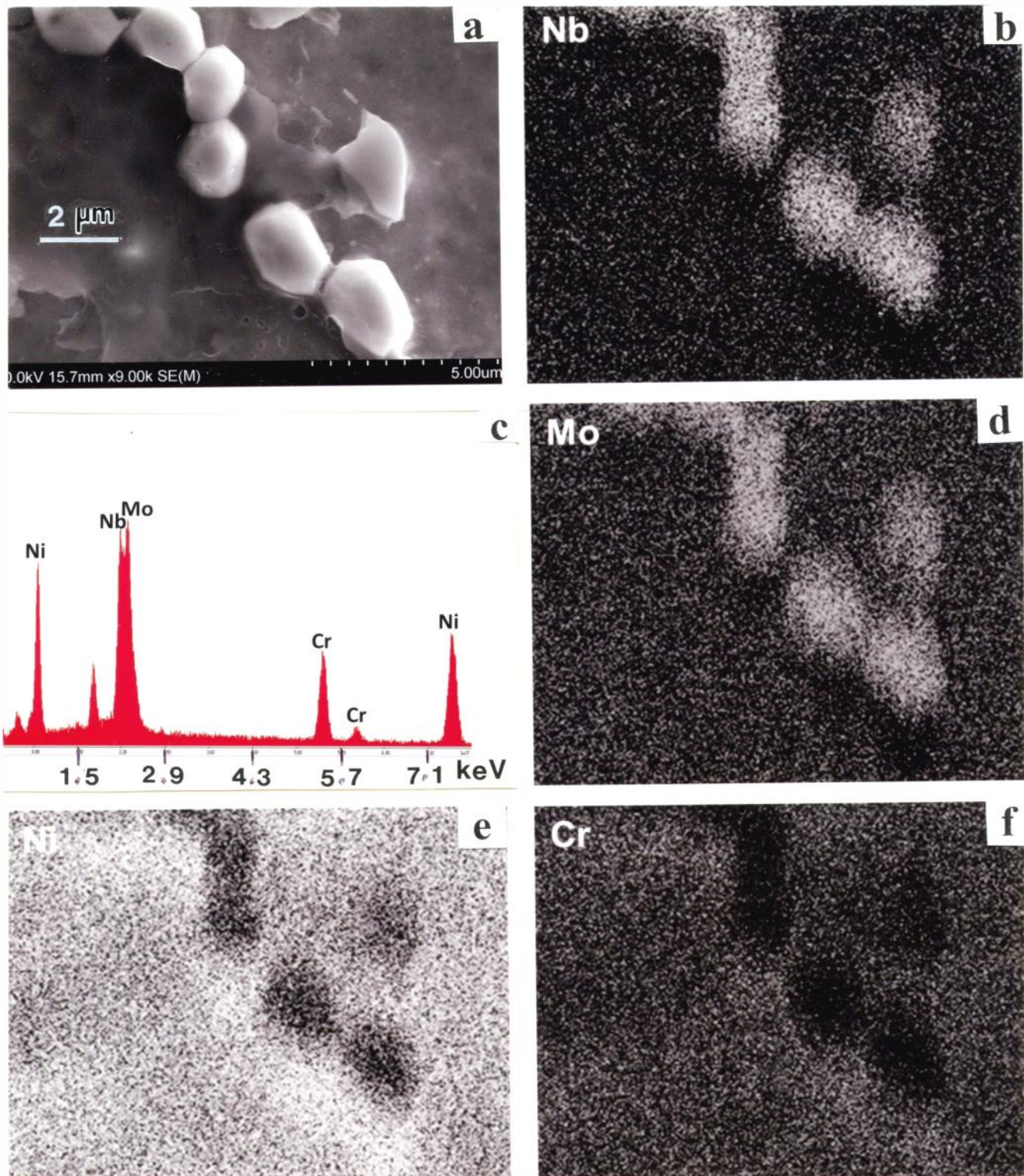


Figure 4.23. SEM analysis sequence corresponding to Fig. 4.22(a). (a) Precipitates. (b) EDS spectra for (a). (c) to (f) show corresponding EDS elemental X-ray maps.

Figures 4.24 and 4.25 show a typical, similar analysis sequence for MoNb precipitates in the XY-axis fabricated and HIP components corresponding to Figure 4.19. In contrast to Figure 4.23(c), Figure 4.25 compares the background NiCr matrix elemental (EDS) spectrum (Figure 4.25(a)) in contrast to the corresponding spectrum at the precipitates in Figure 4.24(b), where the Mo, Nb peak prominence is apparent.

Figure 4.26 shows smaller, intergranular precipitates viewed in the TEM in the horizontal reference plane for an XY-oriented, fabricated and HIP component (corresponding to Figure 4.19). Note the faceted, polyhedral which represent the nano regime for the MoNb precipitates shown in Figures 4.19 and 4.24.

Figures 4.27 to 4.29 illustrate another analytical sequence involving three precipitates indicated by P_1 , P_2 and P_3 , respectively in Figure 4.27. The inserts in Figure 4.27 show magnified views for precipitates P_2 and P_3 , respectively, while Figure 4.29 shows a more detailed analysis of precipitate P_1 . To some extent, all of these precipitates exhibit crystallographic faceting. All, like those precipitates in Figure 4.26, are noncoherent dispersoids. These precipitates represent primarily NiNb (Figure 4.21): rhombohedral (space group: $R\bar{3}m$), $a = 4.90 \text{ \AA}$, $c = 26.64 \text{ \AA}$. Clusters of precipitates shown in Figure 4.27 range from particle sizes $<10 \text{ nm}$ to $>400 \text{ nm}$. Those shown prominently as P_1 , P_2 , and P_3 in Figure 4.27 all exhibit crystallographic facets or polyhedral forms. The EDS analyses shown in Figure 4.28(a) and (b) for P_1 and P_2 , respectively exhibit variations in Ni and Nb in contrast to the background (NiCr matrix) analysis shown typically in Figure 4.25(a), and suggesting variances in Ni-Nb stoichiometry shown for the XRD data in Figure 4.21. This applies to Figure 4.29 as well where the precipitate shown in Figures 4.27 and 4.28 as P_1 can be associated either with Nb_5Ni (fcc; space group: $Rd\bar{3}m$; $a = 11.64 \text{ \AA}$), indexing the circled diffraction spot as $[\bar{2}\bar{4}6]$, or $[2\bar{1}\bar{1}]$ for NiNb in Figure 4.29(b). The corresponding dark-field (DF) image in Figure 4.29(c) using the circled reflection in Figure 4.29(b) corresponds to a cubic or hexahedral polyhedron viewed down a vertex. This is supported by comparing the bright-field image views in Figure 4.29(a) and (d), where Figure 4.29(d) is a tilted view of Figure 4.29(a).

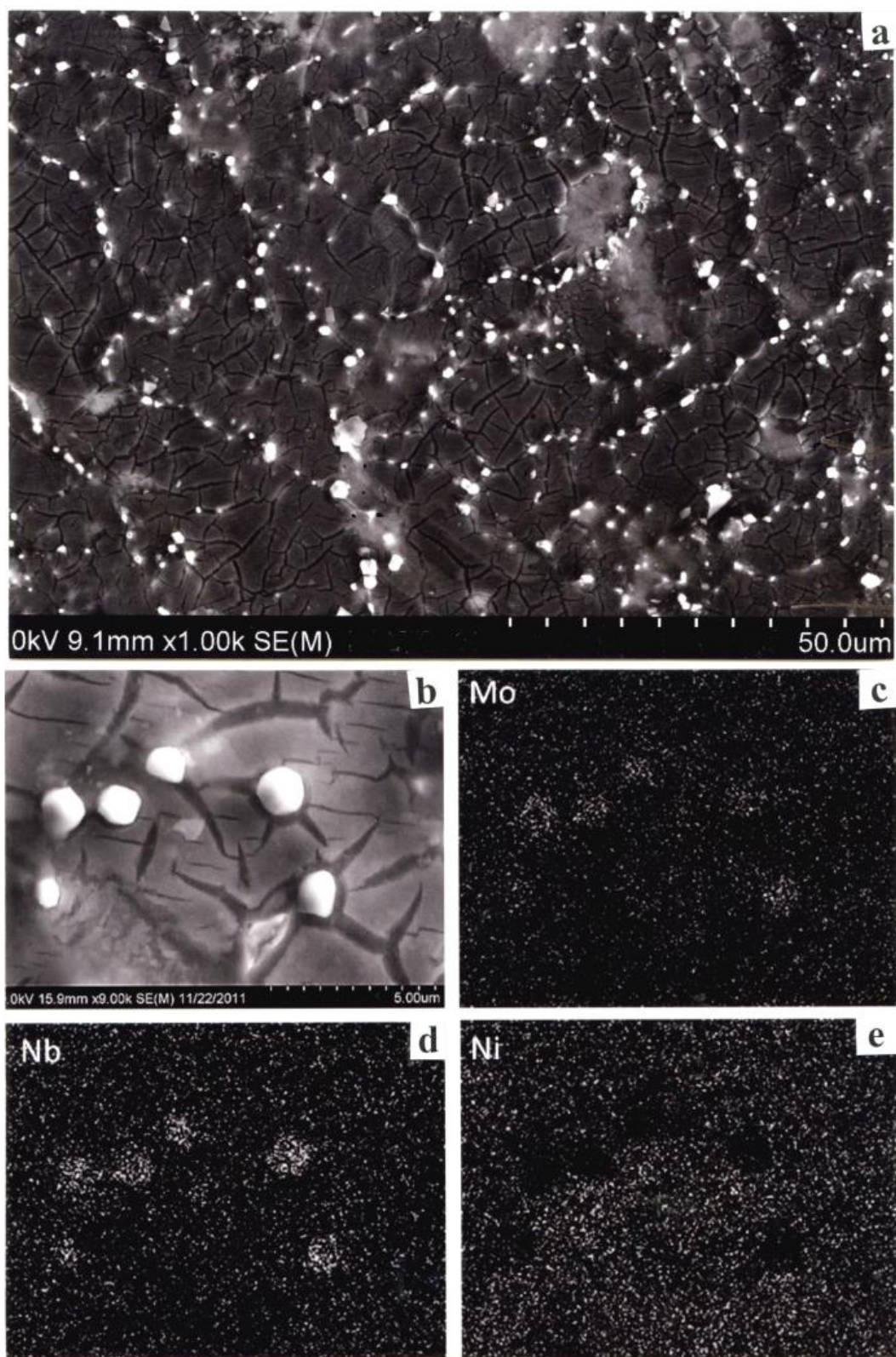


Figure 4.24. SEM analysis sequence corresponding to the vertical reference plane in Figure 4.19 (X, Y-axis) build. (a) Vertical surface view of precipitates. (b) Magnified view of precipitates. (c) to (e) show corresponding EDS elemental X-ray maps.

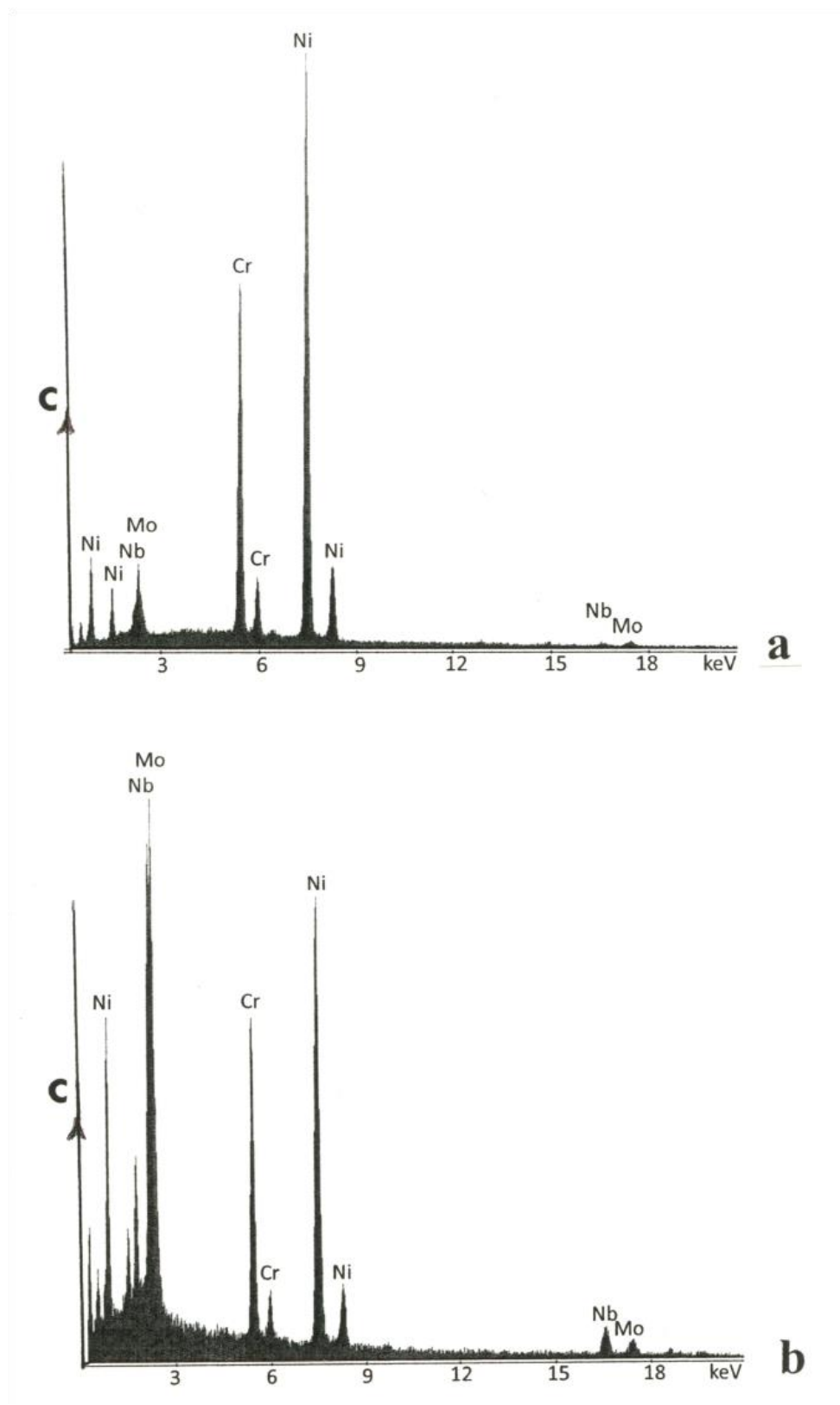


Figure 4.25. EDS spectra corresponding to Fig. 4.24. (a) matrix. (b) Precipitate area as in Fig. 4.24(b).

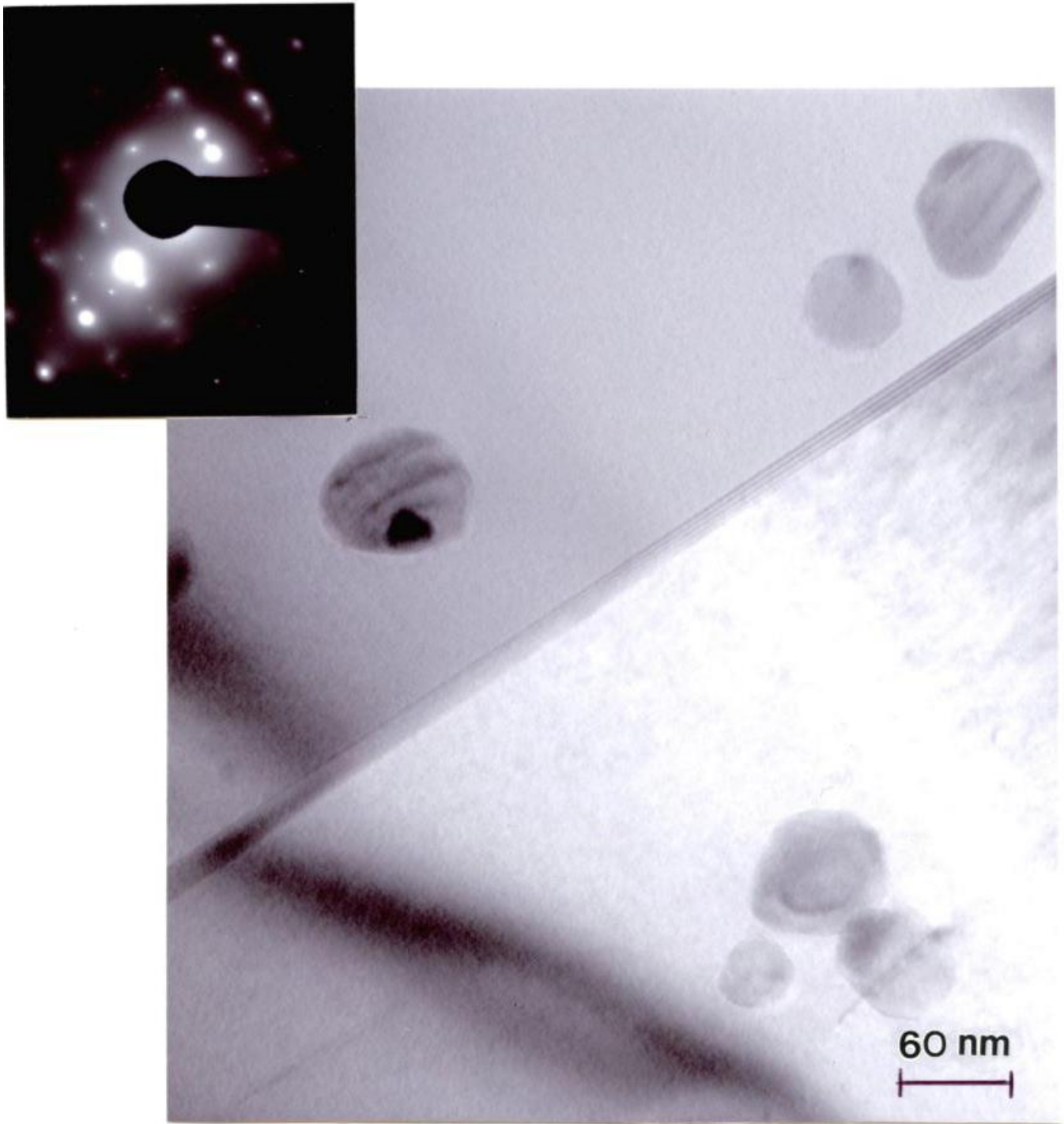


Figure 4.26. TEM image in horizontal reference plane corresponding to Fig. 4.19 (X, Y-axis component). The grain surface orientation is (110) shown in SAED pattern insert. Operating reflection, $g = [\bar{1}11]$. Note diffraction spots normal to inclined twin plane in SAED pattern insert.

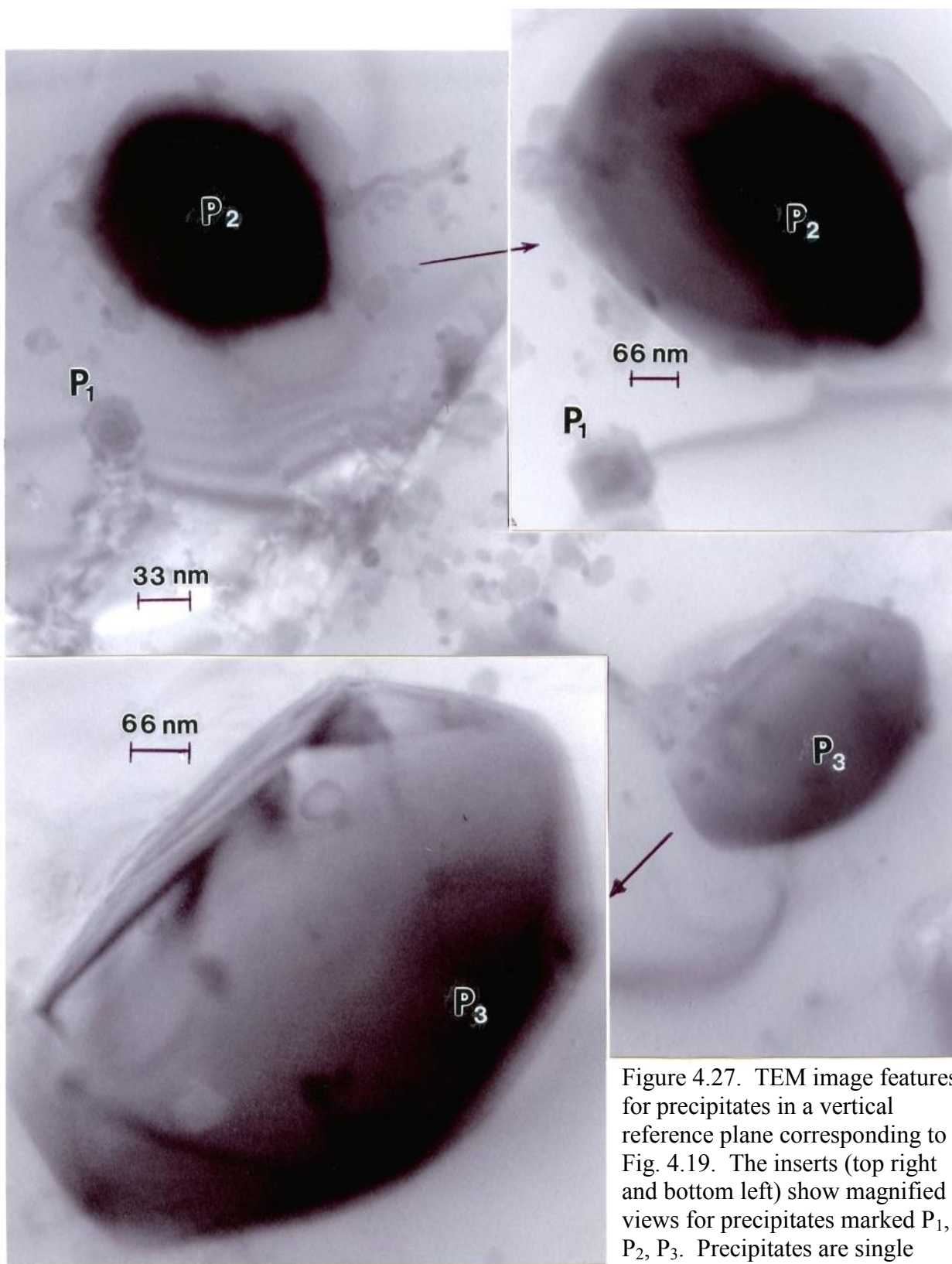


Figure 4.27. TEM image features for precipitates in a vertical reference plane corresponding to Fig. 4.19. The inserts (top right and bottom left) show magnified views for precipitates marked P_1 , P_2 , P_3 . Precipitates are single crystals dispersed noncoherently in the fcc NiCr matrix.

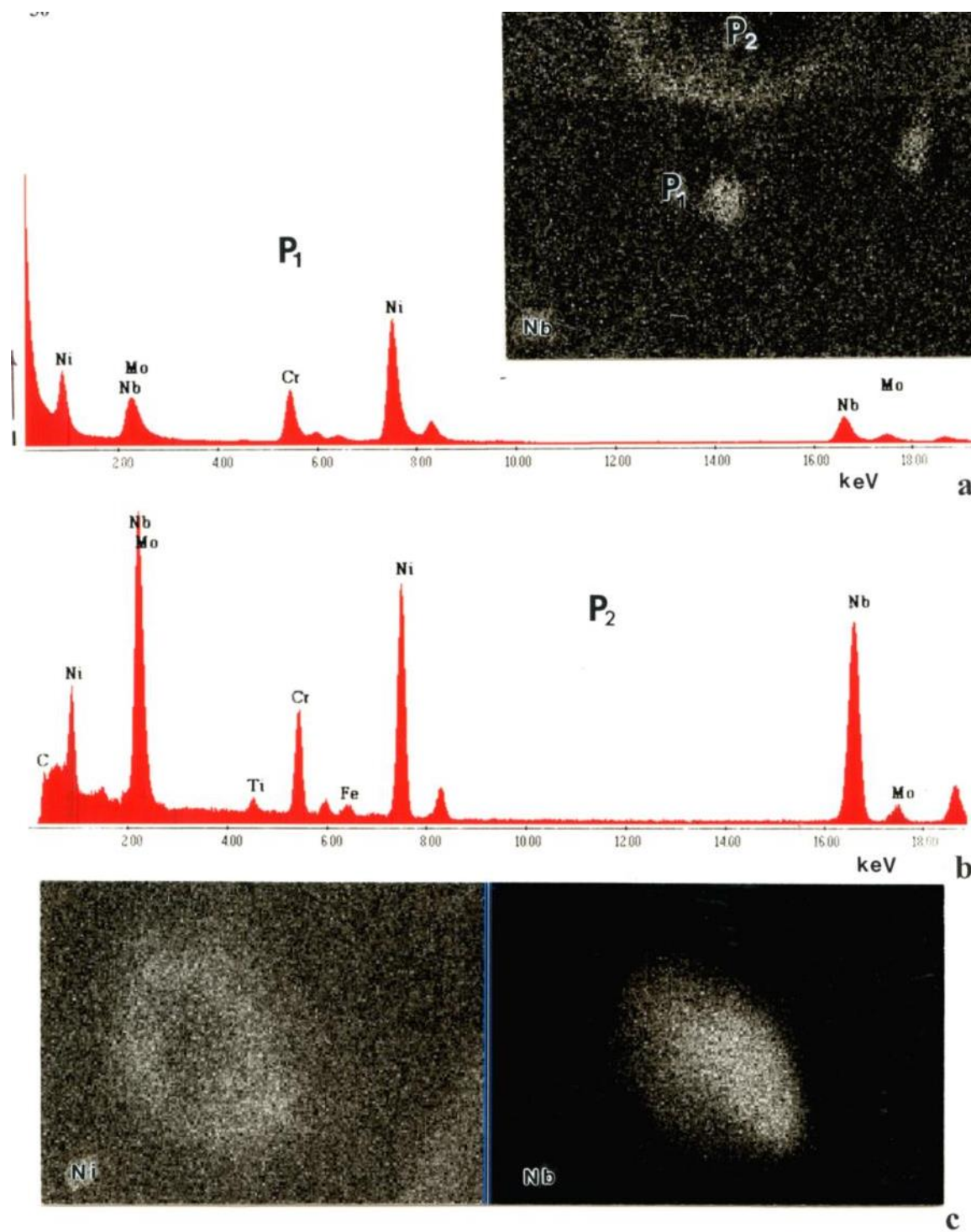


Figure 4.28. TEM microanalysis sequence for precipitates in Fig. 4.27. (a) EDS analysis for precipitate P₁. Insert shows Nb characteristic X-ray map. (b) EDS analysis for precipitate P₂. (c) Ni and Nb characteristic X-ray maps for precipitate P₂ in Fig. 4.27.

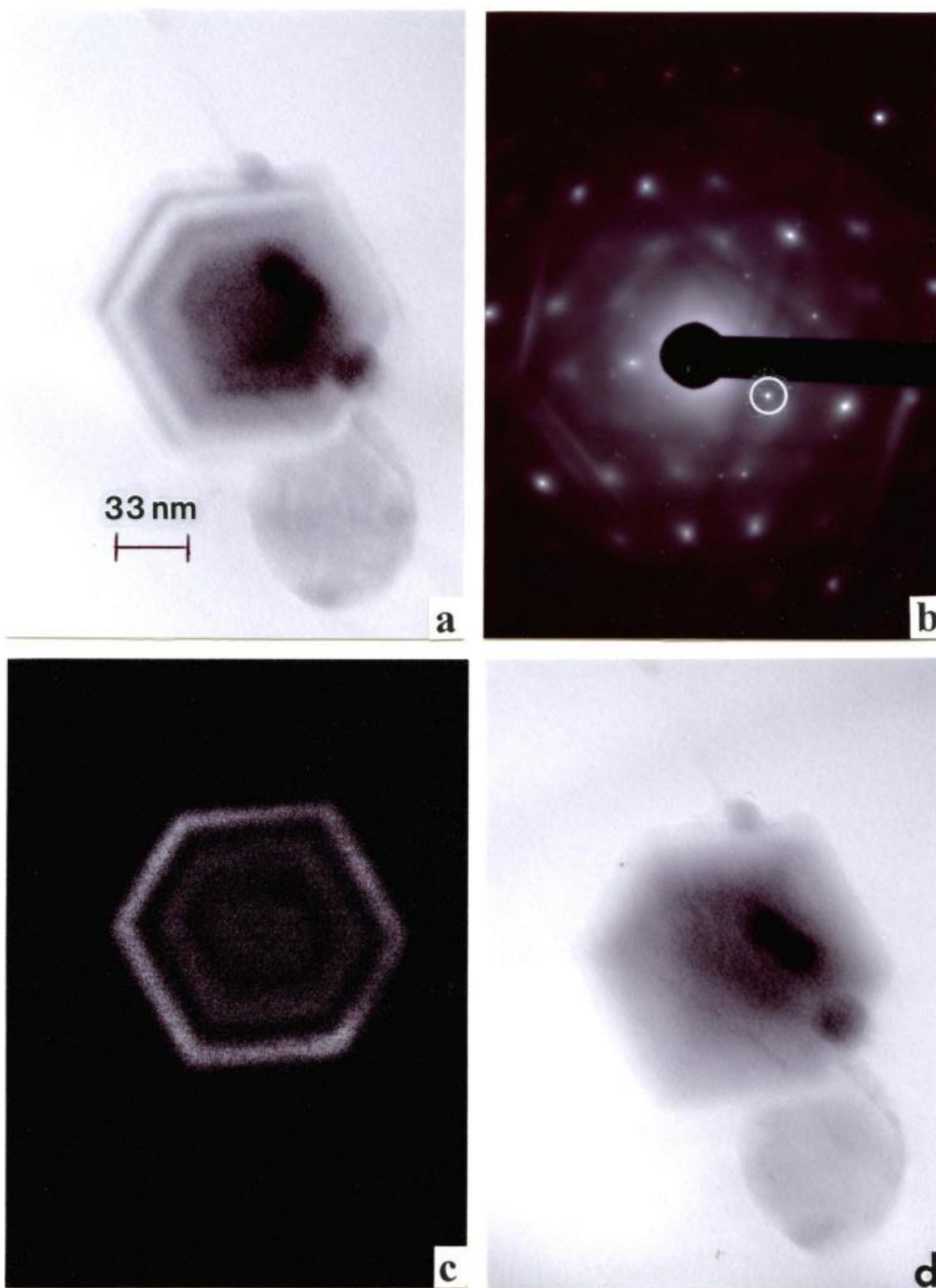


Figure 4.29. TEM microanalysis sequence for precipitate P_1 in Fig. 4.27. (a) Bright-field image. (b) SAED pattern for (a). (c) Dark-field image of (a) using $[\bar{2}\bar{4}6]$ diffraction spot circled in (b). (d) Tilted bright-field image of (a).

4.3.2 Mechanical Testing

EBM Fabricated and HIPed Components

Components built by EBM included only cylinders fabricated in the Z-axis direction (cylinder axis) and parallel to the build direction. Tensile specimens for the as-fabricated (Z-axis) specimens as well as as-fabricated and HIP specimens exhibited typical properties shown for comparison in Table 4.2. Table 4.2 also compares Vickers microindentation hardness (HV) measurements and Rockwell C-scale (HRC) macroindentation measurements for these fabricated and processed specimens. There is a corresponding hardness drop following HIP, along with a drop in yield stress (YS) but the ultimate tensile stress is not significantly affected. The drop in hardness may be due to partial recrystallization during HIPing. There is a significant increase in elongation after HIP: 69% versus 44% as-fabricated; an increase of ~57%. This considerable elongation is characterized by classical ductile-dimple fracture as illustrated typically in Fig. 4.30(b). Typical elongation of Z-axis oriented tensile specimens for as-fabricated and HIP specimens is shown in Fig. 4.30(a). Examination of the deformation associated with, and as a precursor to fracture, showed dense, generally linear dislocation arrays in {111} planes of the fcc-NiCr matrix as illustrated in Fig. 4.31. The dislocation density in Fig. 4.31 can be compared with that typical for as-fabricated EBM components shown in Fig. 4.3, where the dislocation density difference is more than an order of magnitude.

Table 4.2. Mechanical Properties for EBM and SLM Processed Alloy 625

	HV (GPa)	HRC	YS (GPa)*	UTS (GPa)†	Elongation (%)
EBM-fabricated (Z)	2.7	14	0.41	0.75	44
EBM-fabricated (Z) + HIP	2.2	8	0.33	0.77	69
SLM-fabricated (Z)	3.4	30	-	-	-
SLM-fabricated (Z) + HIP	2.9	27	0.36	0.88	58
SLM-fabricated (X,Y)	4.2	43	-	-	-
SLM-fabricated (X,Y) + HIP	3.4	21	0.38	0.90	58

* YS- 0.2% engineering offset yield stress.

† UTS- Ultimate tensile stress

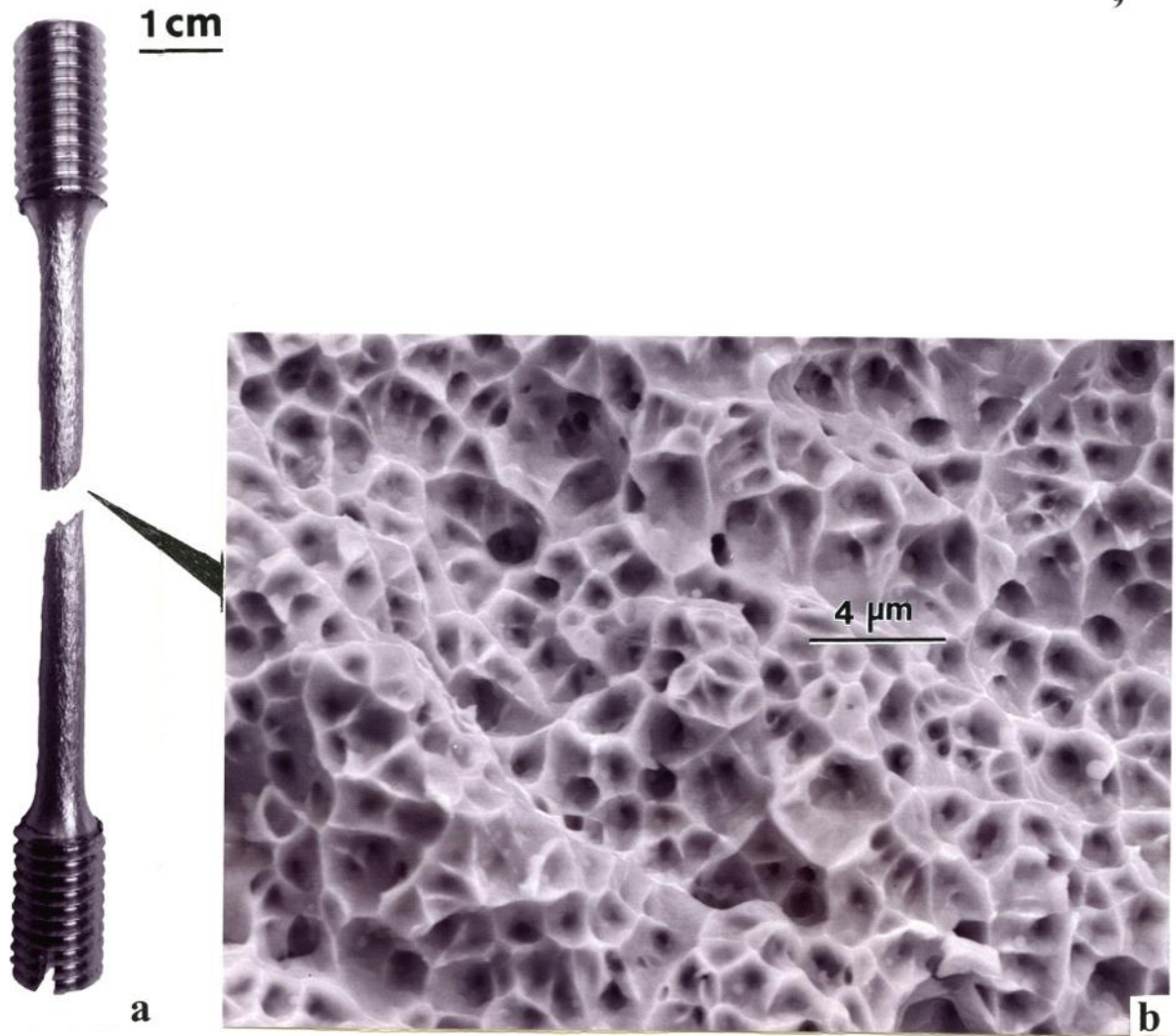


Figure 4.30. Failed tensile specimen for EBM fabricated and HIP component (a) and SEM image of corresponding fracture surface (b).

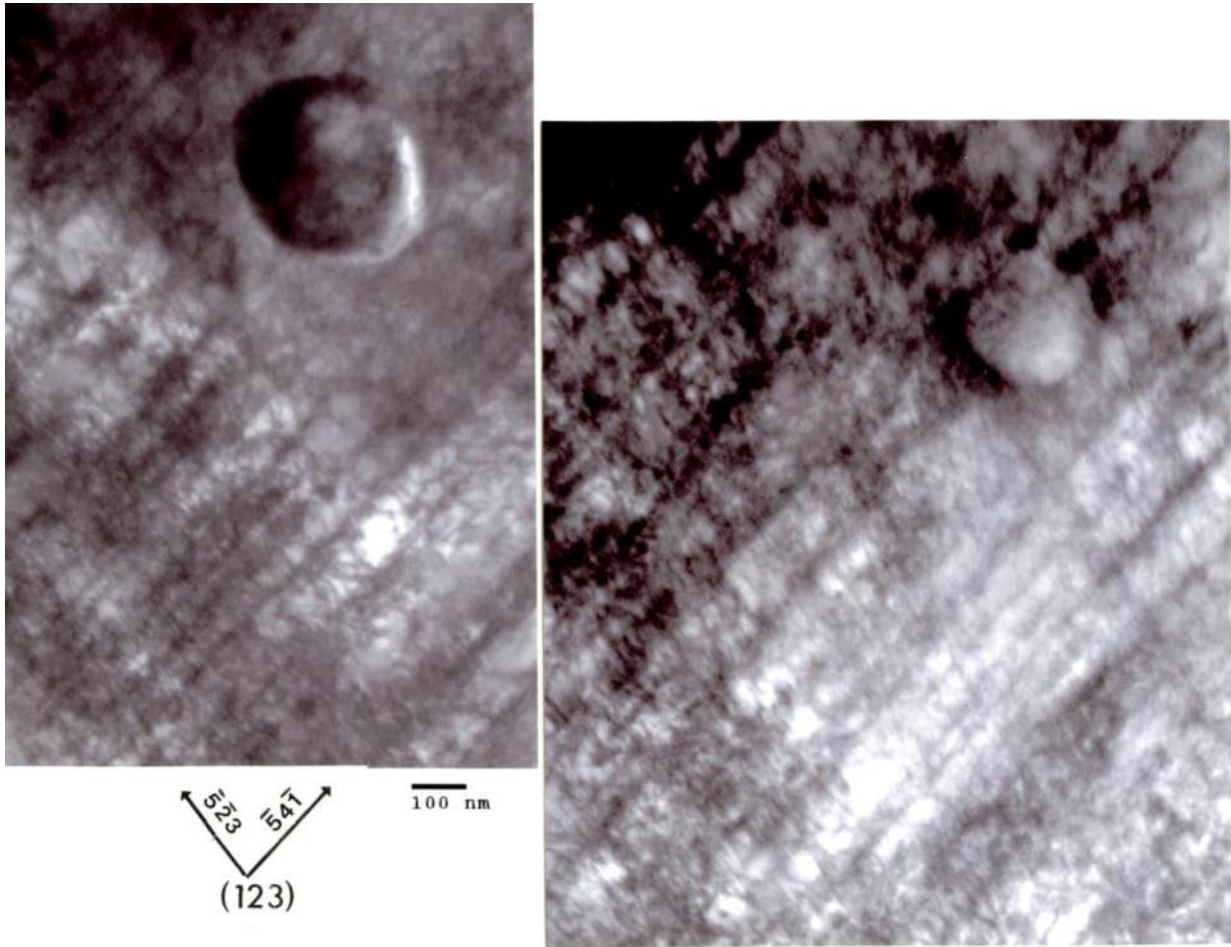


Figure 4.31. TEM image for failed tensile specimen in Fig. 4.30(a) in a section ~ 2 mm from the fracture surface, perpendicular to the tensile axis. The two views show sections in a (123) oriented matrix grain. NbCr_2 precipitates are observed.

SLM Fabricated and HIPed Components

Cylinders fabricated by SLM in the Z-axis direction as well as cylinders fabricated in the X, Y-axis directions and following HIP were machined into comparative tensile specimens and tested as described for the EBM specimens above. As-fabricated tensile tests exhibited poor tensile properties, especially elongation as a consequence of porosity and the melt pool banding as shown in Figs. 4.5 and 4.7. HIP specimens exhibited tensile behavior more comparable to the EBM components, and these measurements are shown in Table 4.2. Table 4.2 also shows the corresponding microhardness (HV) and macrohardness (HRC) measurements. It can be observed that overall the SLM fabricated and HIP components exhibited considerably higher hardness and UTS, while the elongation declined slightly.

SEM fracture surface images showed similar ductile-dimple behavior as observed in Fig. 4.30 for EBM. The elevated hardness for both the SLM-fabricated and fabricated plus HIP components (Table 4.2) are a consequence of the different precipitation microstructures evident in Figs. 4.9, 4.22 and 4.24, among others; in contrast to Figs. 4.3, 4.14, and 4.16, respectively.

4.3.2 Comparison of Precipitates in SLM and EBM Fabricated Components

A comparison of Figs. 4.2, 4.5 and 4.7 demonstrate that on a microscale, the development of columnar precipitation microstructures is considerably different for EBM fabrication versus SLM fabrication. At a smaller microstructural scale, this difference manifests in considerably different precipitate morphologies and sizes even though the precipitate chemistry is the same γ'' , bct-Ni₃Nb. Moreover, after HIP, these processed components demonstrate even more distinguishable precipitation variances, and these are shown for comparison in Table 4.3. Table 4.2 also demonstrated that the precipitation variations shown in Table 4.3 might account for variations in the residual mechanical properties, particularly for HIP processed components, by precipitation hardening.

Table 4.3. Comparative Precipitation for EBM and SLM Processed Alloy 625

EBM Fabricated	SLM Fabricated
γ'' (bct-Ni ₃ Nb) {111} coincident precipitate platelets (100 nm x 1000 nm) 2-3 μ m spaced columns (irregular)	γ'' (bct-Ni ₃ Nb) globular precipitates (10 to 20 nm diameter) <1 μ m spaced columns (irregular)
EBM Fabricated + HIP	SLM Fabricated + HIP
NbCr ₂ (laves) (most prominent) Ni ₈ Nb (trace) Cr	NbCr ₂ (laves) MoNb (most prominent) NiNb Nb ₅ Ni (trace)

The occurrence of melt-scan banding and associated γ'' precipitation within these bands illustrated in Figs. 4.5, 4.7 and 4.13 suggest considerably different thermo-kinetic phenomena which will influence precipitation, nucleation, growth, and stoichiometry as this relates to thermo-kinetic

parameters, especially time-at-temperature as this relates to stable and metastable phases. In this respect, the precipitate phases are all noncoherent, and apparently at equilibrium.

Although Thijs et al. (2010) and Bontha et al. (2009) have investigated the effect of process variables and size-scale on solidification microstructure-grain size and morphology as well as columnar grain orientations in Ti-6Al-4V processed by laser or electron beam fabrication, there are no comparable studies in other systems. In addition, there have been no systematic or systematic studies of precipitation phenomena in electron or laser-beam processed metal or alloy systems. Consequently, Table 4.3 represents the first qualitative comparison of electron and laser beam processing and related precipitation phenomena.

4.4 Summary

In both EBM and SLM processes, columnar architectures are formed parallel to the build direction by γ'' bct Ni_3Nb precipitates, yet the difference in cooling rates of the melt pools in each process significantly alters the size and shape of the precipitates as well as the columnar spacing, column width, and texture. The presence of melt banding does not exist in the EBM microstructure as it does in the SLM microstructure (Figure 4.2 and Figure 4.7, respectively). The columnar architecture of the EBM as-fabricated components is composed of large γ'' platelets aligned with a texture of [220] parallel to the build direction, with columnar arrays spaced ~ 2 to $3\ \mu\text{m}$ apart. The precipitates of the SLM as-fabricated cylinders irregular, fine Ni_3Nb precipitates with a [200] texture combined with dense dislocation arrays. The columnar precipitates of SLM-fabricated component had a spacing of roughly $1\ \mu\text{m}$ (half or less) and one third of the column width in contrast to the EBM component.

HIPing of the EBM and SLM as-fabricated cylinders at 1120°C for 4 h recrystallized the columnar grains and formed an equiaxed fcc NiCr grain structure containing low-energy annealing twins. The columnar γ'' arrays were dissolved during the annealing process and the formation of an NbCr_2 laves precipitates occurred in all fabricated and HIPed EBM cylinders. Precipitates were present in high-energy grain boundaries but absent from low-energy, coherent twin boundaries. However, intergranular MoNb precipitates (smaller in XY-oriented components) in SLM-fabricated and HIPed components were notably larger than the EBM HIPed components. These precipitates are mostly MoNb

with some NbCr₂ and traces of Nb₅Ni and NiNb, which are not present in EBM-fabricated and HIP components. The NbCr₂ laves precipitates were the most prominent in the EBM- fabricated cylinder with some pure Cu precipitates and traces of Ni₈Nb.

It should be noted on comparing the mechanical behavior for Z-axis and XY-axis fabricated components by either EBM or SLM, that there is both a size factor difference for Z-axis versus XY-axis fabrication, and a corresponding cooling-rate difference, which is more notable on comparing EBM and SLM fabrication. Table 4.2 shows that both the Vickers microindentation hardness (HV) and Rockwell C-scale hardness (HRC) increase significantly on comparing Z-axis component fabrication by EBM versus SLM. Correspondingly, there is a significant increase on comparing SLM Z-axis fabrication with XY-axis fabrication: HV 3.4 GPa versus 4.2 GPa, respectively, or an increase of 24%. In contrast to EBM Z-axis fabrication, SLM Z-axis fabrication increases even more notably: HV 2.7 GPa to 4.2 GPa, or a 56% increase; more than twice that for the SLM Z-axis versus XY-axis fabrication. There is a corresponding increase in hardness (HV) for the HIPed components: SLM - Z-axis HIP versus EBM Z-axis-HIP; and SLM Z-axis HIP versus SLM XY-axis-HIP, although the increase was not as great (Table 4.2). Nonetheless, the hardness differences shown in Table 4.2 are indicative of both the process variances (EBM versus SLM) and the component size variances (Z-axis oriented components versus XY-axis components).

Chapter 5: Discussion

5.1 Fabrication parameters

The flexibility to change the parameters of the fabrication process allows us to manipulate the microstructure, and, therefore, the mechanical properties of the material being manufactured. In this study, multiple parameters were adjusted and compared including fabrication process, build environment, and build orientation. The parameter differences in the two fabrication processes (EBM and SLM) included scan speed and cooling rate.

It can be seen in Figures 3.5, 4.2, and 4.5 that the as-fabricated cylinders all have a directionally solidified microstructure with a similarity between the grain texture and columnar architecture of the precipitation. The difference between the microstructures in EBM and SLM is mainly the melt pool formation in the SLM fabricated specimens, as shown in Figures 3.5 and 4.5, which is not present in the EBM fabricated specimens. As previously mentioned in Chapter 4, this is due to the difference in the cooling rate, which can be explained by the variance in scan speed by one order of magnitude (10^2 versus 10^3 mm/s for EBM and SLM, respectively). In the SLM process, each layer has ~1000 mm/s less time than specimens fabricated by EBM to cool before another layer is added.

Another parameter that was manipulated was the build environment. Since EBM uses a vacuum environment, that could not be altered. However, for the SLM process, argon and nitrogen environments were compared, but there was no significant difference in the microstructures of the cylinders.

Inconel 718 and Inconel 625 cylinders were built in orientations parallel and perpendicular to the build direction. The columnar architectures and grain texture are similar when comparing the Z-axis oriented and X-Y axis oriented cylinders for both alloys, as can be seen in Figures 3.8, 3.9, 4.5 and 4.7.

5.2 X-Ray Diffraction

X-Ray diffraction was used to identify study the morphology of the precipitates formed during fabrication as well as the texture of the grains before and after heat-treating the cylinders. As expected, γ'' Ni₃Nb precipitates and a γ' NiCr matrix were present in all as-fabricated specimens for both alloys. The orientation, environment, and cooling rate did not play a role in the presence of these phases.

However, the texture of the grains for EBM specimens and SLM Z-axis and X-Y oriented specimens differed for Inconel 625, as seen in Figures 4.3, 4.6, and 4.8.

Although the mixed texture of alloy 718 specimens varied, the phases stayed the same after HIPing the cylinders. The only change in precipitation occurred after annealing the specimens, which was the presence of δ phase in addition to γ'' . For alloy 625 specimens, however, there was a significant difference in the XRD spectra for EBM and SLM components and parallel and perpendicular build directions. Table 4.3 summarizes the different precipitates that formed before and after HIPing for both fabrication processes.

5.3 Scanning and Transmission Electron Microscopy

Electron microscopy and EDS analysis confirmed the findings of the XRD analysis. In Figures 3.14 and 4.3, lenticular-shaped γ'' precipitates are stacked in columns, as seen in LOM images. The change in precipitation from the annealing process can be seen in Figure 3.20, where the shape, phase, and location of precipitation is different from the as-fabricated specimens.

There was a significant difference in the size and morphology of precipitation after specimens were HIPed for alloy 625. EBM-fabricated components begin with fine, dense dislocation arrays of γ'' clusters (Figure 4.9). After being HIPed, larger, globular, intergranular precipitates nucleated (Figures 4.16 and 4.17). The SLM components also grew in size while crystallographic faceting occurred in most precipitates. In the SEM and TEM images, it is evident that the fabrication processes play a big role in the type of precipitation that forms after heat treating.

5.4 Mechanical Behavior

When comparing the mechanical properties of Inconel 718 fabricated by SLM to cast and wrought 718, it is evident in Table 3.1 that the Rockwell hardness is substantially higher for the annealed specimen fabricated by SLM compared the wrought alloy. Also, the hardness is higher for the Z-axis than the X-Y oriented cylinder. However, in Table 4.2, the hardness is higher for the X-Y cylinder than the Z-axis cylinder as well as the EBM-fabricated specimen. The SLM specimens have a higher hardness due to the faster cooling rate, which affects precipitation nucleation and growth. The

SLM components have fine intergranular precipitates and less spacing between columns than EBM components.

Although the elongation does not vary in the cylinders with different orientations, the yield strength and ultimate tensile strength is slightly higher for X-Y specimens. This is due to the orientation of columnar grains and precipitate columns and the direction that the stress is being applied on these grains.

Chapter 6: Conclusion

With innovations of new technologies such as additive manufacturing, we are able to manipulate the properties of a particular superalloy by controlling the parameters of the fabrication process as well as choosing a specific fabrication process. The Inconel alloy system is used in many applications due to its ability to withstand a wide range of temperatures and detrimental conditions. Inconel 718 and 625 are particularly strong alloys at high temperatures due to their ability to form precipitates as they are exposed to elevated temperatures. For this reason, they are heat treated before being put into the market to increase their value. One advantage to manufacturing parts using EBM and SLM is that the fabrication processes involve melting, which allows these precipitates and other desirable features, such as directional solidification, to be achieved during fabrication rather than after. This eliminates many steps in the entire fabrication process, which normal involves casting, heat treating, and machining. With additive manufacturing, we are able to produce parts that are closer to the finished product while eliminating production time and costs.

This study has demonstrated only a few ways that objects produced can be customized to fit a particular application. In previous studies, various shapes, densities, and constructions have been produced and analyzed to show that metal meshes and foams can be manufactured with lower densities than solid parts with equally, if not better, mechanical properties (Gaytan, et al. 2010). While EBM and SLM have been used to fabricate complex superalloy components (Thijs, et al. 2010, Gaytan, et al. 2010), the mechanical properties of this alloy system have not been previously compared to its cast and wrought counterparts.

Now that there is a better understanding of this alloy system using EBM and SLM, it is possible to extend this study by fabricating complex shapes and varying densities of this alloys system. One example of the benefits of this study includes the ability to build aircraft components with a hollow or less dense center, making the parts lighter while increasing the lifetime of these components due to their increased performance. There is a myriad of possibilities with the amount of ways that these new methods allow components to be customized, whether it be mechanical properties, shape, finish, or material.

References

- Amato, K.N., Gaytan, S.M., Murr, L.E., Martinez, E., Shindo, P.W., Hernandez, J., Collins, S., and Medina, F. *Acta Mater* 2011; 60(1): 2229-39.
- Amato, K.N., Murr, L.E., Hernandez, J., Martinez, E., Gaytan, S.M., Shindo, P.W., and Collins, S. *J Mater Sci Res* 2012; 1(2).
- Azadian S., Liu-Ying, W., Warren R. *Mater Character* 2004; 53:7-16.
- Bontha, S., Klingbeil, N. W., Kobryn, P. A., & Fraser, H. C. *Mater Sci Engr A* 2009; (513-514): 311-318.
- Cormier, D., Harrysson, O. L., & West, H. (2004). *Rapid Prototyping J.*, 10(1): 35-41.
- Cozar R., Pineau A. *Metall Trans* 1973; 4:47-59.
- Eiselstein H.L. *ASTM-STP369*. 1965:62-70.
- Faubert F.M., Springer G.S. *J Chem Phys* 1972; 57:2333-2340.
- Gaytan, S. M., Murr, L. E., Martinez, E., J. L., Machado, B. I., Ramirez, D. A., Medina, F., Collins, S., & Wicker, R. B. *Metall Mater Trans* 2010; 41A: 3310-3327.
- Ganesh, P., Kaul, R., Paul, C.P., Tiwari, P., Rai, S.K., Prasad, R.C. Kukreja, L.M. *Materials Science and Engineering A* 2010; 527: 7490-97.
- He J, Fukuyama S, Yokogawa K. *J Mater Sci Technol* 1994; 10:293-303.
- Kirman I., Warrington O.H., *J Inst Metals* 1971; 99:197-202.
- Li, R.B., Yao, M., Liu, W.C., He, X.C. *Scripta Mater* 2002; 46:635-638.
- Mankins, W.L., Lamb, S. 1990. "Nickel and Nickel Alloys." *ASM Handbook*. 2. California.
- Mehrabian R, Kear BH, Cohen M. (Eds.) *Rapid Solidification Processing*. 1975. Baton Rouge: Claitor's Publishing Div.
- Murr, L. E. *Interfacial Phenomena in Metals and Alloys*. 1975. Reading: Addison-Wesley Publishing, Co.
- Murr, L. E., Quinones, S. A., Gaytan, S. M., Lopez, M. I., Rodela, A., Martinez, E. Y., Hernandez, D. H., Martinez, E., Medina, F., & Wicker, R. B. *J. Mech. Behavior Biomed. Mater.* 2009, 2: 20-32.
- Murr L.E., Martinez E., Gaytan S.M., Ramirez D.A., Machado B.I., Shindo P.W., Martinez J.L., Medina F., Wooten J, Ciscel D, Ackelid U, Wicker RB. *Metall Mater Trans A* 2011; A: 3491-3508.
- Murr, L. E., Gaytan, S. M., Ramirez, D. A., Martinez, E., Hernandez, J., Amato, K. N., Shindo, P. W., Medina, F., & Wicker, R. B. *J Mater Sci Technol* 2012a; 28(1):1-14.
- Murr, L. E., Martinez, E., Hernandez, J., Collins, S., Amato, K. N., Gaytan, S. M., & Shindo, P. W. *Mater. Sci. Engr A* 2012b; 1(3).
- Oblak J.M., Paulonis D.F., Duvall D.S.. *Metall Trans* 1974; 5:143-151.
- Patterson II R.J., Cox A.R., VanReuth E.C. *J Metals* 1980; 32(9):34-39.
- Paulonis D.F., Oblak J.M., Duvall D.S. *Trans ASM* 1969; 62:611-616.
- Shankar, V., Sankara Rao, K.B., Mannan, S.L. *Journal of Nuclear Materials* 2001; 288 (2–3): 222-232.
- Smith, W.F. *Structure and Properties of Engineering Alloys*. 1981. Flint: McGraw-Hill.
- Strondl, A., Fischer, R., Frommeyer, G., & Schneider, A. *Mater Sci Eng A* 2008; 480A: 138-147.
- Sundararaman M., Mukhopadhyay P., Banerjee S. *Metall Trans* 1992; 23A:2015-2028.
- Strondl A, Fischer R, Frommeyer G, Schneider A. *Mater Sci Engr A* 2008; 480A:138-147.
- Slama C., Serrant C., Cizeron G. *J Mater Res* 1997; 12(9):2298-2316.
- Thijs L., Verhaeghe F., Craeghs T., VanHumbeeck J., Kruth J-P. *Acta Mater* 2010; 58:3303-3312.

Appendix

From: Journal of Materials Science Research [jmsr@ccsenet.org]
Sent: Tuesday, October 30, 2012 6:51 PM
To: Amato, Krista N
Subject: Re: Request to use published journal article in a dissertation

Dear Krista Amato,

Thanks for your query.

It is permission to use the material published in Journal of Materials Science and Research.
Accurate reference is suggested.

Copyrights for articles published in CCSE journals are retained by the authors, with first publication rights granted to the journal. The journal/publisher is not responsible for subsequent uses of the work. It is the author's responsibility to bring an infringement action if so desired by the author.

Please feel free to cotact with me if you get any question.

Best regards,

Lily Green
Editorial Assistant
Journal of Materials Science Research
2012-10-31

1120 Finch Avenue West, Suite 701-309, Toronto, ON., M3J 3H7, Canada
Tel: 1-416-642-2606 ext.241
Fax: 1-416-208-2608
E-mail: jmsr@ccsenet.org
Website: www.ccsenet.org/jmsr

===== At 2012-10-31, 05:26:22 you wrote: =====

>Krista N. Amato
>
>The University of Texas at El Paso
>500 W. University Ave.
>College of Engineering Building, M-201
>El Paso, TX 79968, USA
>Email: knamato@miners.utep.edu<<mailto:knamato@miners.utep.edu>>

>
>
>

>Journal of Materials Science Research
>1120 Finch Avenue West, Suite 701-309, Toronto, ON., M3J 3H7, Canada
>E-mail: jmsr@ccsenet.org

>
>

>Dear Dr. Lily Green,

>
>
>

>I am a Ph.D candidate at The University of Texas at El Paso, El Paso, TX 79968, USA. I have published an article in your journal cited as follows:

>
>

> Amato, K.N., Murr, L.E., Hernandez, J., Martinez, E., Gaytan, S.M., Shindo, P.W., and Collins, S.

> Comparison of Microstructures and Properties for a Ni-Base Superalloy (alloy 625) Fabricated by

> Electron and Laser Beam Melting. Journal of Materials Science Research (2012), Vol. 1, No. 2.

>

>I am writing to request permission to include the material in the article cited above in my dissertation. The University of Texas at El Paso will accept permission to use the material published in Journal of Materials Science and Research in the form of a response to this email. Thank you.

>

>Best Regards,

>
>
>

>Krista Amato

>
>
>

=====

Journal of Materials Science Research
jmsr@ccsenet.org
2012-10-31

Vita

Krista Amato earned her Bachelor of Science degree in Metallurgical and Materials Engineering from The University of Texas at El Paso in May 2010. She joined the Fast Track doctoral program in Fall 2010. She has been the recipient of numerous honors and awards including a Woman's Auxiliary Fellowship and a Metallurgical and Materials Engineering Graduate Research Award. While pursuing her degree, Krista worked as a research assistant and a teaching assistant for the department of Metallurgical and Materials Engineering. She has presented her research at international conference meetings including TMS 2012 Annual Meeting & Exhibition and the Materials Science & Technology 2011 Conference and Exhibition. Krista is the author of two publications including, "Microstructures and mechanical behavior for Inconel 718" and "Comparison of Microstructures and Properties for a Ni-Base Superalloy (Alloy 625) Fabricated by Electron and Laser Beam Melting." She is also the co-author of several publications. Her dissertation was supervised by Dr. Larry Murr.

Permanent address: 1112 Canyon Run Dr.
El Paso, TX 79912

This dissertation was typed by Krista Amato.